Linking the Solar Magnetism from the Interior to the Outer Atmosphere

by

Fang Fang

A dissertation submitted in partial fulfillment
of the requirements for the degree of
Doctor of Philosophy
(Atmospheric and Space Sciences)
in The University of Michigan
2012

Doctoral Committee:

Professor Tamas I. Gombosi, Co-Chair
Research Associate Professor Ward B. Manchester, IV, Co-Chair
Professor Lee W. Hartmann
Associate Research Scientist Bart van der Holst
Research Physicist William P. Abbett, University of California

TABLE OF CONTENTS

LIST OF FIGURES

Figure

ABSTRACT

Linking the Solar Magnetism from the Interior to the Outer Atmosphere

by

Fang Fang

Co-Chairs: Ward B. Manchester, IV & Tamas I. Gombosi

Solar magnetic fields, produced in the interor and extending all the way into the interplanetary space, connect the Sun with the terrestrial environment. They manifest themselves on the solar surface over a wide range of scales, from ubiquitous ephemeral regions as small as 10^{16} Maxwells, to active regions as large as 10^{23} Maxwells. The appearance of kilo-Gauss magnetic flux bundles on the photosphere is observationally well studied. However the physical processes that produce observed magnetic structures are yet to be well-understood, due to the lack of information below the solar surface. To illustrate the physics of sub-surface magnetic fields, we carry out numerical simulations of the emergence of magnetic flux ropes from the convection zone through the photosphere and into the corona. The spatial scale of our simulations varies from ephemeral regions to active regions. This study of the formation of magnetic structures shows the importance of the interaction of rising magnetic fields and turbulent convective motions:

The first simulation addresses the emergence of a flux rope with a total axial flux of 3×10^{19} Mx. From a shallow convection zone, it self-consistently forms an

ephemeral region at the photosphere and disrupts the near-surface convection pattern, with magnetic flux quickly becoming concentrated in the downflow regions.

In another simulation, a flux rope with a total axial flux of 1×10^{21} Mx, buoyantly rises from 10 Mm below the photosphere, interacts with convective cells of varying scales and forms a small active region with a pair of sunspots by the coalescence of small-scale flux and the subsequent intensification from convective collapse.

At the beginning of the emergence, vertical motion dominates the energy transport into the corona when the flux first passes through the photosphere. After that, horizontal motions, i.e., shearing, separating motion of magnetic dipoles, and rotation of magnetic polarities take over the energy transport, while vertical motion transports energy back into the convection zone due to the concentration of magnetic flux in downflow regions.

In our simulations, we find strong shearing motions draw the magnetic field parallel to the polarity inversion line. Tether-cutting reconnection then transfers the magnetic shear into the corona. Together, with the rotation of sunspots, these processes produce and transport free magnetic energy into the corona during times of the flux emergence and cancellation. The free energy in the corona increases to 8×10^{30} erg within 3 hours, which may provide the energy necessary for solar eruptive events, such as coronal mass ejections, flares, and filament eruptions.

A comparison of our simulation with observations of active region 11158 finds the same physical processes at work over longer time scales and larger spatial scales. Strong shear flows, enhanced horizontal field strength, and converging flows at the polarity inversion line are found to precede a fast coronal mass ejection accompanied by an X-class flare. The close match between the simulation and observations support the conclusion that shearing motion builds up the necessary magnetic energy to drive eruptive events.

CHAPTER I

Introduction

Among all the stars in the Universe, the Sun is the most well observed and understood. The most basic facts about the Sun can be summarized as follows: the Sun is a 5×10^9-year old, G2V main-sequence star in the Hertzsprung-Russell diagram. The Sun has a mass of 2×10^{30} kg, a radius of 7×10^8 m, and lies at the center of our solar system, 1.5×10^{11} m from our Earth. It provides the energy source for all life on earth in the form of electromagnetic radiation, at a luminosity of 3.8×10^{26} W. This energy is produced in the Sun's core by thermonuclear reactions, and then transported through the solar interior by radiative and convective processes until it escapes at the visible surface, and radiates into interplanetary space.

These simple facts belie the enormous complexity of the Sun, which is not well understood. While it is the closest star to our planet, our knowledge about the Sun's complex magnetic structure and dynamic activity is incomplete. For example, a well-known discrepancy in the measured and predicted solar neutrinos, produced in the solar interior, was not solved until recently when observations distinguished the flavors of neutrinos. In the solar atmosphere, it is still controversial what mechanism heats the coronal plasma up to temperatures of 10^6 K. The magnetic field of the corona extends far from the Sun into interplanetary space and connects the Sun with Earth through a continous stream of charged particles constrained to the field

known as the *solar wind*. Yet how the solar wind is energized is still a matter of debate. The 11-year sunspot cycle gave rise to the development of dynamo models, but these models have yet to reproduce the observed features of previous cycyles, or reliably predict the characteristics of future cycle of acitivity. The destabilization of the magnetic structures on the Sun results in a variety of eruptive behaviors, such as *coronal mass ejections* (CMEs), *flares* and *filament eruptions*. Each releases enormous amounts of plasma and energy into the interplanetary space. But the question of how solar eruptions are energized and initiated remains. The eruptions at the Sun drive disturbances in the terrestrial environment, called *geomagnetic storms*. These storms affect both space and ground-based assets. They damage spacecraft by radiation and charging, disrupt radio signals necessary for GPS and communication, and induce currents on power grids. These storms occur during times of enhanced magnetic activity on the Sun when it is more likely that geo-effective eruptions can occur. Thus, it is crucial to understand the magnetic behavior of the Sun in order to better predict the response of the Sun-Earth environment.

The importance of the Sun not only lies in its impact on the terrestrial environment, but also in its unique ability to provide a laboratory for the study of physical processes that cannot be reproduced in a terrestrial environment. The Sun has a uniformly rotating inner core and radiative zone, covered by a convective envelope, that rotates differentially. The extremely high temperature ($\sim$10 MK) at the core of the Sun ionizes atoms forming free electrons, whose motion produces currents and magnetic fields in the solar convection zone. These magnetic fields are frozen-in to the turbulent plasma due to the high electrical conductivity. The magnetic fields are amplified by dynamo processes, pervade the solar interior and atmosphere, and extend out into interplanetary space. It is the magnetic field that connects the hot, dense solar interior with the solar atmosphere and terrestial environment. The interaction between the convective turbulence and the magnetic field gives rise to the extreme

complexity of magnetic structures observed at the photosphere. These structures are observed to vary drastically over a wide range of spatial and temporal scales. At the high end of the spectrum are sunspots and active regions. Large concentrations of magnetic flux in and around active regions and sunspots are often the source regions of geo-effective magnetic eruptions, suh as CMEs and flares. Our work here, is devoted to understanding the link between active-region magnetism in the solar interior and atmosphere, and the associated energy transfer through these layers. The remainder of this thesis is organized as follows: Chapter I describes the basic structure of the Sun, and the previous work that our study builds on. Chapter II describes the formation of an ephemeral region by magnetic flux emergence from the near-surface convection zone to the solar corona. Chapter III examines the emergence of a small solar active region by the interaction of emerging magnetic fields and the plasma motion in the upper 20 Mm of convection zone. Chapter IV discusses the buildup of the free magnetic energy necessary for solar eruptive events during the flux emergence and Chapter V compares the simulation results with observations. Finally, Chapter VI summarizes our conclusions.

1.1 The Structure of the Sun

The Sun's plasma does not have a sharp boundary such as a white dwarf or neutron star does. However, the Sun's gravity causes the density and temperature of its plasma to vary dramatically from the core to the outer layer, which determines what physical processes dominate at different radii. Based on observational evidence and theoretical analysis, our current understanding of the Sun suggests a structure as shown in Figure 1.1. The interior consists of three zones, with increasing radius: the core, the radiative zone and the convection zone. The temperature and density drop monotonically from the core to the surface, shown in Figure 1.2. The dense, hot plasma produces a solar interior completely opaque to radiant energy, while in the

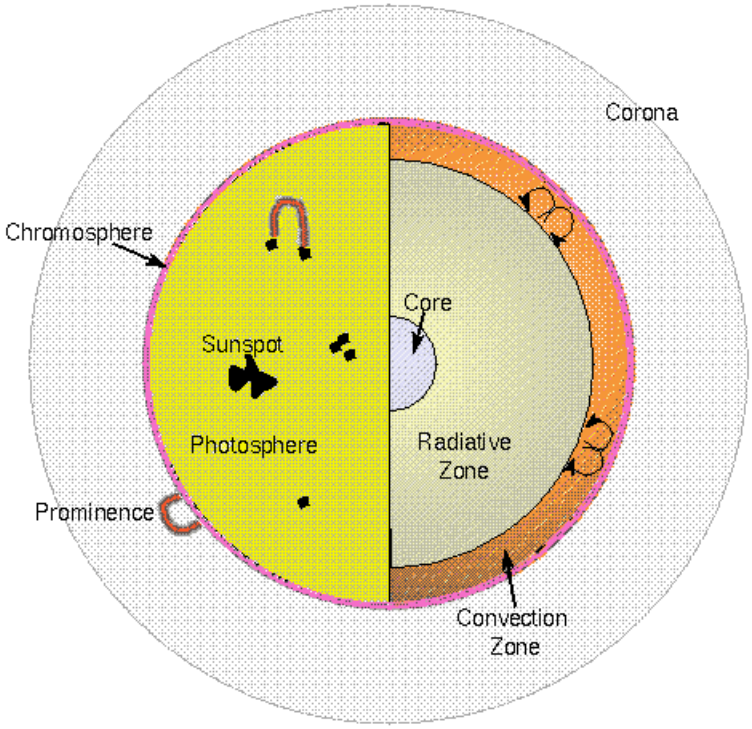

Figure 1.1: A cut-view structure of the Sun showing the interior and the atmosphere. Figure from http://www.astronomynotes.com.

relatively cool solar atmosphere, the density drops by many orders of magnitude, and the plasma becomes nearly transparent to radiation. The transition from opaqueness to transparency of the plasma defines the visible surface of the Sun. Above the surface, the atmosphere becomes complex. The chromosphere is a region that is transparent to continuum radiation but optically thick (opaque) to energetically important spectral lines. Coronal plasma is optically thin, but non-thermal processes can be important, particularly as the magnetic field releases energy in eruptive events. The stratification of the temperature and density in the atmosphere of the Sun is shown in Figure 1.3. In the following sections, we discuss the detailed properties and physics of the layers of our particular interest.

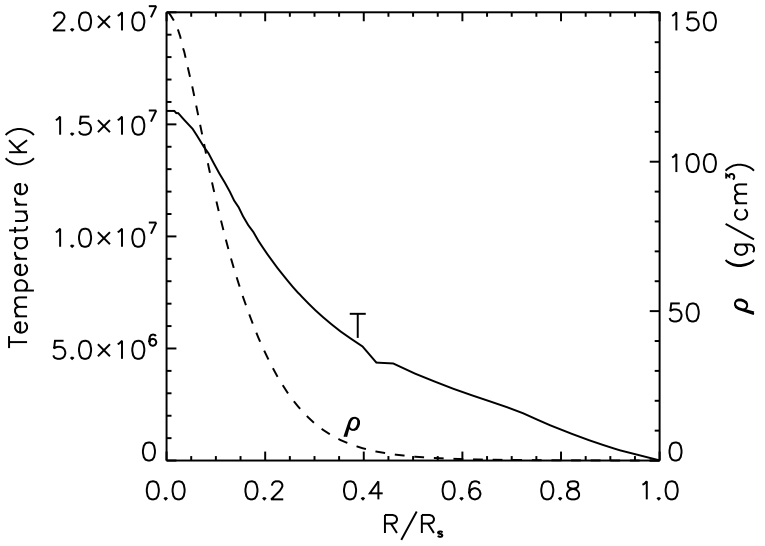

Figure 1.2: The stratification of the density and temperature in the solar interior. Data from Bahcall & Ulrich (1988).

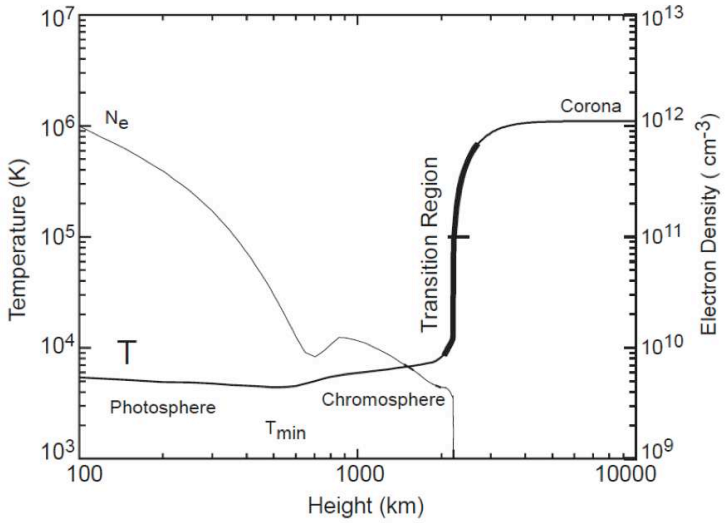

Figure 1.3: The stratification of the density and temperature in the solar atmosphere. Figure from Gary et al. (2007).

1.1.1 The Solar Core and Radiative Zone

The production of 99% of solar energy takes place in the core, which extends from the center of the Sun to 25% R_s. Composed of hot, dense plasma (see Figure 1.2), the core provides the physical conditions necessary for nuclear fusion of protons into helium. The 1.5×10^7 K temperature completely ionizes the plasma, allowing isolated

proton nuclei with an average energy of 2 keV to overcome electromagnetic repulsion and undergo thermonuclear fusion. The nuclear fusion inside the solar core can be described as follows (Gombosi, 1998):

$$p + p \rightarrow {}^2H + e^+ + \nu_e \tag{1.1}$$

$${}^2H + p \rightarrow {}^3He + \gamma \tag{1.2}$$

$${}^3He + {}^3He \rightarrow {}^4He + 2p \tag{1.3}$$

The net result of these reactions is that

$$4p \rightarrow {}^4He + 2e^+ + 2\nu_e + 2\gamma. \tag{1.4}$$

In this process the conversion of four protons to a helium nucleus consumes 0.029 amu, and releases 26.73 MeV, carried by gamma rays and neutrionos shown in the equation above. In the core, the reaction takes place $\sim 9{\times}10^{37}$ times every second and produces $2.38{\times}10^{45}$ eV of energy to power the Sun.

The high-energy photons generated by the nuclear fusion at the core then enter the radiative zone, the layer between the core and ~ 0.7 R_s. In the radiative zone, the mean free path of a photon is very short, of the order of a millimeter due to the high density of the plasma. This means that photons are scattered by electrons almost immediately after they are emitted. The scattering of photons randomizes their paths and slows down the outward transfer of energy produced in the core, requiring about $1.7{\times}10^5$ years to reach the outer edge of the radiative zone (Mitalas & Sills, 1992). The energy transfer process by the random walk of photons can be described by a diffusive process, with a heating/cooling rate of the form:

$$Q_{\text{diff}} = \nabla \cdot (\kappa \nabla T). \tag{1.5}$$

Here κ is the radiative conductivity, which in the opaque interior can be written as

$$\kappa = \frac{16\sigma_S T^3}{3\tilde{\kappa}\rho}. \tag{1.6}$$

Here σ_S is the Stefan-Boltzmann constant, and $\tilde{\kappa}$ is the Rosseland mean opacity. The energy balance of the solar interior requires that the radiative diffusion equals energy production at the core, which gives the following relation:

$$-\nabla \cdot (\kappa \nabla T) = \nabla \cdot (\frac{\varepsilon}{4\pi r^2}\vec{r}). \tag{1.7}$$

Here ε is the energy production rate at the core. Therefore the temperature gradient inside the radiative zone can be written as

$$\frac{dT}{dr} = -\frac{3\tilde{\kappa}\rho\varepsilon}{64\pi\sigma_S r^2 T^3}. \tag{1.8}$$

Given the high temperature and low opacity in the radiative zone, Equation 1.8 yields a small temperature gradient, which effectively prohibits convective energy transport in this region. And energy transport in the radiative zone is dominated by radiative diffusion.

1.1.2 The Convection Zone

The outer 30% of the solar interior is composed of turbulent plasma with convective motions, and is referred to as the *convection zone*. Near-surface convection forms cells with hot, upflowing plasma with velocities of 1 km/s surrounded by cool, sinking plasma. At the photosphere the convective cells appear as granules, shown in Figure 1.4, observable over the whole solar disk. The size of the convective cells scales with the local pressure scale height and ranges from a granular scale of the order of 1 Mm to larger than 100 Mm, which are manifest as different flows ranging from several

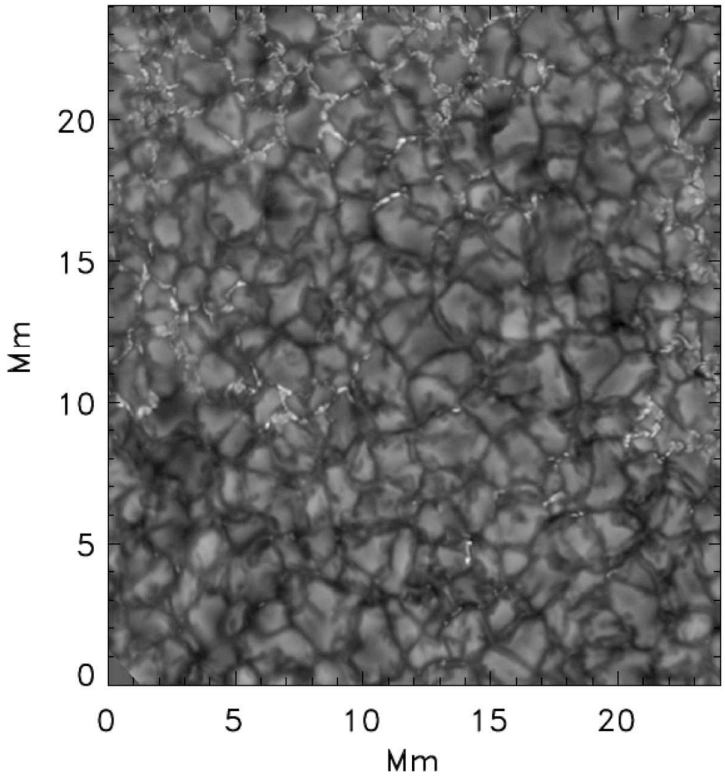

Figure 1.4: Granulation in the G-continuum at the photosphere. From Nordlund et al. (2009).

m/s to km/s (Hathaway et al., 2000). The lifetime of the convective cells, depending on their size, varies from several min (granules) to several weeks (giant cells).

The temperature in the convection zone decreases monotonically from about 2×10^6 to $\sim$ 6000 K, resulting in the recombination of ions with electrons near the top. For example, Figure 1.5 shows the normalized ionization fraction of H, He I and He II, in the uppermost 20 Mm of the convection zone. The ionization fraction of H and He changes from almost unity to zero within this region, resulting in the deviation of Γ, the adiabatic index, from 5/3. The frequent recombination and ionization of particles in the convection zone alters the properties of the plasma away from an ideal gas.

Photons are absorbed more easily with the increasing ionization and recombination rate resulting in a sharp increase in the opacity from bound-free absorption. The

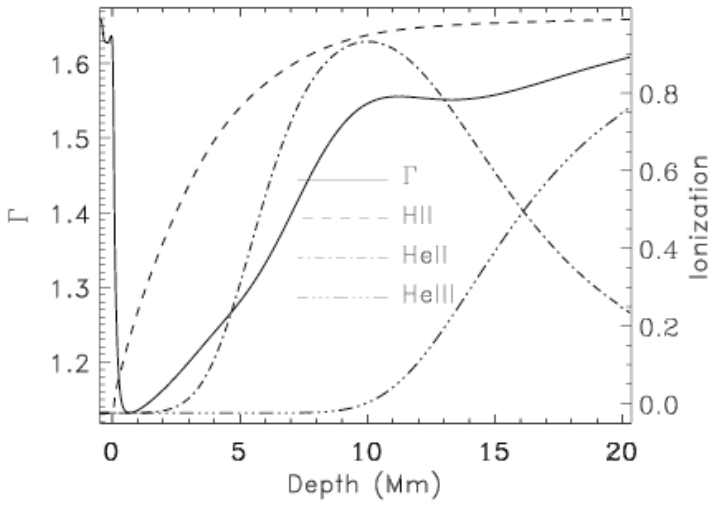

Figure 1.5: The stratification of the normalized ionization fraction of H I, He I, He II and the adiabatic index Γ in the uppermost 20 Mm of the convection zone. From Nordlund et al. (2009).

absolute temperature gradient in the convection zone increases rapidly with increasing opacity. The steep temperature gradient in the convection zone, once exceeding a critical value, drives the convective instability in the plasma, first discovered by *Schwarzschild* (Schwarzschild, 1958). Convective instability sets in when the temperature gradient is larger than the adiabatic lapse rate, written as:

$$|\frac{d\mathrm{T}}{d\mathrm{r}}| > |\frac{d\mathrm{T}}{d\mathrm{r}}|_{ad}, \tag{1.9}$$

which gives

$$\frac{d\mathrm{lnT}}{d\mathrm{lnP}} > \left(\frac{d\mathrm{lnT}}{d\mathrm{lnP}}\right)_{ad} = \frac{\gamma_2 - 1}{\gamma_2}. \tag{1.10}$$

Here γ_2 is Chandrasekhar's second adiabatic exponent, defined as

$$\gamma_2 = \left[1 - \left(\frac{\partial \mathrm{lnT}}{\partial \mathrm{lnp}}\right)_S\right]^{-1}. \tag{1.11}$$

Once the instability ensues, hot plumes from the radiative zone rise, expand, and

reduce the mass density inside the plume. However, the surrounding plasma falls in density and temperature even more rapidly, resulting in the continous rising of the plumes. At the outer edge of the convection zone, the upflowing ions recombine with electrons, due to the decreasing temperature, and release energy by emitting photons during recombination. With low electron density at the surface, the produced photons can escape the surface freely, resulting in the cool down and sinking motion of the plasma. The sinking plasma gets heated up in the convection zone and rises again. The repeated rising and sinking motion of the plasma takes energy from the radiative zone and releases it at the top of the convection zone, resulting in the energy transfer to the surface of the Sun.

While the solar interior cannot be directly observed (with the exception of neutrinos), its structure can be infered from the propagation of pressure waves. Observed at the photosphere as Doppler shifts of of specturm lines, these waves inform us of the conditions of the interior by the variation in propagation time and the frequency of global modes. Such inversion techniques are generally refered to as *helioseismology* (Gough & Toomre, 1991). Helioseismology discovered that differential rotation in the convection zone depends on latitude and depth, as shown in Figure 1.6. The angular velocity of the rotation is almost latitude-independent for layers less than 0.7 R_s from the center, suggesting a uniform rotation of the solar core and the radiative zone. However, in the upper 30% radius of the Sun, there is a tendency of increasing rotation speed with decreasing latitude. Hence, the convection zone at the equator rotates at an angular speed roughly 25% faster than at 60°. The difference in angular speeds in the radiative zone and the convection zone produces a thin shear layer, with thickness of less than 7% in radius (Miesch & Toomre, 2009). The solar magnetic fields are believed to be stored in the tachocline, a thin layer between the convection and radiative zone, and transferred from poloidal to toroidal fields by the differential rotaion (Section 1.2.1). The fine structure of the tachocline results from the coupling

of rotation, shearing, convective downflows, and strong magnetic fields (Miesch & Toomre, 2009), and therefore requires detailed study by both helioseismology and numerical model.

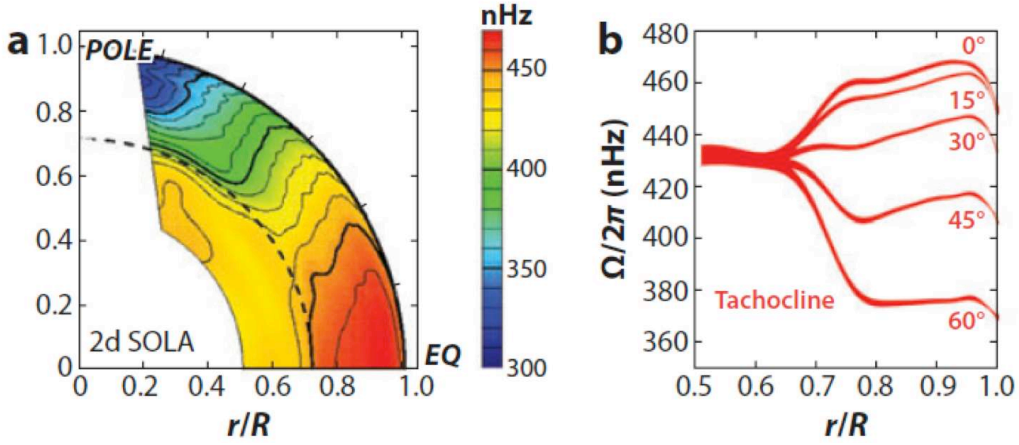

Figure 1.6: (a) The structure of angular velocity on a solar cut plane from helioseismology (b) vertical stratification of angular velocity at different latitudes. From Miesch & Toomre (2009).

1.1.3 The Solar Atmosphere

The photosphere is the layer that emits most solar radiation, and has an effective temperature of 5770 K and a depth of 500 km. Due to the relatively low temperature at this layer, particles are less ionized, and electron densities are lower. Therefore, most photons can escape outward without interruption. The radiant losses at the surface cause the rapid temperature drop from the photosphere to the temperature minimum of about 4100 K.

To describe the radiative cooling/heating, one needs to take into account the transport of photons in the cold surface layers. The radiative cooling/heating rate

can be written as:

$$\begin{aligned} Q_{rad} &= -\nabla \cdot F_{rad} \\ &= \int_{\nu} \int_{\Omega} \rho \kappa_{\nu} \left(I_{\nu} - S_{\nu} \right) d\Omega d\nu, \end{aligned} \tag{1.12}$$

where F_{rad}, ν, Ω, κ_{ν}, I_{ν}, S_{ν} are the radiative flux, frequency, solid angle, absorption coefficient, intensity and source function, respectively. In the thick interior, the mean free path of photons is so short that transport of the photons can be described with simple diffusion. Therefore Equation 1.12 can be written as 1.5. At the photosphere, however, radiation transfer changes rapidly from nearly isotropic diffusion to free streaming, which requires a detailed angular description of the radiation.

Above the photosphere, the plasma gets heated up to about 10^6 K above the chromosphere at the top of the transition region and expands as a supersonic wind from the corona into interplanetary space. Observational evidence (De Pontieu et al., 2009) and numerical simulations (Gudiksen & Nordlund, 2005) suggest that the solar atmosphere is heated up to million degrees within ~ 2 Mm in the corona. Wave and electric-current heating have been proposed as two major methods of transferring the photospheric kinetic energy to coronal internal energy (Kuperus et al., 1981; Walsh & Ireland, 2003; Klimchuk, 2006). Although there is still no concensus on the the physical mechanisms that heat up the plasma within such a short path, observations have demonstrated an empirical power-law relation between the X-ray luminosity and the unsigned magnetic flux at the photosphere (Pevtsov et al., 2003):

$$L = c\phi^{\alpha} \tag{1.13}$$

where c is a constant, ϕ is the unsigned magnetic flux, and $\alpha = 1.15$. This suggests that the heating mechanism is related to the solar magnetic field.

The density drop and temperature increase in the solar corona results in a fully-ionized, optically-thin plasma. Therefore, radiative losses in the corona can be calculated in the optically- thin limit:

$$Q_{rad} = -n_e n_p \Lambda(T) \tag{1.14}$$

where n_e and n_H are the electron and hydrogen number density, respectively. $\Lambda(T)$ is the total radiative cooling curve, calculated from the atomic database consisting of many ions of astrophysical interest under optically thin assumption, e.g. CHIANTI database (Dere et al., 1997, 2009).

1.2 Solar Magnetism

As discussed in Section 1.1.2, large-scale solar magnetic fields are believed to be amplified at the tachocline and buoyantly rise through the convection zone to make their way into the photosphere and solar atmosphere. Observations have shown that the photosphere is penetrated by magnetic fields that are concentrated at kilo-Gauss strengths in structures, such as ephemeral regions and sunspots. Moreover, magnetic features at the surface vary over many timescales, from minutes for small-scale flux emergence, to 11 years of solar cycle-scale magnetic activity. Coronal observations over wide wavelength ranges also show the structure of the magnetic field. Loops and open field regions can be inferred from observations in the EUV spectrum. More importantly, solar magnetic fields display a wide hierarchy of eruptive and explosive activity, releasing significant amounts of energy and mass into interplanetray space (Schrijver, 2010). Intuitive questions arise from the observations: What is the origin of the 11-year cycle? How do the fields become structured? What drives the magnetic activity? Our current understanding of the questions above has advanced greatly by the development of both observational, theoretical and numerical models as discussed

below.

1.2.1 The Solar Cycle and Solar Dynamo

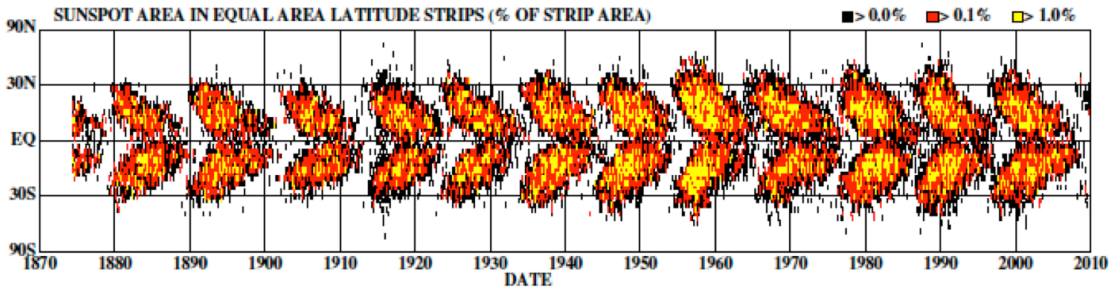

Figure 1.7: Sunspot area in equal area latitude strips as a function of time and latitude From Hathaway (2010).

Discovered by *Samuel Schwabe*, solar activity displays an 11-year cycle of periodic variation in the number of sunspots. As we shall discuss in Section 1.2.2, sunspots are photospheric concentrations of magnetic fields, which originate below the convection zone. It is thus of great interest and importance to study the interior processes that magnetic fields undergo before they approach the surface and display the observed periodic behavior. Since *Schwabe*'s discovery, more sophisticated observations have added more features to the solar cycle, and demonstrated that besides the sunspot number, the following solar properties also vary periodically (Hathaway, 2010):

- sunspot pairs appear at mid-latitude, about 20-25°, and migrates toward the equator as the cycle processes, as shown in Figure 1.7,
- the corresponding leading and trailing sunpots are of opposite polarities in opposite hemispheres, and the current polarity is opposite to the one of the previous cycle, as stated by *Hale's Law*,
- the polarity of the polar fields reverses at the time of sunspot maximum and with a period of 22 years,

- the number of M-, X- class flares (flares with peak flux of 100-800 picometer X-rays near the Earth ranges in $10^{-5} \sim 10^{-4}$, and above 10^{-4} W/m^2, respectively) and CME's is also correlated with the sunspot number,

- the 10.7 cm radio flux of the solar emission correlates well with the sunspot number with a 1-month lag in phase, and the total irradiance, i.e., the solar radiation incident on the Earth's upper atmosphere, also varies with the 11-year cycle,

The cycle-to-cycle reversal of the polarities of sunspots and polar fields illustrates the periodic behavior of the toroidal and poloidal fields: the strengthening of one of them is accompanied by the weakening of the other, and they reverse directions from cycle to cycle. The cyclic regeneration of the magnetic fields therefore requires a solar interior dynamo that can replenish toroidal field by poloidal, and *vice versa*.

The study of the interior magnetism depends mostly on numerical simulations and theoretical developments. We can describe the evident magnetic fields in the solar interior using the induction equation and express it in the following form:

$$\begin{aligned} \frac{\partial \mathbf{B}}{\partial t} &= \nabla \times (\mathbf{u} \times \mathbf{B} - \eta \nabla \times \mathbf{B}) \\ &= \mathbf{B} \cdot \nabla \mathbf{u} - (\nabla \cdot \mathbf{u})\mathbf{B} - (\mathbf{u} \cdot \nabla)\mathbf{B} - \nabla \times (\eta \nabla \times \mathbf{B}). \end{aligned} \tag{1.15}$$

Here η is the magnetic diffusivity. The first term on the right describes the inductive source of the magnetic fields, while the last term is the magnetic sink (Charbonneau, 2010) due to the dissipation of the current. Equation 1.15 reproduces the toroidal fields from the poloidal field given the differential rotation in the convection zone (see Section 1.1.2). We can express differential rotation as:

$$\mathbf{u}(r, \theta) = \mathrm{r}\ \sin\theta \Omega(\mathrm{r}, \theta)\hat{\phi}. \tag{1.16}$$

Here $\Omega(r, \theta)$ is the angular rotation speed dependent on the radius r and latitude θ. $\hat{\phi}$ is the unit vector in azimuthal direction. This gives the first term in Equation 1.15, i.e. the source of the magnetic field as follows:

$$\mathbf{B} \cdot \nabla \mathbf{u} = \left(B_r \frac{\partial u}{\partial r} + \frac{B_\theta}{r} \frac{\partial u}{\partial \theta} \right) \hat{\phi}, \tag{1.17}$$

which successfully generates B_ϕ, i.e. toroidal field from B_r and B_θ, i.e. poloidal field, as a result of the dependency of the rotation speed on r and θ.

What requires more study is how to produce the poloidal or polar fields from the toroidal fields. *Cowling's theorem* (Cowling, 1933) states that a rotationally symmetric magnetic field cannot be maintained by axially symmetric current, so in order to overcome resistive dissipation, additional motions must be considered. Most solar dynamo models incorporate a mean electromotive force ε correlated to the mean magnetic field due to anisotropic turbulent motions in the convection zone, and write the induction equation as (Charbonneau, 2010):

$$\frac{\partial \langle \mathbf{B} \rangle}{\partial t} = \nabla \times \left(\varepsilon + \langle \mathbf{u} \rangle \times \langle \mathbf{B} \rangle - \eta \nabla \times \langle \mathbf{B} \rangle \right). \tag{1.18}$$

With the implementation of the differential rotation and the electromotive force, mean-field dynamo models are then able to produce cyclic behavior of large-scale mean magnetic fields in the solar interior, given a stratification consistent with helioseismic observations. Other models based on shear, buoyant, or flux tube instabilities have also successfully reproduced the poloidal field from the toroidal component as well as the cyclic behavior of the global magnetic fields (Charbonneau, 2010). Moreover, the development of parellel supercomputers has given rise to magnetohydrodynamic (MHD) simulations devoted to capturing the evolution of both solar rotation and global-scale magnetic structures (Miesch & Toomre, 2009; Brown et al., 2010; Ghizaru et al., 2010). The fact that flow speeds 20 Mm below the surface are very

subsonic allows the application of the anelastic approximation, which is a scaled-variable expansion of the MHD system that essentially filters out sound waves (Fan, 2009a). This approximation allows for much larger time steps, making numerical simulations of the solar cycle possible. Figure 1.8 shows the results from the anelastic MHD simulations of Ghizaru et al. (2010), which produce a solar cycle of 30 years and a cycle-to-cycle reversal of the toroidal field in each hemisphere.

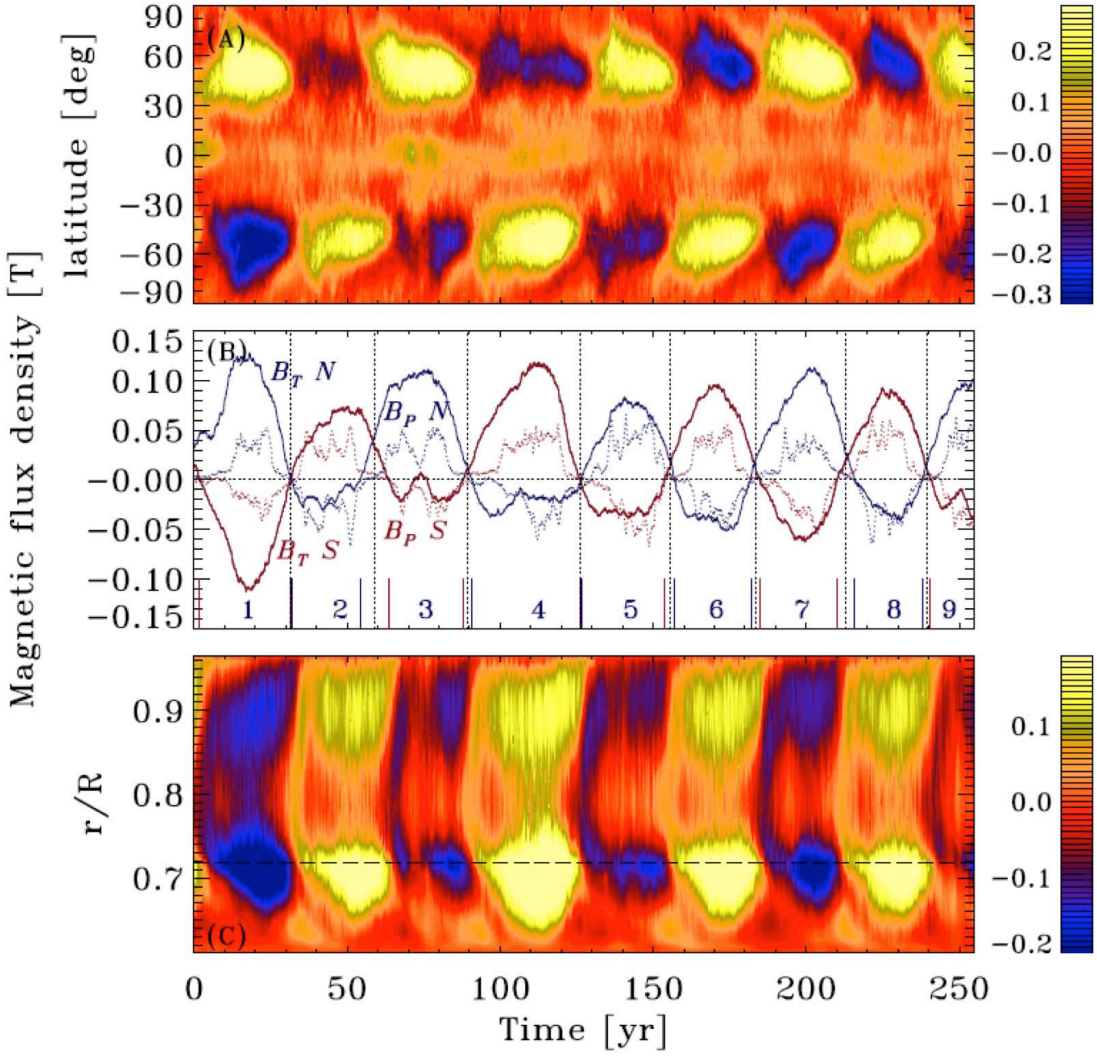

Figure 1.8: (A) butterfly diagram of the toroidal magnetic field at $r/R_s = 0.718$. (B) Temporal evolution of the toroidal field for each hemisphere. (C) Zonally-averaged toroidal field at mid-latitude. From Ghizaru et al. (2010).

The features above vary in more ways than just repeating themselves during each

cycle. They also produce specific characteristics that vary from cycle to cycle (Hathaway, 2010). These variations, e.g. the peak sunspot number during solar maximum, and occasionally-extended times of low activity, have imposed additional constraints to models of the solar cycle and magnetic activity.

1.2.2 The Solar Surface Magnetism

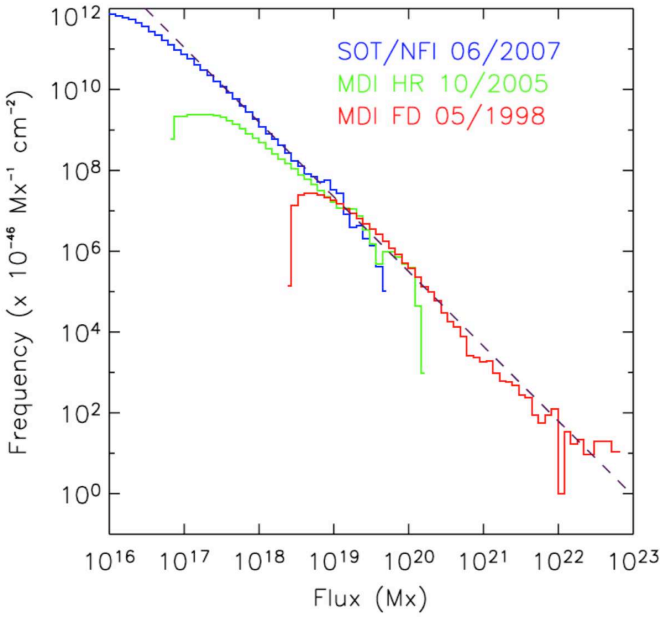

Figure 1.9: Histogram of the magnetic fluxes. From Parnell et al. (2009).

Magnetic fields occur at the surface over a wide range of scales, from ubiquitous ephemeral regions with a unsigned flux of as small as 10^{16} Maxwells, to active regions as large as 10^{23} Maxwells. Due to the limited resolution of current magnetograms, there might also be smaller-scale flux concentration beyond our ability to detect. Statistical study of the probability distribution of the hierarchy of the current observable magnetic features (Hagenaar et al., 2003; Parnell et al., 2009) suggest a uniform power-law distribution for magnetic fluxes ranging from 2×10^{17} to 10^{23} Mx, shown in Figure 1.9:

$$\mathrm{N}(\phi) = \mathrm{N_f}\phi^{-1.85}\mathrm{Mx}^{-1}\mathrm{cm}^{-2}, \tag{1.19}$$

where N(ϕ) is the number of features and $N_f = 3\times10^{-4}$. The observed uniform power-law distribution suggests that either the magnetic structures are produced through the same physical process or they undergo the same subsurface process before they become visible at the surface (Parnell et al., 2009).

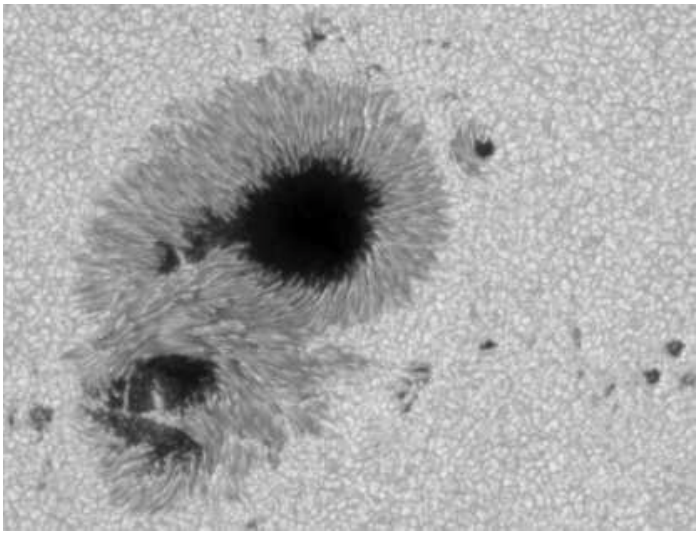

Figure 1.10: Continuum map of the sunspots in AR 10930 observed by Hinode/SOT on Dec 13, 2006.

Among all magnetic features, sunspots are the most outstanding concentrations of magnetic flux (Hale, 1908), with an average field strength of several kG and a lifetime of a few weeks. A typical sunspot contains a compact dark umbra, surrounded by a penumbra, shown in Figure 1.10. Strong magnetic fields suppress convection in sunspots and reduce energy transport, thereby giving an appearance darker than the surrounding surface. In the umbra, the effective black-body temperature is about 4000 K, and the magnetic fields are mostly vertical, while the inclination of the magnetic fields increases with increasing radius, reaching a maximum at the penumbra. In the outer penumbra, the flow pattern demonstates a persistent outflow, called *Evershed Flow*, associated with the horizontal fields.

It is believed that sunspots are magnetic flux tubes rooted deep in the solar convection zone and extending into the atmosphere. However it is still not clear whether

it is a monolithic structure (Cowling, 1957) or a cluster of magnetic flux tubes (Parker, 1979b; Spruit, 1981). Due to the spatial and temporal scales of these structures, most numerical models separate processes in the upper 20 Mm of the convection zone from those in the deep convection zone. Until recently, there was not a numerical model capable of describing both the global stable structure of the sunspot magnetic fields and the detailed fine structures, e.g. umbra dots, dark and bright penumbra filaments. Deep in the solar convection zone, the cross-sectional scale of magnetic flux tubes is much smaller than the local pressure scale height. Thus the thin flux tube approximation can be used to describe its dynamics, by neglecting the variation in the cross section of a magnetic flux tube and assuming instantaneous pressure equilibrium across the tube given the fast sound speed in the interior (Spruit, 1981; Fan et al., 1994; Longcope & Klapper, 1997). This approximation allows one to simulate the dynamic evolution of a magnetic flux tube in a non-magnetized, gravitationally stratified environment. This simple approximation has made remarkable success in reproducing observed properties of active regions such as *Joy's Law* (the variation of the tilt of active regions with latitude). More realistic simulations are now able to reproduce the observed features of sunspots within a thin layer near the visible surface (Rempel & Schlichenmaier, 2011). This advance has been made possible, in part, by increases in computational capability. These types of simulations will be discussed further in Chapter III.

Besides sunspots, there are many smaller-scale magnetic concentrations, such as ephemeral regions and solar pores. These features often appear as smaller dark spots around sunspots as seen in Figure 1.10. They are formed in the supergranular or granular lanes where downflows occur and their evolution is on a much shorter timescale than that of sunspots, normally from hours to days. Sunspots, pores and ephemeral regions, despite their range of sizes, are all local concentrations of strong magnetic fields, with magnetic strength greater than the equipartition strength at the sur-

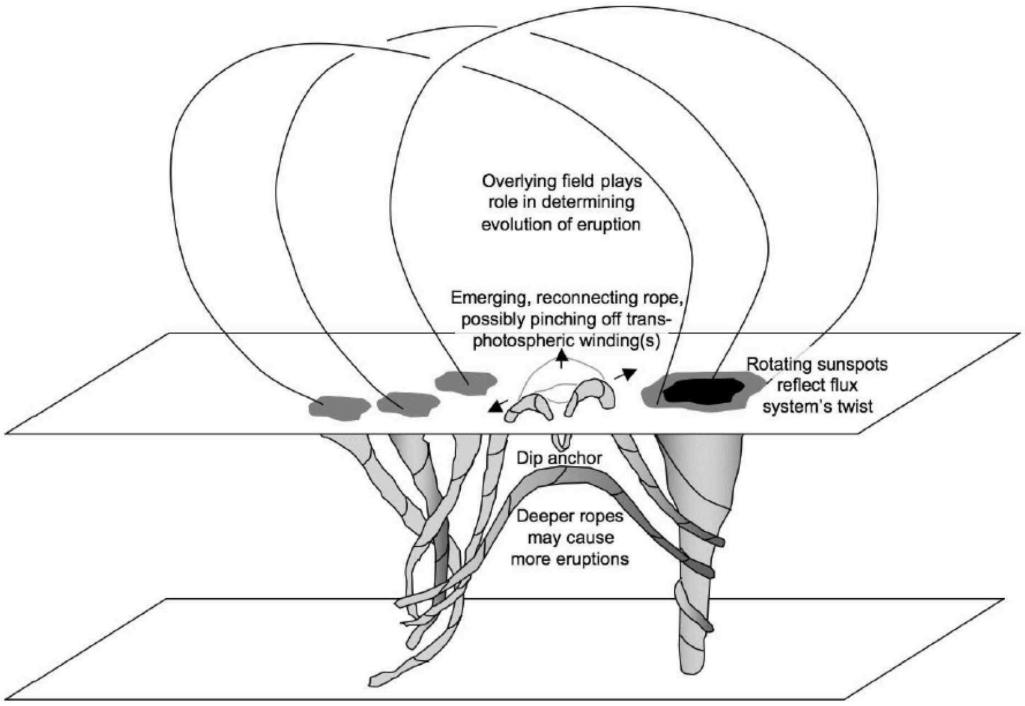

Figure 1.11: Configuration of the emergence of magnetic flux ropes and formation of solar active regions from Schrijver (2009).

face between thermal pressure and magnetic energy $B_{eq} \approx 500$ G. The formation of such strong magnetic fields is facilitated by the convective nature of the near-surface layers: the magnetic field modifies the convective granules producing downward flowing, colder plasma bulbs; the pressure imbalance with the surrounding material thus causes the flux tube to collapse and increases the strength of the magnetic field; and the flux tube approaches equilibrium again with higher magnetic pressure balancing the surrounding material (see Chapter III). This process, called *convective collapse*, was suggested by Parker (1978) and Spruit (1979), as a means of explaining the strength of magnetic fields in the upper convection zone. Both sunspots and pores appear in solar active regions, whose magnetic structure often represent the geometry of a bipolar field, as shown in Figure 1.11 (Schrijver, 2009). The magnetic flux in expanding active regions is maintained by the persistent emergence of bipolar fields from below the convection zone, whose polarities separate after emergence and coa-

lesces into magnetic poles of the same polarity via self-orgnization. The behavior of the magnetic flux emergence will be examined in Chapter II and III.

Unlike the strong local magnetic features, there is a weak field component covering the whole surface of the sun, i.e. the *internetwork field* (Zwaan, 1987). This is composed of mostly horizontal fields, with strength of several hundred Gauss, comparable to B_{eq}. The internetwork field exists at the scale of convective granules, and evolves quite differently from larger-scale magnetic features. The internetwork emerges in clusters of magnetic flux and the poles travel in the same direction, while the polarities of strong field depart from each other (Schrijver & Zwaan, 2000). It is still yet to be determined how the internetwork field is produced, but numerical simulations suggest it is generated through the surface turbulent dynamo (Vögler & Schüssler, 2007).

1.2.3 The Coronal Magnetic Field

Magnetic fields in the photosphere (discussed in Section 1.2.2), fan out in the upper solar atmosphere, forming a magnetic canopy in the chromosphere and overlying coronal magnetic loops. The geometric expansion of magnetic flux leads to a descrease of field strength in the corona. However, thermal pressure of the surrounding plasma falls even faster, which results in a significant decrease of the plasma beta with height. Therefore, in the corona, dynamics is driven by the magnetic field, instead of plasma. At the photosphere, surface flows impose more complexity to the evolution of the magnetic field. Coronal fields react to the changes in the photospheric fields at the Alfvèn speed, and tend to relax to a force-free field, where the current aligns parallel to the magnetic field, as decribed by

$$\nabla \times \mathbf{B} = \mu \mathbf{j} = \alpha \mathbf{B}. \tag{1.20}$$

When $\alpha = 0$, it reduces to a current-free, minimum-ernergy, potential state. However, as the new flux emerges and enters the corona, it may carry with it magnetic non-pontentiality, demonstrated as twist, helicity or shear. How the non-potentiality is produced is still under debate: it might be intrisincally built in the emerging flux and approach the solar atmosphere with the rising motion; or it might be generated by the surface flows, e.g., shearing and rotation motion of the photospheric footpoints of the magnetic flux. The detailed physical processes that build up the magnetic non-potentiality will be examined in Chapter IV. These processes that generate magnetic free energy in the corona, are essential for our understanding of the energetic source of the solar eruptions.

CMEs and flares are the most prominent manifestations of coronal magnetic activity. CMEs release energy up to 10^{32} ergs, and can expel about 10^{15} gm of plasma and $\sim 10^{20}$ Mx of magnetic flux into interplanetary space (Bieber & Rust, 1995) at speeds that can reach 3000 km/s (e.g. Gosling et al., 1990; St. Cyr et al., 2000; Zhang et al., 2004). Solar flares can locally heat up coronal and chromospheric plasma and accelerate energetic electrons and protons to energies greater than 1 MeV. Both CMEs and flares result from the destabilization of the coronal magnetic field. Whether the occurrence of the two phenomena are associated with each other is still unclear. The correlation factor increases with increasing flare strength (Schrijver, 2009), approaching 100% for X3 flares (Yashiro et al., 2005).

In active regions, CMEs and flare eruptions are associated with the release of significant amount of free magnetic energy stored in the coronal fields. The storage of the free energy distingushes the coronal field geometry from the potential field: the non-potential force-free fields are stretched, expanded and intertwined. Such force-free fields in the solar corona have historically been taken to be of two forms: (a) arcades, in which the foot points have been sheared to produce a strong field component parallel to the Polarity Inversion Line (PIL); and (b) flux ropes, in which the

magnetic field is twisted about a central axis. Plentiful observations provide evidence for both arcades and flux ropes as the coronal field structures for CMEs. Sheared magnetic fields are measured directly at the photosphere with vector magnetographs (e.g. Hagyard et al., 1984; Zirin & Wang, 1993; Falconer, 2001; Yang et al., 2004; Liu et al., 2005), where the field is found to run nearly parallel to the PIL. More recent analysis by Schrijver et al. (2005) found that shear flows associated with flux emergence drove enhanced flaring. Similarly, active region CME productivity is also strongly correlated with magnetic shear, as shown by Falconer et al. (2002, 2006). There is also evidence suggesting that flux ropes may completely emerge through the photosphere to reside in the corona. Leka & Steiner (2001) examined a time series of vector magnetograms of emerging magnetic flux and found that magnetic fields passing through the photosphere are already twisted. Similarly, Lites et al. (1995) examined a time series of photospheric vector magnetograms, which they found could be fitted by the emergence of a spherically shaped magnetic flux rope. Lites (2005) shows an example of the photospheric vector magnetic field and chromospheric structure seen in the Hα line that suggests the presence of a coronal flux rope associated with a prominence.

The dichotomy of field configurations naturally leads to two broad groups of theoretical and numerical models of the coronal magnetic activity (Forbes et al., 2006). In the case of magnetic arcades, initial configurations are typically taken to be line-tied to the lower boundary and subsequently energized with prescribed shear flows, which cause the arcade to expand and then erupt, forming flux ropes (e.g. Steinolfson, 1991; Mikic & Linker, 1994; Amari et al., 1996; Guo & Wu, 1998). Another variant, the so-called breakout model, involves a system of quadrupolar fields with a system of three arcades. The field reverses direction over the central arcade allowing magnetic reconnection to annihilate it (e.g. Antiochos et al., 1999; Lynch et al., 2004, 2008; van der Holst et al., 2009). In all of these cases, magnetic flux ropes form during

the eruption process and are expelled from the corona. For those models, which assume that flux ropes exist prior to the eruption, the flux ropes are assumed to reside within an arcade where the outward-directed Lorentz force of the rope (hoop force) is balanced by magnetic tension of the surrounding arcade (e.g. Forbes & Isenberg, 1991; Low, 1994; Titov & Démoulin, 1999). The central question with flux rope models is how the force imbalance occurs and results in eruption. Flux ropes have been energized by the application of rotational motions at the rope footpoints (e.g. Tokman & Bellan, 2002; Rachmeler et al., 2009) that twist up the field. Flux ropes have also been forced to emerge into the corona by advecting them through the lower boundary of the computational domain (e.g. Török & Kliem, 2005; Fan, 2005). In the case of Amari et al. (2003), flux cancellation at the PIL forms a flux rope within a sheared magnetic arcade. Following these formation processes, the flux rope may lose equilibrium and erupt from several instabilities including: unbalance of magnetic forces, which is followed by magnetic reconnection (Forbes & Isenberg, 1991; Amari et al., 2003; Roussev et al., 2004), torus instability (Török & Kliem, 2005), or kink instability (Sturrock et al., 2001; Fan, 2005).

1.3 MHD Simulations

The behavior of magnetized plasma can be described by the system of equations of MHD, which combines a set of fluid equations and Maxwell's equations. The MHD equations describe the bulk transport of the plasma and the magnetic flux as a coupled system. This treatment assumes near Maxiwellian particle distribution and excludes charge separation and high frequency phenomena. However, since we consider the slow movement in a relatively dense atmosphere, this approximation is valid. The MHD equations therefore can describe the interaction of the plasma with the magnetic fields, which is essential if we are to understand the physics of the physics of the solar convection zone. As discussed in Section 1.2.1, the MHD

equations can be simplified to the anelastic approximation in the high-β region of the deep convection zone, where the plasma is almost adiabatic and the flow speed is much smaller than the accoustic speed (Fan, 2009a). Anelastic MHD simulations prove to be very useful to study the rise of the magnetic flux tube from the base of convection zone (Fan, 2008; Jouve & Brun, 2009). These global scale simulations address how magnetic fields generated at the tachocline pass through the convection zone and have explained and reproduced many large-scale aspects of sunspots (e.g. Spruit & van Ballegooijen, 1982; Abbett et al., 2001; Fan, 2008). However, because of the anelastic approximation, these models are only applicable to a height of 20 Mm below the photosphere. As we move up to the near-surface layers, i.e. the upper 20 Mm of the convection zone, the properties of the plasma deviate significantly from the interior (see Section 1.1.2), therefore the anelastic approximation becomes insufficient to describe the compression or expansion of the plasma and magnetic flux tubes and flow speeds comparable with the sound speed. In this case, fully compressible MHD equations are required in order to properly capture the interaction of the magnetic flux and the plasma at the surface layers.

1.3.1 Ideal MHD

We derive the ideal MHD equations under the following simplifying assumptions (Gombosi, 1998):

- the plasma is in local thermodynamic equilibrium (LTE),
- electron heat conduction is negligible,
- the plasma is charge-neutral,
- the fluid has infinite conductivity,
- the displacement current is negligible in the Ampère's law.

In this approximation, we can write the MHD equations as:

$$\frac{\partial \rho}{\partial t} + \nabla \cdot (\rho \mathbf{u}) = 0, \tag{1.21}$$

$$\frac{\partial (\rho \mathbf{u})}{\partial t} + \nabla \cdot \left[\rho \mathbf{u}\mathbf{u} + \left(p + \frac{\mathbf{B}\mathbf{B}}{8\pi} \right) \mathbf{I} - \frac{\mathbf{B}\mathbf{B}}{4\pi} \right] = \rho \mathbf{g}, \tag{1.22}$$

$$\frac{\partial E_{tot}}{\partial t} + \nabla \cdot \left[\left(E_{tot} + p + \frac{\mathbf{B} \cdot \mathbf{B}}{8\pi} \right) \mathbf{u} - \frac{(\mathbf{u} \cdot \mathbf{B})\mathbf{B}}{4\pi} \right] = 0, \tag{1.23}$$

$$\frac{\partial \mathbf{B}}{\partial t} + \nabla \cdot (\mathbf{u}\mathbf{B} - \mathbf{B}\mathbf{u}) = 0, \tag{1.24}$$

where ρ, $\mathbf{u}$, E_{tot}, p, $\mathbf{B}$ are the mass density, velocity, total energy density, plasma pressure and magnetic field respectively. And the total energy density includes the internal energy e, the kinetic energy and the magnetic energy:

$$E_{tot} = e + \rho \frac{\mathbf{u} \cdot \mathbf{u}}{2} + \frac{\mathbf{B} \cdot \mathbf{B}}{8\pi}. \tag{1.25}$$

For an ideal gas with $\gamma = 5/3$, the internal energy can be written as:

$$e = \frac{3}{2} p \tag{1.26}$$

In order to desribe the temporal and spatial variation of the magnetic fields and the plasma, one needs to solve the MHD equations with discretization in the spatial and temporal dimensions. The spatial resolution has to be determined by the scale of the gradient of the physical properties to avoid numerical diffusion, which leads to a necessity of very fine grid structure in the photosphere to capture the small-scale magnetic concentrations and the sharp gradient in density and temperature, as shown in Figure 1.3. It is advantageous to have a coarse grid both in the corona and convection zone where structures are larger and sound speeds are higher. High spatial resolution in the deep convection zone will over-resolve large structures and reqire a small timestep, given the fast accoustic speed in the hot plasma. In the

corona, the structures are generally large, and the timestep is typically controlled by the fast magneto- accoustic wavespeed. Thus decreased resolution in this region can also mitigate overly restrictive timesteps. In this way, numerical simulations with uniform grids are waste of computational resources when studying magnetism from the convection zone to the atmosphere. In light of this problem, the application of non-uniform grids can save computational resources while retaining the necessary refinement to resolve local turbulent structures at the photosphere.

Over the past decades, fully compressible MHD models have been employed to simulate the emergence of magnetic fields from the near surface convection zone into the lower corona. Shibata et al. (1989) describes a two-dimensional (2-D) simulation on the emergence of a horizontal magnetic flux rope from the photosphere into the chromosphere using a two-layered atmosphere. Moreno-Insertis & Emonet (1996), Emonet & Moreno-Insertis (1998) and Dorch & Nordlund (1998) use 2-D and three-dimensional (3-D) MHD models respectively to study the buoyant rise of magnetic flux tubes through a stratified model convection zone and find that a random or twisting component of the magnetic field along the tube was necessary for the structure to remain coherent during its ascent. During the emergence of magnetic flux in the layers, shearing motion driven by the Lorentz force (Manchester & Low, 2000) draws the magnetic field parallel to the PIL, as demonstrated in simulations (Fan, 2001; Magara & Longcope, 2003; Abbett & Fisher, 2003; Manchester et al., 2004; Archontis & Török, 2008; MacTaggart & Hood, 2009). Furthermore, the energy transport of shear flows naturally provides an energy source for CMEs (Manchester, 2007, 2008). Simulations have also revealed that shear flows driven by the Lorentz force can produce eruptions in both magnetic arcades (Manchester, 2003) and emerging flux ropes (Manchester et al., 2004; Archontis & Török, 2008; MacTaggart & Hood, 2009), providing further evidence of a mechanism for CMEs, flares and filament eruptions. Galsgaard et al. (2007), Archontis & Török (2008), and MacTaggart & Hood

(2009) produce fast CME-like eruptions by also invoking magnetic reconnection with emerging flux ropes. Our understanding of the dynamics and energetics of the solar magnetic activity has been greatly improved by MHD models.

1.3.2 Radiative MHD

The physical conditions in the near-surface layers and the atmosphere of the Sun, discussed in Section 1.1.2 and 1.1.3, requires a more realistic treatment of thermodynamic processes (Stein & Nordlund, 2000; Nordlund et al., 2009). While much can be learned from ideal MHD models, they are limited by simplifications in describing the complex energetics of the solar atmosphere. For example, with an artificially-imposed thermodynamic stratification or an adiabatic energy equation, the plasma contained in an emerging flux rope will cool dramatically as the flux tube expands, and will unphysically inhibit the tube's emergence. In light of this, and other limitations inherent to idealized models, it is desirable to include in the models the additional thermodynamic processes necessary to improve the realism of the simulations. Radiative loss at the surface and in the corona , and the heating at the corona must be included in Equation 1.23 to describe the energy transfer. We can rewrite the energy equation as:

$$\frac{\partial E_{tot}}{\partial t} + \nabla \cdot \left[\left(E_{tot} + p + \frac{\mathbf{B} \cdot \mathbf{B}}{8\pi} \right) \mathbf{u} - \frac{(\mathbf{u} \cdot \mathbf{B})\mathbf{B}}{4\pi} \right] = Q_e, \tag{1.27}$$

where Q_e on the right hand side denotes a radiative source term. An accurate treatment of the Q_e term requires solving Equation 1.12 (see Stein & Nordlund, 2000; Vögler et al., 2005; Cheung et al., 2007; Martínez-Sykora et al., 2008a; Rempel et al., 2009).

In addition to radiative transfer, the ionization and excitation of particles in the upper convection zone contribute 2/3 of the enthalpy flux at the solar surface (Stein

& Nordlund, 2000). This enthalpy flux can be taken into account by implementing a non-ideal equation of state (EOS) (see Section 1.1.2), instead of Equation 1.26. Tabular equations of state have been developed over large temperature and density ranges using multiple atomic species. For example, the OPAL EOS (Rogers, 2000) provides pressure, internal energy, entropy, adiabatic indexes and specific heat values as functions of temperature and density. The application of the tabular EOS offers a precise description of the thermodynamic state of the plasma in the convection zone, which allows us to update the pressure from the internal energy e and density ρ by $p = p(e, \rho)$.

Numerical models that take into account thermodynamic processes have produced a more realistic convection zone overlaid by a self-consistent upper atmosphere (Vögler et al., 2005; Stein & Nordlund, 2006; Hansteen et al., 2006; Abbett, 2007; Gudiksen et al., 2011). Such realistic simulations reveal a wealth of complex dynamic interactions between the magnetic field and the convective flows. Cheung et al. (2007) and Tortosa-Andreu & Moreno-Insertis (2009a) studied the rise of buoyant magnetic flux tubes from the near-surface convection zone into the photosphere and chromosphere and found convective flows played a fundamental role in the emergence of magnetic flux at the photosphere. Cheung et al. (2007) and Martínez-Sykora et al. (2008b, 2009) simulated an emerging flux tube, and found that it increases the size of photospheric granules and alters chromospheric structure. Radiative MHD simulations on a larger scale (Rempel et al., 2009; Cheung et al., 2010) are able to simulate sunspots and active regions. More discussion on the interaction between the magnetic field and the convective flows can be found in reviews by Fan (2004) and Nordlund et al. (2009).

However, solving the radiative transfer equation becomes computationally expensive when we are considering simulations covering the near-surface layers and the corona, therefore approximations have been made to simplify the radiative transfer

while still adequately describing radiative cooling. Abbett (2007) writes the energy source term as:

$$Q_e = Q_{rad} + Q_{cr} + Q_{damp}. \tag{1.28}$$

Here, Q_{damp} is the energy loss due to an optional velocity damping term in the momentum equation to suppress the fast moving vertical shocks, to speed up the relaxation of the background atmosphere. The optional damping term changes Equation 1.22 to:

$$\frac{\partial(\rho\mathbf{u})}{\partial t} + \nabla \cdot \left[\rho\mathbf{u}\mathbf{u} + \left(p + \frac{\mathbf{B}\mathbf{B}}{8\pi}\right)\mathbf{I} - \frac{\mathbf{B}\mathbf{B}}{4\pi}\right] = \rho\mathbf{g} - \frac{\rho u_z}{\tau}, \tag{1.29}$$

where τ represents a time scale over which the optional artificial vertical damping is applied. This velocity damping term results in the following damping in energy:

$$Q_{damp} = -\frac{\rho u_z^2}{\tau}. \tag{1.30}$$

Q_{rad} is the optically thin radiative loss term. In the solar corona, high-temperature low-density plasma dominates. Radiative losses in the optically-thin limit can be expressed as Equation 1.14. We approximate optically-thick surface cooling by artificially extending the optically-thin cooling curve to lower temperatures. This treatment leads to physical results if calibrated against more realistic simulations, where the LTE radiative transfer equation is solved in detail (Bercik, 2002; Stein & Nordlund, 2000). Q_{cr} is the coronal heating term, from the empirical law in Equation 1.13. Assuming that the heat deposited in the corona is proportional to the local magnetic field strength, an empirically-based coronal heating function can be written as:

$$Q_{cr} = \frac{c\phi^{\alpha}|B|}{\int BdV}. \tag{1.31}$$

Here, ϕ is the unsigned magnetic flux at the photosphere; B is the magnetic field strength; $\int BdV$ represents the magnetic field strength $|B|$ integrated over the region

above the model photosphere; and c and α are constants with values of 89.40 and 1.15, respectively, in CGS units (see Abbett 2007). We note that the model corona could be heated via Joule dissipation in a manner similar to Martínez-Sykora et al. (2008a). With these additional source terms, Equations 1.21, 1.29,1.27 and 1.24 together provide an approximate radiative MHD description of the magnetic fields and the plasma in the near-surface layer and atmosphere. While we realize that heating due to electron thermal conduction along the magnetic field is a crucial contributor to the energy balance of the corona, our focus here is on the dynamic emergence of magnetic flux lower in the atmosphere. We do not attempt to realistically model the thermodynamics of the corona, thus we choose to neglect the effects of thermal conduction in order to allow for a more thorough exploration of parameter space.

CHAPTER II

Near-surface Magnetic Flux Emergence

Magnetic fields play an important role in driving solar and heliospheric activity (see Section 1.2). In spite of the wide range of magnetic flux in the solar magnetic features, the probability distribution of the flux present a uniform power law for fluxes between 2×10^{17} and 10^{23} Mx (Parnell et al., 2009). The uniform probablity distribution suggests a uniform generation or post-processing at the near-surface layers for the magnetic features. In light of this observation, great effort has been devoted to study the formation of the magnetic features at the solar surface by the magnetic flux emergence from the convection zone.

One way to make progress is to use MHD models to study different aspects of the emergence process. As discussed in Section 1.3.1, ideal MHD simulations have been carried out on the emergence of the magnetic flux from the convection zone (Shibata et al., 1989; Emonet & Moreno-Insertis, 1998; Dorch & Nordlund, 1998; Abbett & Fisher, 2003). They find a random or twisting component of the magnetic flux is necessary for coherent emergence. Recent 3-D MHD simulations of flux emergence in a computational domain containing both the upper convection zone and corona (Fan, 2001; Magara & Longcope, 2003; Archontis et al., 2004; Manchester et al., 2004) illustrate the importance of surface forces during the emergence process. In particular, Manchester et al. (2004) found that magnetic tension forces drove shear flows and

facilitated the flux tube's emergence and partial eruption. This shearing process was discovered in Manchester & Low (2000) and first illustrated with time-dependent numerical simulations in Manchester (2001). However, in ideal MHD simulations, as discussed in Section 1.3.1, the magnetic fields undergo unphysical processes due to the absence of physical thermodynamic processes, such as over-expansion with the adiabatic cooling of the plasma.

Recent increase in computing power allows MHD models to include a more realistic treatment of energy transfer through the solar convection zone into the corona. Details of radiative MHD models are discussed in Section 1.3.2. It is clear in these models that surface convection driven by radiative cooling dramatically impacts magnetic structures both above and below the visible surface (Stein & Nordlund, 2000; Vögler et al., 2005; Cheung et al., 2007; Martínez-Sykora et al., 2008a; Rempel et al., 2009). We therefore set out to improve the treatment of the energy equation in the 3-D MHD model (Fang et al., 2010) with the Block Adaptive-Tree Solar-wind Roe Upwind Scheme (BATSRUS) developed at the University of Michigan (Powell et al., 1999; Tóth et al., 2012). We use the energy treatment described in Section 1.3.2 to study the physics of flux emergence in a combined convection zone-to-corona system. The study here focus on the effect of near-surface turbulent convection has on the emerging structure, and whether the shear flows described in Manchester et al. (2004) continue to be the principle drivers of magnetic flux emergence and energy transfer in a radiatively dominated regime.

2.1 Simulation Steps

With source terms for radiative cooling (Equation 1.12), coronal heating (Equation 1.31), and optional damping (Equation 1.30) of vertical flows, the MHD equations consist of Equation 1.21, Equation 1.29, Equation 1.27 and Equation 1.24. Within BATSRUS, we solve the MHD equations in conservative form using a second order-

accurate Total Variation Diminishing (TVD) scheme on a block-adaptive Cartesian grid using the seven characteristic waves scheme of Sokolov et al. (2008). To model solar-like convective turbulence, we must also use a non-ideal, tabular equation of state to close the MHD system. For these simulations, we use the OPAL repository (Rogers, 2000) and set the abundance ratios to solar values. Specifically, we set $X = 0.75$, $Y = 0.23$, and $Z = 0.02$, where X, Y, and Z refer to the mass fractions of hydrogen, helium, and other metals respectively.

2.1.1 Background Solar Atmosphere

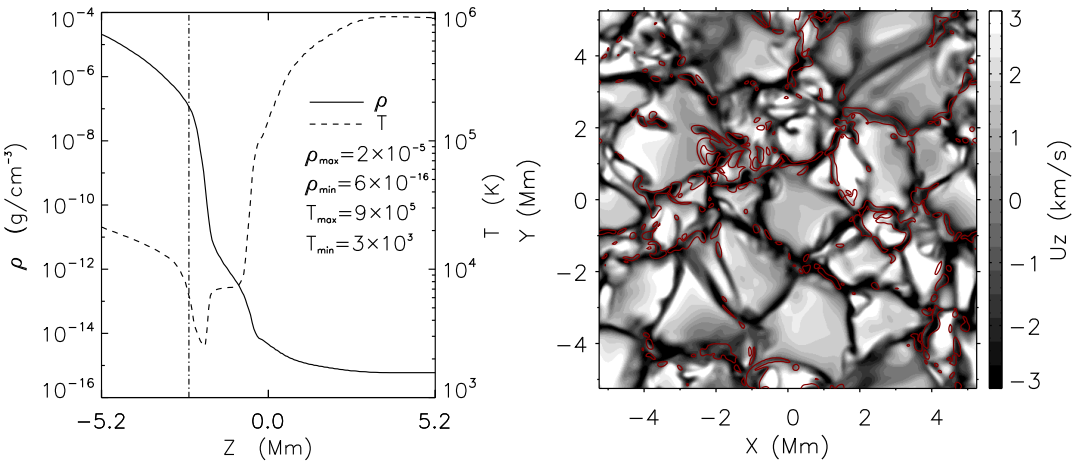

Figure 2.1: Left: The average vertical density (solid) and temperature (dashed) stratification. The dash-dotted line indicate the height where the density and temperature values (1×10^{-7} g/cm^3, 5730 K) are comparable with photospheric values. Right: The vertical velocity structure at the photosphere (z = -2.5 Mm). Red lines show regions with $|B_z|$ greater than 3G.

Magnetic fields presumably must travel through the convection zone after their formation near the sheared tachocline. It is important to understand the interaction of these fields with convective eddies during their ascent before they reach the photosphere where they are observed (see e.g., the review by Fisher et al. 2000). However, local processes near the surface also contribute to the observed evolution of the magnetic field. For example, the MHD quiet sun simulations by Nordlund et al. (1992)

found that most of the generated magnetic field appeared as coherent flux tubes in the vicinity of strong downdrafts. The small-scale convective dynamo in granules can maintain a disordered, locally intense magnetic field, which may contribute to the formation of ephemeral regions (Cattaneo et al., 2003).

To study the effects of convective motion on flux emergence, we need to generate a realistic solar atmosphere with a superadiabatic stratification below the model photosphere, following the approach of Abbett (2007). We start our simulation by building up a long rectangular domain with dimensions of $0.75 \times 0.75 \times 15$ Mm^3, initialized with uniform temperature and density. The domain is periodic in the horizontal directions. At the lower vertical boundary, we modify the standard symmetric boundary conditions to allow for energy inflow. The top boundary is closed to prevent mass inflows. With these boundary conditions, we allow the initially isothermal model atmosphere to evolve self-consistently in response to gravitational forces and radiative cooling, and relax to a convectively unstable stratification below the surface, coupled to a cold, evacuated upper-atmosphere. The solar-like subsurface stratification is achieved by adjusting the density and temperature cutoffs of the extended cooling curve and the energy input at the base of the model convection zone until the resulting atmosphere matches that of Bercik (2002) and Abbett (2007) as well as possible.

We then use this solution as the initial state of a 3-D simulation with a domain of dimensions of $10 \times 10 \times 15$ Mm^3, which is comparable to the size of an ephemeral region on the sun. Within this superadiabatic background atmosphere, convective motion then can be initiated by breaking the symmetry with a small random energy perturbation applied to the subsurface portion of the computational domain. In our simulations, we obtain solar-like convective structures with convective granules of upward velocity, up to 6 km/s, surrounded by narrow intergranular lanes of downward velocity up to 6 km/s, shown by the gray-scale image in the right panel of Figure 2.1.

To build a magneto-convective state, we introduce a horizontal magnetic field, $B_x = 1$ G, into the region below the surface, while other regions are initially field-free. The magnetic energy is less than 0.001% of the kinetic energy of the turbulent motion, which dominates the dynamics in this case. Over time, the field is stretched and amplified by convective motions, and flux becomes concentrated in intergranular lanes, shown by red lines in the right panel of Figure 2.1, without noticeable deformation of the granular convection. Since the focus of our study here is not the study of the convective dynamo, we also experiment with stronger initial mean fields to more quickly build up semi-realistic models of magneto-convection.

We then put a 1 G vertical magnetic field into the domain to heat the corona by activating the empirical magnetic-flux-related coronal heating term Q_{cr} (Equation 1.31), and open the upper boundary to allow waves to travel outward. The vertical variation of the relaxed atmosphere is described in the left panel of Figure 2.1, which shows average density and temperature plotted as functions of height. At $z = -2.5$ Mm, the density and temperature values (1×10^{-7} g/cm^3, 5730 K) are comparable with the observed values of the photosphere, and thus, this layer is defined in our simulations as the solar surface.

2.1.2 Magnetic Flux Rope

After the generation of a realistic convective state and overlying atmosphere, we insert a thin, horizontal twisted flux rope into the model's convection zone. Following Fan (2001) and Manchester et al. (2004), we describe the initial flux rope by

$$\mathbf{B_0} = B_0 e^{-r^2/a^2} \hat{\mathbf{x}} + qr B_0 e^{-r^2/a^2} \hat{\theta}, \tag{2.1}$$

where we set the radius of Gaussian decay $a = 0.3$ Mm. q is the twisting factor defined as the angular rate of field line rotation per unit length in the axial direction.

The density is depleted in the central section of the flux rope, which produces an Ω-loop structure by buoyancy using:

$$\rho = \rho_0(1 - \eta e^{-x^2/\lambda^2}), \tag{2.2}$$

where the length of the buoyant section $\lambda = 1.5$ Mm, and the ratio η is defined as

$$\eta = \frac{\frac{1}{2}\left[B_0 e^{-r^2/a^2}\right]^2 \left[-1 + \frac{1}{2}q^2(1 - \frac{2r^2}{a^2})\right]}{p_0}, \tag{2.3}$$

which maintains force balance.

To make the total energy unchanged, we correct the pressure by:

$$p = p_0(1 - \eta). \tag{2.4}$$

2.2 Simulation Results

Results from our simulations are presented as follows. In Section 2.2.1, we describe the overall structure developed during the course of the emergence of three different flux ropes. In Section 2.2.2 we discuss the shearing motion during the emergence process, and finally in Section 2.2.3 analyzes a particular case of "U-loop" formation.

2.2.1 Emergence of the Flux Rope

Table 2.1: Parameters for runs

runs	q	B_0 (kG)
1	-1.0	7.0
2	-1.5	7.0
3	-1.5	14.0

In the sections below, we experiment with different twisting and magnetic strength

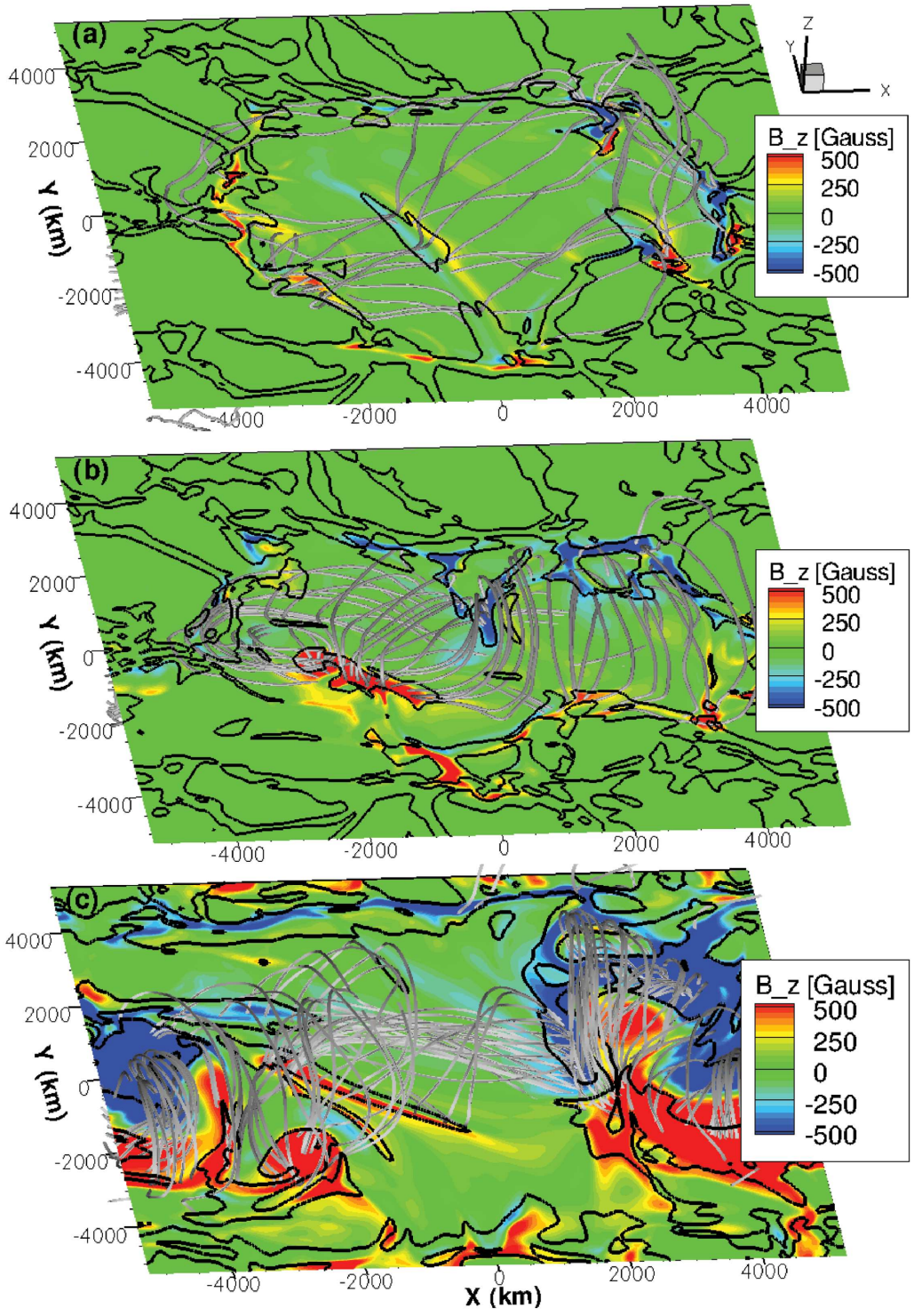

Figure 2.2: The 3-D structure of magnetic field of Run 1 (a), Run 2 (b) and Run 3 (c) at t = 20, 20, 16 min, respectively. The planes show the B_z on photosphere. Black lines outline regions with downflow speed greater than 1km/s. Flux ropes with more twist or strength have less horizontal expansion and more coherence during emergence.

values shown in Table 2.1 and evaluate their role in affecting the emergence. At the photosphere, the flux rope first emerges as two closely-aligned flux concentrations with opposite polarities. Then these two polarities start to separate from each other since the buoyant section continues to rise and expand at the photosphere. Figure 2.2 shows the 3-D structure of magnetic fields for each run, with the color showing the photospheric B_z field, and black lines marking downdrafts with speed greater than 1 km/s. For Run 1, with a weak field $B_0 = 7.0$ kG and low twist $q = 1.0$, we observe little coherency in the emerging flux rope, which expands preferentially in the horizontal direction. The horizontal expansion occurs 0.5 Mm above the photosphere, at the temperature minimum, under force imbalance due to the sharp decrease in the thermal pressure of the surrounding atmosphere. And on the photosphere, convective motion dominates over the rising motion of magnetic flux, as seen in Panel (a) of Figure 2.2. The twisting factor was increased in Run 2, and a coherent flux rope was observed in the lower corona after emergence, shown in Panel (b). In Run 3, both twisting factor and flux rope strength are increased compared with Run 1. We find that the increase of a non-axial component of the initial magnetic field (Panel (c) of Figure 2.2) enhances coherency, and prevents the emerged rope from over-expansion in the horizontal direction, as shown in Panel (a). Turbulent plasma flows distort the flux rope during its rise, while a flux rope with strong magnetic field deforms the convective granules after emergence, consistent with Cheung et al. (2007). However, regardless of the deformation, the strong vertical magnetic fields concentrate in the downdrafts after fully emerging above the surface. In the following sections, we will analyze Run 3 in detail.

2.2.2 Shearing Motion

Photospheric shearing motions have long been observed to be in strong association with solar flares and CMEs (e.g., Meunier & Kosovichev 2003; Yang et al. 2004;

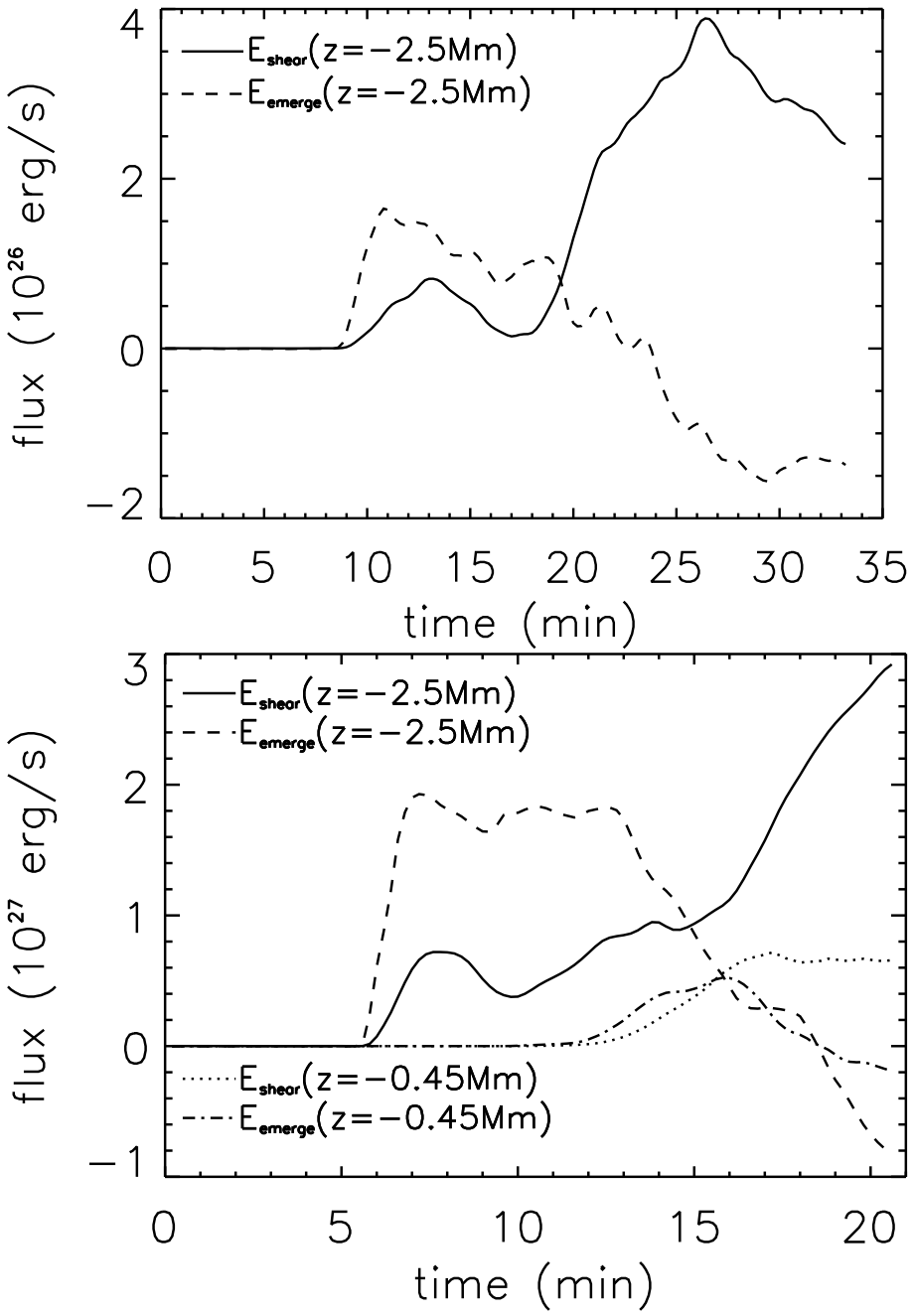

Figure 2.3: The evolution of sheared (solid) and emerged (dashed) energy flux at the photosphere for Run 2 (left) and Run 3 (right). In the bottom panel, dotted and dash-dotted lines show the evolution of shear and emerged fluxes, respectively, at z = -0.45 Mm.

Schrijver et al. 2005). Besides the photospheric motion, Athay et al. (1985) found a shearing area in the transition region and upper chromosphere. Helioseismic flow

maps (Kosovichev & Duvall, 2006) also indicate that the magnetic energy buildup prior to CMEs is driven by the strong shearing flows with speed 1-2 km/s at the depth of 4-6 Mm below the surface.

In our simulations, coherent shearing flows develop below the photosphere and extend into the lower corona in the later phase of emergence. We calculate the components of the Poynting flux associated with horizontal and vertical motions on the photosphere by:

$$E_{\rm shear} = -\int \frac{1}{4\pi} \left(B_x u_x + B_y u_y\right) B_z dS, \tag{2.5}$$

$$E_{\rm emerge} = \int \frac{1}{4\pi} \left(B_x^2 + B_y^2\right) u_z dS. \tag{2.6}$$

The temporal evolution of the energy fluxes is shown in Figure 2.3. In Runs 2 and 3, the top of the flux rope reaches the photosphere at times $t = 9.5$ and 5.5 min, respectively, shown in Figure 2.3. When the magnetic field first emerges at the surface, a simultaneous increase in sheared and emerged energy flux occurs, with a greater increase in emerged flux. The emerging motion dominates the energy flux for the first 10 minutes, during which the buoyant part of the flux rope evolves to a fully emerged state. Afterwards, near the surface, the magnetic pressure gradient force is balanced by gravity and gas pressure, which slows down the emergence and decreases the emerged energy flux after the saturation of emergence. The emerged energy flux drops to negative values in the later phase due to the concentration and subduction of the magnetic field in downdrafts. Dotted and dash-dotted lines in bottom panel of Figure 2.3 show the shear and emerged energy fluxes, respectively, in lower corona, 2.05 Mm above the photosphere, which has a temporal delay of 6 min but represents a similar trend as the fluxes at the photosphere.

When the rising motion succumbs to photospheric downflows, the main energy release into the overlying atmosphere is contributed by the shear flow, which continues

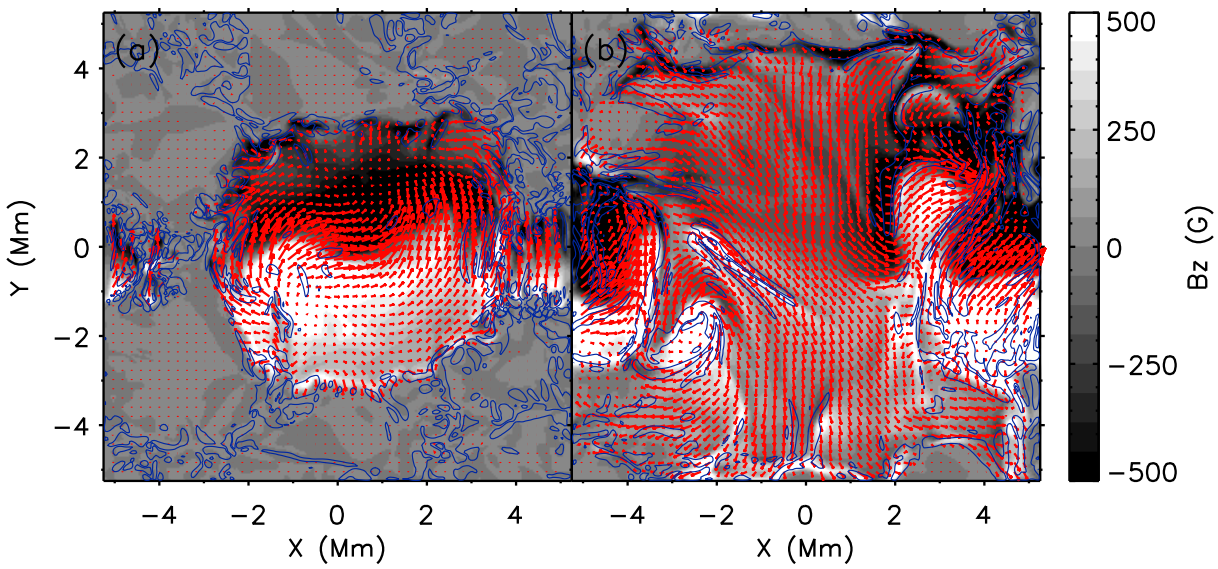

Figure 2.4: The vertical magnetic field structure on the photosphere at times $t = 10$ (a) and 15 (b) min for Run 3. Blue lines show regions with $|(\nabla \times \mathbf{u})_z|$ greater than 1.5 times of the average value. The horizontal magnetic field is shown by the red arrows. The locations of strong PILs show a good coincidence with regions with higher $|(\nabla \times \mathbf{u})_z|$ values.

long after the flux has emerged through the photosphere. The sheared energy flux increases by a factor of 4 from the initial emerging phase. The energy evolution resembles that shown in Manchester et al. (2004), with the fundamental difference that active convection ultimately subducts magnetic field and reverses the emerging energy flux.

Figure 2.4 shows the evolution of vertical and horizontal magnetic field structures at the photosphere for Run 3. The horizontal gradients in velocity are illustrated with contour lines of $(\nabla \times \mathbf{u})_z$, i.e. the vertical vorticity. At $t = 10$ min, Panel (a) of Figure 2.4 shows a highly sheared magnetic field structure at this initial phase. Panel (a) of Figure 2.5 shows a horizontal velocity field flowing outward from the center of the granule at $t = 10$ min, when the top of the flux rope reaches the photosphere and the size of the convective granule lying above it increases. After that, the emerging motion is saturated, and the fragmentations and distortions of the magnetic field

mainly result from shearing and convective motions. In Panel (b) of Figure 2.5, the two polarities start to move along the PIL in opposite directions, and form a strong magnetic gradient shown in Panel (c) and (d). At time $t = 15$ min, Panel (b) of Figure 2.4 shows a good coincidence of the PIL and regions with $|(\nabla \times \mathbf{u})_z|$ greater than 1.5 times of the average value. This implies a high velocity shearing along the PIL at the photosphere in the later phase of emergence, which is clearly seen in the region outlined by the green box in Panel (d) of Figure 2.5.

Figure 2.6 shows the evolution of the horizontal velocity, u_x, and the magnetic field lines on the $X = 0$ plane for Run 3. A coherent shearing pattern with velocity u_x up to 20 km/s develops in the lower corona and extends down to the chromosphere and photosphere during the rising of the rope. The shear pattern is similar to Manchester et al. (2004) with notable exceptions of being more highly structured with reduced velocity. We also find that shear flows in the corona persist even when the convective motion washes out any coherent shearing at the photosphere.

2.2.3 U-loop Structure

Here, we examine a U-loop - a magnetic feature formed when magnetic flux is pulled down into an intergranular lane, as reported by Tortosa-Andreu & Moreno-Insertis (2009b). We evaluate the role of Lorentz force $\mathbf{F}$ in a subregion outlined in Panel (c) of Figure 2.5 where the U-loop forms, by examining F_y and the y component of velocity perpendicular to the magnetic field $(u_\perp)_y$. This velocity component, $(u_\perp)_y$, excludes siphon flows parallel to the magnetic field and thus illustrates the motion of magnetic field lines. In Figure 2.7, we show that the field lines on the $X - Z$ plane evolve to a U-loop structure with a shearing velocity $(u_\perp)_y$ up to $\pm$ 1.5 km/s on each side of the PIL (outlined by the green boxes). The upper two panels illustrate the magnitude of the Lorentz force while the bottom panels show the magnitude of $(u_\perp)_y$. The fact that F_y and $(u_\perp)_y$ are in the same direction-reversing across the

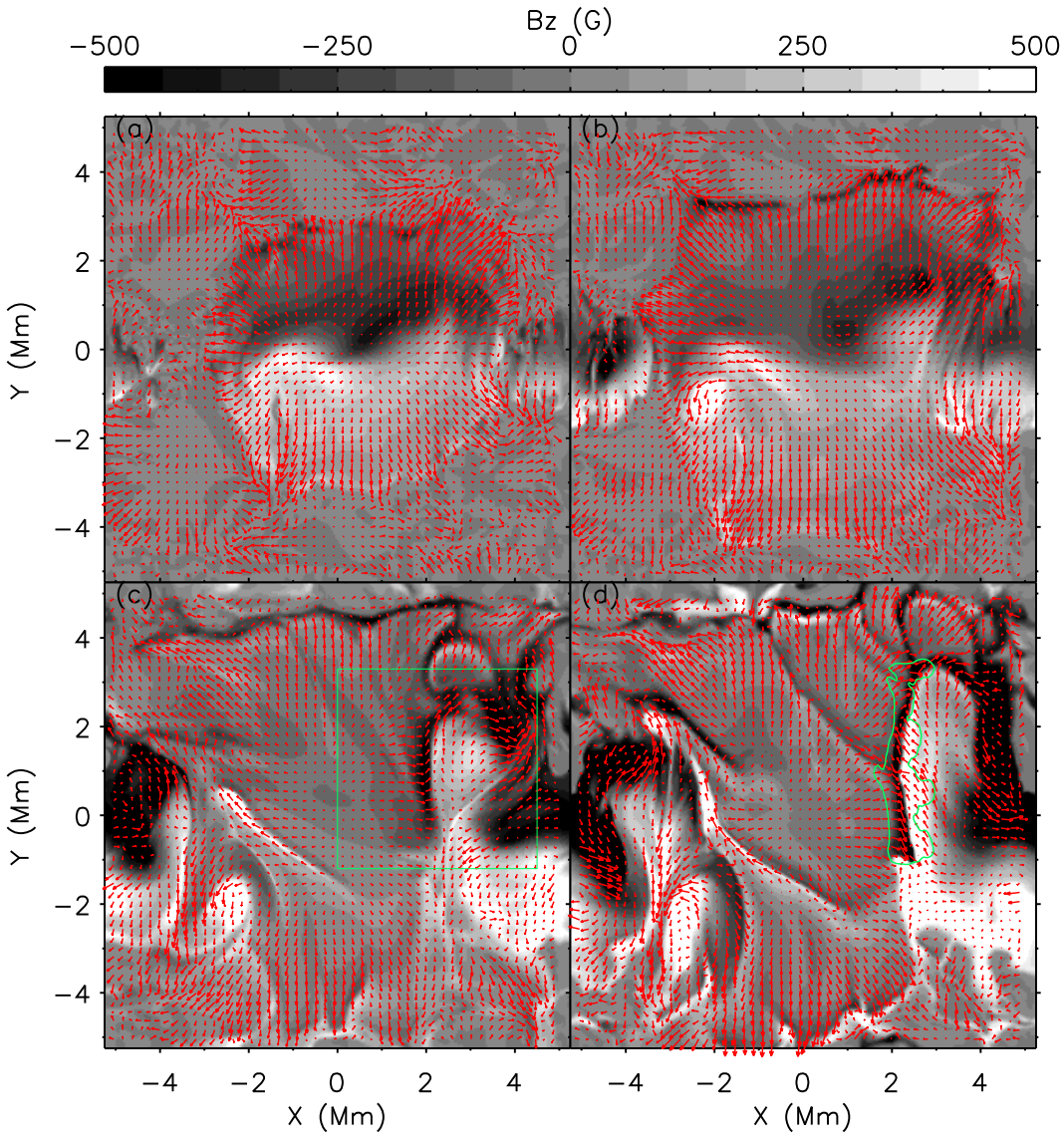

Figure 2.5: The vertical magnetic field structure on photosphere at times $t = 10$ (a), 12 (b), 15 (c) and 20 (d) min for Run 3. The red arrows show the horizontal velocity field. In panel (d), the green line outlines the region with velocity shearing illustrated by $|(\nabla \times \mathbf{u})_z|$ greater than the average value. In panel (c), the green box marks the subregion shown in Figure 2.7 and Figure 2.9. High velocity shearing occurs along the PILs during the emergence.

neutral line (outlined by the green boxes) suggests the velocity shearing is due to the Lorentz force. Panels (c) and (d) of Figure 2.5 show a highly sheared magnetic field and velocity field in this region on the photosphere. However, when viewed from

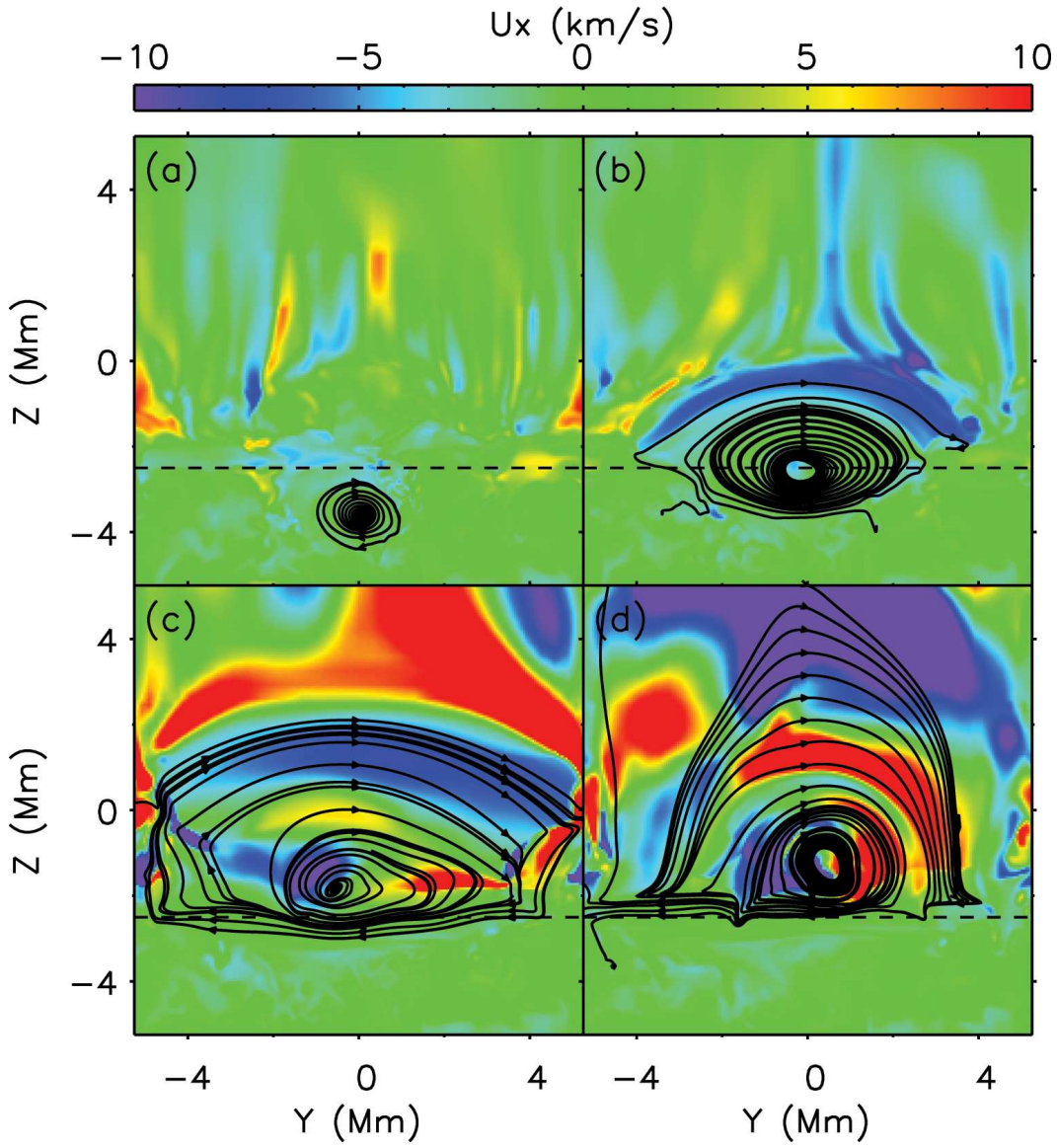

Figure 2.6: Variation of u_x on $X = 0$ plane at times $t = 5$ (a), 10 (b), 15 (c) and 20 (d) min for Run 3. Black lines show the magnetic field lines on the Y-Z plane by ignoring B_x, with arrows indicating the direction. Dashed lines indicate the height of the photosphere. Coherent shearing pattern develops in the lower corona and extends down to the chromosphere when the rope rises.

the bottom, as shown in Figure 2.9 (with 3-D magnetic lines over a gray-scale image of the photospheric B_z field in this region), the magnetic field lines are unsheared below the surface, running perpendicularly to the PIL, and minimizing the energy. Figure 2.8 shows the ratio of the thermal pressure and kinetic energy to the magnetic

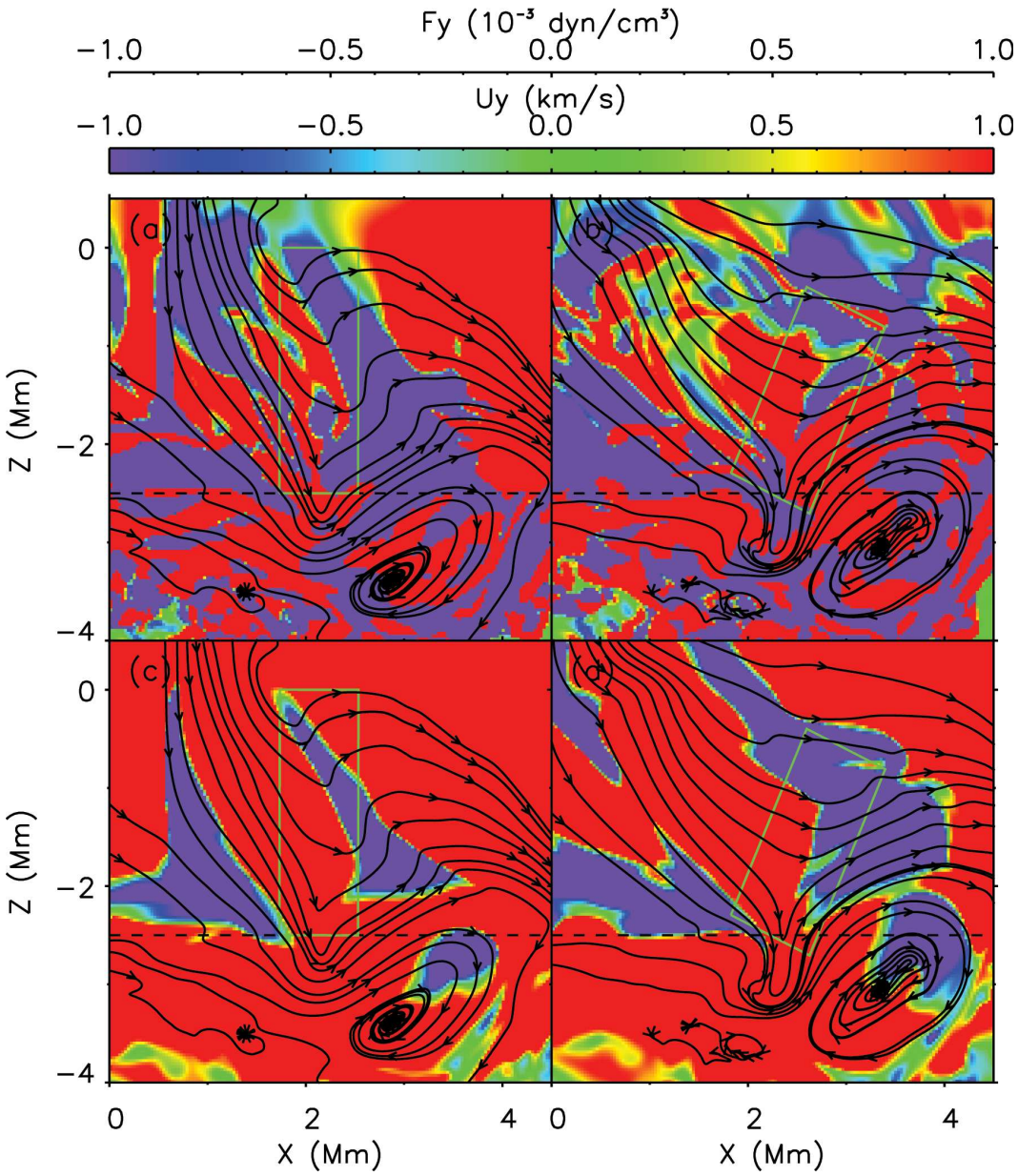

Figure 2.7: (a) F_y structure at time $t = 16$ min (b) F_y structure at time $t = 18$ min (c) y component of velocity perpendicular to magnetic fields at time $t = 16$ min (d) y component of velocity perpendicular to magnetic fields at time $t = 18$ min in the region marked by the green box in Panel (c) of Figure 2.5 for Run 3. Black lines show the magnetic field lines on the plane, with arrows indicating the direction. Dashed lines show the height of the photosphere. The field lines form a U-loop structure with a shearing velocity up to $\pm$ 1.5 km/s on each side of the PIL (outlined by the green boxes).

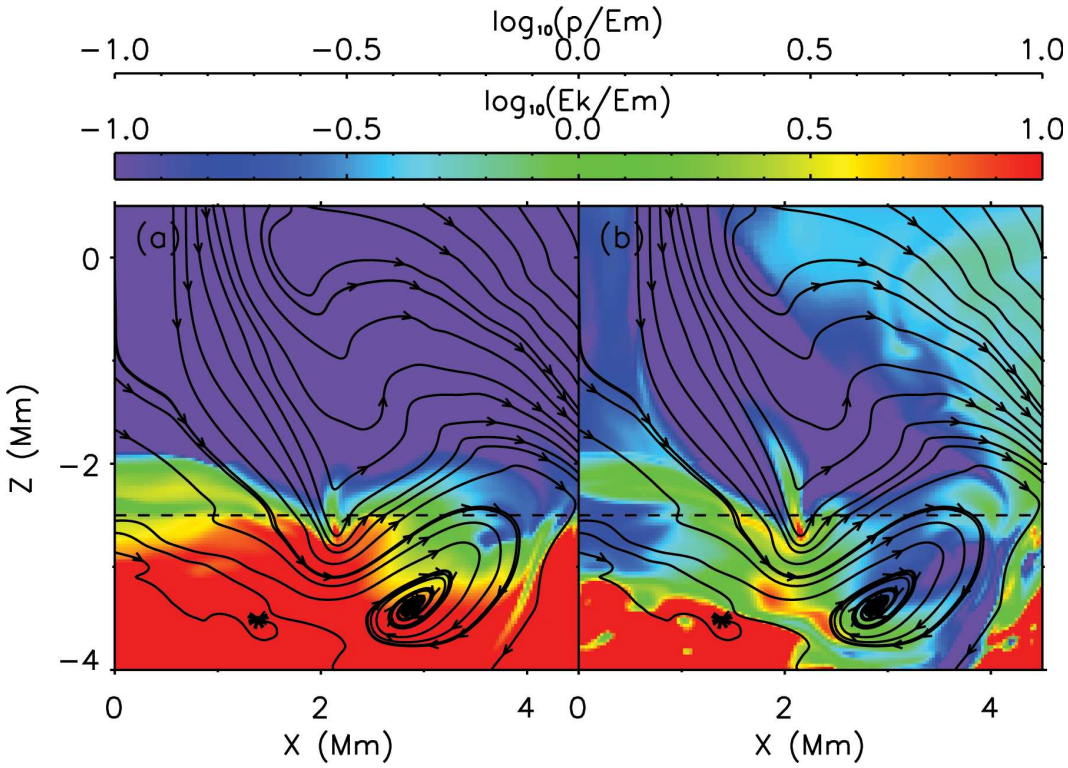

Figure 2.8: (a) Ratio of thermal pressure to magnetic energy $log_{10}(p/E_{mag})$ at time $t = 16$ min (b) ratio of kinetic energy to magnetic energy $log_{10}(E_k/E_{mag})$ at time $t = 16$ min. Black lines show the magnetic field lines on the plane, with arrows indicating the direction. Dashed lines show the height of the photosphere. Kinetic and thermal energy dominate in the domain below the photosphere, while above it magnetic energy dominates.

energy in the region in Figure 2.7. Below the photosphere, kinetic and thermal energy dominate, while above the photosphere, convective motion stops and gives way to the magnetic energy.

It has been commonly observed that the central regions of Ω-loops become highly sheared as they emerge and unshear as they submerge (Manchester, 2007). We find, for the first time, that magnetic U-loops will unshear by flows driven by the Lorentz force, as illustrated by the gradient in B_y. These flows transport energy and axial flux from the convection zone to the corona, where the U-loop is expanding. This simulation further illustrates the dynamic coupling of the convection zone and corona, due to shearing flows driven by Lorentz force, suggested by Manchester (2007). This

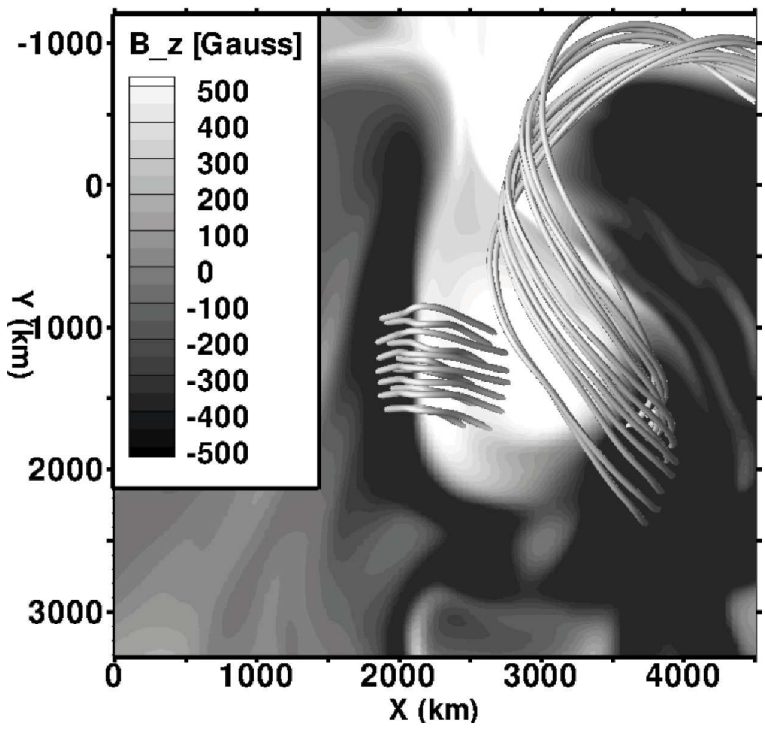

Figure 2.9: Bottom view of the magnetic field lines in region marked in green box in Panel (c) of Figure 2.5 for Run 3. Plane shows the B_z structure on photosphere. The magnetic field lines run perpendicularly to the PIL, minimizing the energy.

coupling occurs for two reasons: the transport of axial flux, and the requirement that axial field strength be equilibrated along field lines to achieve a state of force balance.

2.3 Discussion and Conclusions

Observations have shown that CMEs originate from polarity inversion lines on the photosphere, where strong magnetic and velocity shearing occurs. Study of vector magnetograms of active regions (Falconer, 2001; Falconer et al., 2006) found the nonpotentiality of the magnetic fields, i.e. the total free magnetic energy, to control the CME generation. Other observations also indicate that solar eruptive events, e.g. flares, filaments, and prominences, preferentially occur in magnetic structures where the magnetic field runs parallel to the magnetic inversion line, i.e. highly sheared

magnetic structures (Foukal, 1971; Leroy, 1989; Canfield et al., 1999; Liu et al., 2005; Su et al., 2007). Deng et al. (2006) observed persistent and long-lived (> 5 hrs) shear flows in Active Region NOAA 10486 along the neutral line prior to the occurrence of the X10 flare on 2003 October 29, which may be explained by the successive emergence of a much larger and stronger flux rope/system than that in our simulations.

Surface plasma flows have long been recognized to have an important influence on the evolution of coronal magnetic fields. Many simulations, e.g. Mikic et al. (1988) and van der Holst et al. (2007), have been performed with flux ropes and arcades whose footpoints are subjected to surface motions imposed as boundary conditions. For example, Amari et al. (2003) has shown that converging motions toward the magnetic inversion line can drive a catastrophic nonequilibrium transition into eruptions when accompanied by shearing motions along an inversion line. In Antiochos et al. (1999), sheared arcades reconnect with a surrounding flux system, resulting in an eruption, in which the magnetic free energy stored in the closed shear arcade is released. In these coronal models, shear flows are only prescribed as boundary conditions to trigger instabilities and eruptions. Other numerical simulations (Manchester, 2003; Manchester et al., 2004) have shown shear flows develop self-consistently during the emergence of the flux system (arcade and rope respectively) through a stratified atmosphere. The shearing motions result from the Lorentz force that occurs as the magnetic field expands into the stratified ambient atmosphere. This shearing mechanism explains the following: (1) coincidence of magnetic and velocity inversion lines; (2) the time evolution and magnitude of the shear flows in different layers of the atmosphere; (3) the large scale shear pattern, which is most concentrated at the PIL; (4) transport of flux and energy from the convection zone to the corona; (5) loss of equilibrium when the shear flows are unable to equilibrate the axial flux along magnetic field lines - a process that can explain many observed occurances of CMEs, eruptive filaments, and flares (Manchester, 2003, 2007, 2008; Archontis & Török, 2008;

MacTaggart & Hood, 2009). However, in these idealized models without convective motion, shear flows grow rapidly in the absence of a competing mechanism. In addition, the use of a purely adiabatic energy equation leads to expanding flux ropes whose plasma cools far too rapidly, thus inhibiting the emergence process.

In light of these problems, we incorporated additional physics into our MHD models, and simulated the buoyant rise of a twisted flux rope as it emerged through a turbulent near-surface part of the convection zone into a model corona. Flux ropes with more twist or greater magnetic strength can rise through the convection zone coherently, while less twisted or weaker flux ropes tend to expand in the horizontal direction, while being distorted by the turbulent motions, as shown by Figure 2.2. During its emergence, shearing motions at the photosphere develop and extend into the lower corona, with a speed up to 20 km/s, which is comparable with the shearing velocity of 20 km/s reported by Chae et al. (2000) in active region loops. In our simulations, shearing motion couples the emerged flux with the subsurface magnetic fields, and transfers the energy from below the surface into the solar atmosphere. In Run 3, where the twisting factor $q = -1.5$ and magnetic strength $B_0 = 14.0$ G, the total sheared energy can go up to 1.08×10^{30} ergs in 21 min, about 1% of the average amount released in CMEs. The consistency between our results and previous simulations (Manchester et al., 2004) shows that the physical mechanism of Lorentz force-driven shear flows is very robust during the flux emergence in a domain comparable to ephemeral regions, regardless of the presence of thermodynamic processes such as turbulent convection. Given that active regions are 10 times (with 100 times the area) larger than this simulated flux concentration, our results suggest that shear flows driven by the Lorentz force can readily provide the free magnetic energy for CMEs.

CHAPTER III

Formation of a Solar Active Region

Active regions and sunspots are the most spectacular and strongest magnetic features observed on the solar surface. Hale's polarity law and Joy's law of tilts suggests that active region magnetic fields take the form of Ω-shaped loops of magnetic flux anchored to a strong, toroidal layer of flux at the tachocline. Over the past decade, theoretical investigations and numerical modeling seem to have validated this simple picture (see e.g., the review by Fan 2009b and references therein). While the physics of flux emergence through the deep interior is well-studied (see e.g. Fan et al. 1993; Caligari et al. 1995; Abbett et al. 2000; Fan 2008), the physics of how these magnetic structures emerge through the upper convection zone, forming active regions and sunspots at the visible surface, and expand into the Sun's atmosphere is not yet well understood. It is therefore of great interest to study the interaction of the emerging magnetic features and convective motions of different scales. In Chapter II, we discussed flux emergence within the upper 3 Mm of the convection zone, the very near-surface layer, and the formation of an ephemeral region. We find that the transport of energy into the corona becomes even more critical as downdrafts return much of the magnetic energy back below the photosphere. This simulation results in the emergence of a weak axial flux of 3.3×10^{19} Mx, which is quickly shredded and dispersed to the intergranular lanes by the convection motions. However, active

regions and sunspots exhibit a much larger spatial scale and longer lifetime, which imposes more difficulty in simulating the evolution of the active regions. Moreover, the thermodynamic processes vary drastically from the convection zone to the corona, adding more complexity to large-scale simulations.

Recently, computing power has reached a level that has allowed the development of realistic solar models, including radiative and thermodynamic processes necessary to simulate convection in conjunction with the upper atmosphere. Stein & Nordlund (2006),Abbett (2007),Rempel et al. (2009), Cheung et al. (2010), Kitiashvili et al. (2010), and Rempel (2011) emphasize the importance of the interaction between magnetic fields and convective motions. Stein & Nordlund (2006) and Abbett (2007), have each addressed quiet-Sun magneto-convection, while Kitiashvili et al. (2010) report the critical role of strong vortical downdrafts around small magnetic structures in the formation of large-scale structures. Radiative MHD simulations (see Section 1.3.2) on a larger scale (Rempel et al., 2009; Cheung et al., 2010) have been carried out to study the gradual formation and the fine structures of the sunspots and active regions from the upper convection zone to the surface. Rempel et al. (2009); Rempel (2011) find outflows in the penumbral structure driven by the Lorentz forces at the surface and by the convective flows in the deeper layers. Cheung et al. (2010) simulates the formation of a pair of sunspots in an active region with a magnetic semi-torus advected through the bottom of the domain and finds the mass removal in the magnetic flux driven by the reconnection, and the migration of the flux due to horizontal flows.

These radiative MHD simulations illustrate the importance of turbulent convective flows in the emergence of the sunspots and active regions at the photosphere. The question, then, is how the transport of the energetic and magnetic flux interacts with the plasma motions, through the upper convection zone into the corona. In light of these previous results, we expand upon the work of Chapter II by simulating

the emergence of a larger twisted magnetic flux rope emerging from deeper in the convection zone, and study the energetics during its rise through the turbulent plasma to reside in the hot corona (Fang et al., 2012b). The study here, by covering the upper 20 Mm of the convection zone and the corona, links the solar interior magnetism and the coronal activity by the emergence of the magnetic fields. With this work, we strive to more deeply understand the energetic coupling between the convection zone and the corona provided by the magnetic field.

3.1 Simulation Setups

For our simulation, the MHD equations are solved with BATS-R-US with additional energy sources, as described in Section 2.1. Thermodynamic processes in the solar atmosphere, i.e. surface cooling at the photosphere, radiative cooling of the corona and magnetic flux-related heating in the corona are implemented in the model. The application of a tabular, non-ideal equation of state takes account of the ionization and the excitation of particles in the dense and hot solar interior (Rogers, 2000). Horizontal boundary conditions are periodic, and the lower boundary condition sets the density and temperature of the same values found in the initial state of the atmosphere, while keeping the vertical momentum reflective across the boundary. The upper boundary is closed.

3.1.1 Background Atmosphere

To develop the coronal model, we first extract the averaged state of the solar atmosphere from the model of Chapter II, at a depth of 2.5 Mm below the photosphere. In the convection zone, the plasma is adiabatic as the heating source is absent and radiative cooling is negligible in the optically thick medium. The entropy is therefore nearly invariant throughout the deep convection zone. Here the deep convection zone is defined as deep in the simulation domain, which covers the upper 10% (20 Mm)

depth of the solar convection zone. Under the assumption that the plasma is both isentropic and in hydrodynamic equilibrium, we solve the following equations for the structure of the atmosphere in the deep convection zone with the extracted values providing the upper boundary condition:

$$\nabla p = \rho \mathbf{g}, \tag{3.1}$$

$$log(\frac{p}{\rho^{\gamma}}) = S. \tag{3.2}$$

Here p, ρ and $\mathbf{g}$ are the plasma pressure, mass density and gravitational acceleration. S is the average entropy value in the convection zone at $z = -2.5$ Mm. γ is the adiabatic index, which can be obtained from the tabular equation of state using the pressure and density values, p and ρ. For the purpose of our simulation here, the atmosphere is extended to 21 Mm below the photosphere by solving Equations 3.1 and 3.2. The stratification of the density and pressure of the extended atmosphere in the convection zone are found to be in agreement with that of Stein et al. (2011).

This solution is then used as an initial condition for a one-dimensional calculation in which we apply the surface cooling. The plasma in the simulation domain then goes through an hour of thermal relaxation to form a superadiabatic background atmosphere, which is unstable to convective motion. The next step is to perform the full 3-D simulation with the size of the domain set to $30 \times 30 \times 42$ Mm^3, extending 21 Mm below the surface and 21 Mm above in the vertical directions, while the horizontal area of the domain is comparable to the size of a small active region. In the supraadiabatically stratified atmosphere, convective motion starts immediately after a small energy perturbation, and relaxes over a period of roughly one turnover time of the convection extending to a depth of 21 Mm. After the convective motion has relaxed, we impose an initial vertical magnetic field B_z of 1 G to the domain, and turn on the heating and radiative cooling term in the coronal region. With

the magnetic-flux-related coronal heating term (Pevtsov et al., 2003), the coronal temperature is heated up to 1×10^6 K within 2 hours.

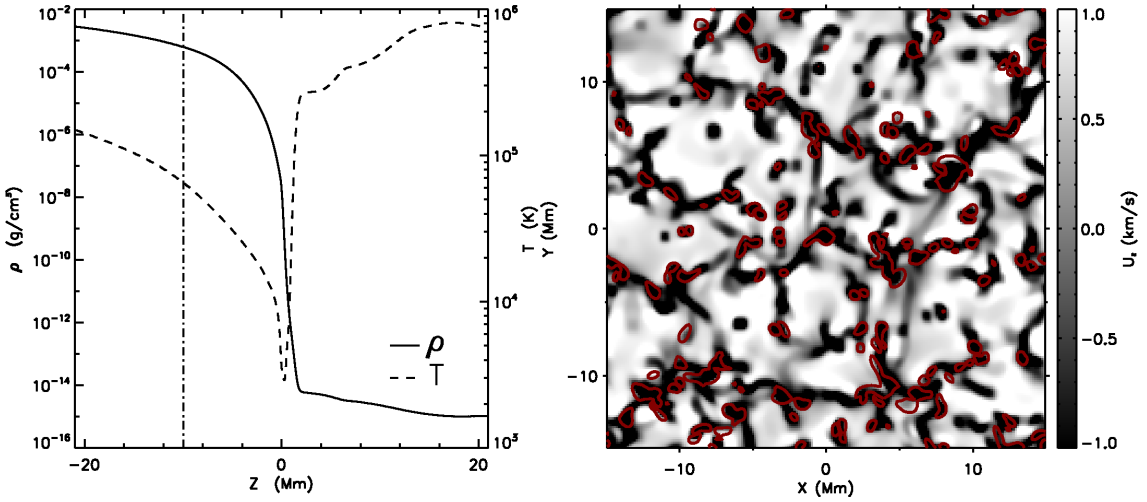

Figure 3.1: Left: The vertical stratification of the density (solid) and the temperature (dashed) of the solar atmosphere. The dash-dotted line indicates the initial location of the inserted flux rope. Right: The vertical velocity structure at $z = -3$ Mm. Red lines show regions with $|B_z|$ greater than 10 G.

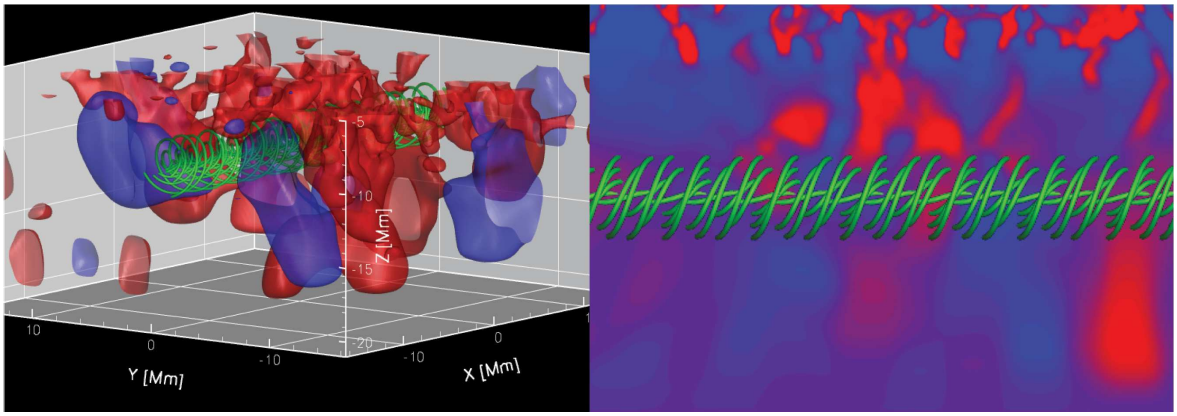

Figure 3.2: The initial structure of magnetic flux rope with color showing the vertical velocity in the convection zone. Left: magnetic flux rope embedded in the convective flows with blue isosurfaces indicating upflows at 1 km s^{-1} and red downflows at -1 km s^{-1}. Right: $x - z$ plane of the convection zone with the inserted flux rope.

The left panel in Figure 3.1 shows the averaged vertical stratification of the den-

sity and temperature in the simulation domain. The density drops by about 5 orders of magnitude from the bottom of the domain to the photosphere, and the temperature drops by 2 orders of magnitude. Above the photosphere, the density drops by another 7 orders of magnitude, and the temperature increases to 1 MK within 2 Mm. The application of the Adaptive Mesh Refinement in BATSRUS greatly facilitates the simulation in saving computational resources while keeping the necessary refinements to resolve the sharp gradient in density and temperature. The grid size in our simulations has three levels of refinement with cubic cells of size 37.5 km, 75 km, and 150 km. The grid is refined in horizontal layers with higher resolution near the surface where temperature and density gradients are largest.

The right panel in Figure 3.1 shows the variation of the vertical velocity u_z at $z = -3$ Mm. Red lines outline the regions with concentrations of B_z field, which coincides well with the down-flowing area. The right panel in Figure 3.2 illustrates the structure of u_z on a vertical cut of the convection zone. Small-scale down-flowing plasma merges and forms the large-scale persistent downdrafts in the deep convection zone. The large-scale downdrafts are very important in the formation of the bipolar structure during the building up of the active region, discussed in Section 3.2.1.

3.1.2 Initial Flux Rope and Convective Motion

The stratification of the atmosphere in the simulation domain is maintained self-consistently with the implementation of the thermodynamic processes in the model. The superadiabatic stratification provides an unstable background atmosphere for turbulent convective motion. As shown by Cheung et al. (2010), convective motion plays an important role in the formation of the sunspots and active region. However, the role of the turbulent convection in the emergence of the magnetic flux has not been clearly understood yet, particularly at larger scales. The aim of our simulation here is thus to study the transfer of the energy and magnetic flux of the rope during its

rise from the deep convection zone, and its interaction with the surrounding turbulent medium. So after the generation of the convection zone with a hot corona, we linearly superimpose a flux rope upon the ambient magnetic field in the deep convection zone, at $z = -10$ Mm, indicated by the dot-dashed line in the left panel of Figure 3.1. The initial flux rope is centrally buoyant and twisted along the $x-$ axis, as described by Equation 2.1 in Section 2.1.2. For the simulation here, we impose a flux rope with a radius of Gaussian decay of $a = 1$ Mm, a twisting factor $q = -1.5$ and the length of the buoyant section of $\lambda = 6$ Mm. The strength of the magnetic field at the axis of the rope is given by $B_0 = 50$ kG, which gives a minimum plasma beta value of 50. The total axial flux on the cross section of the initial flux rope is 1.5×10^{21} Mx. Figure 3.2 shows the initial flux rope embedded within the convective plasma. The left panel illustrates 3-D isosurfaces of the large scale convective flows around the flux rope in the deep convection zone, while the right panel shows the structure of u_z in the convection zone on the $x - z$ plane with the flux rope. The complexity of the convective flows around the flux rope has a strong influence on the emerging process from the deep convection zone with large-scale downflows.

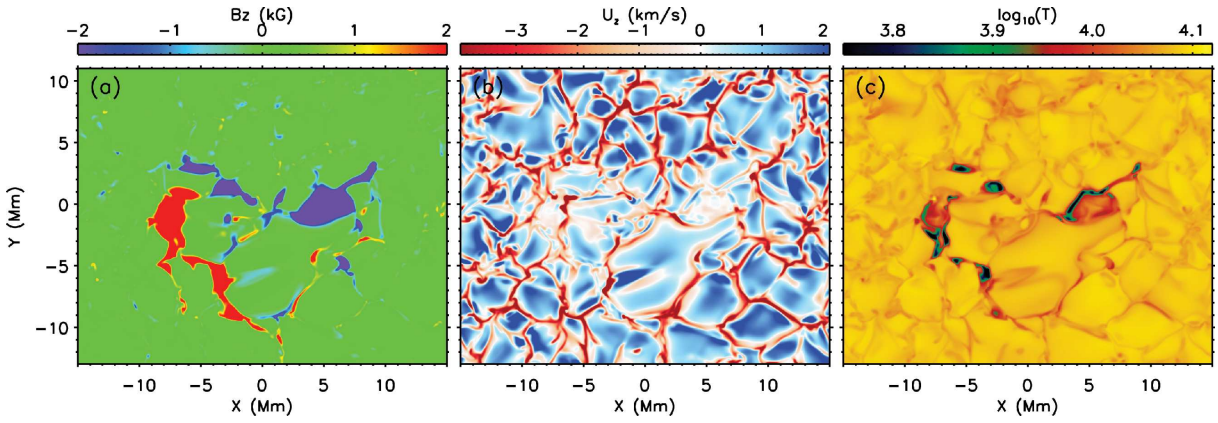

Figure 3.3: The structure of B_z (a), u_z (b) and T (c) at $z = -1$ Mm plane at $t =$ 5:09:00.

3.2 Results

The flux rope is initially embedded in the deep convection zone, where it is buffeted by convective down- and up- flows. On the way from $z = -10$ Mm to the photosphere, the turbulent flows of various scales significantly reshape and redistribute the magnetic flux. On the photosphere, the magnetic flux first emerges as many small-area bipoles, which then sort themselves to form two large concentrations of opposite polarities via coalescence. Figure 3.3 shows the structure of the small active region at $z = -1$ Mm. It contains two pores of opposite magnetic polarities, with smaller-size granules and cooler temperature. The formation of pores by the process of coalescence at the photosphere is revealed by both remote observations and previous numerical simulations (Vrabec, 1974; Zwaan, 1985; Cheung et al., 2010). However, the mechanism that transfers the magnetic flux from the tachocline, which is believed to be the origin of the active region magnetic field, to the solar surface is still to be determined. To date, global scale simulations of the solar interior can not yet resolve individual flux tubes. Here, we examine the evolution of the magnetic flux rope in the deep convection zone and the photospheric and coronal response to its emergence.

3.2.1 Formation of Pores

The horizontal flux rope at $z = -10$ Mm, shown by Figure 3.2, rises in the central section due to the depletion of the density and upwelling convective flows. However, the two ends of the central section are embedded in large-scale downflows present in the convection zone when the flux rope is initiated at $t = 0:00:00$. The downflows are illustrated by the blue isosurfaces and color contours in Figure 3.2. Panel (a) of Figure 3.4 shows the structure of u_z on the $x - z$ plane at $t = 4:50:00$, when the downflows are still present in the convection zone at the two ends of the emerged flux rope. The region of the convective downflows in Panel (a) of Figure 3.4 appears in great accordance with the black and green contour lines indicating the polarity

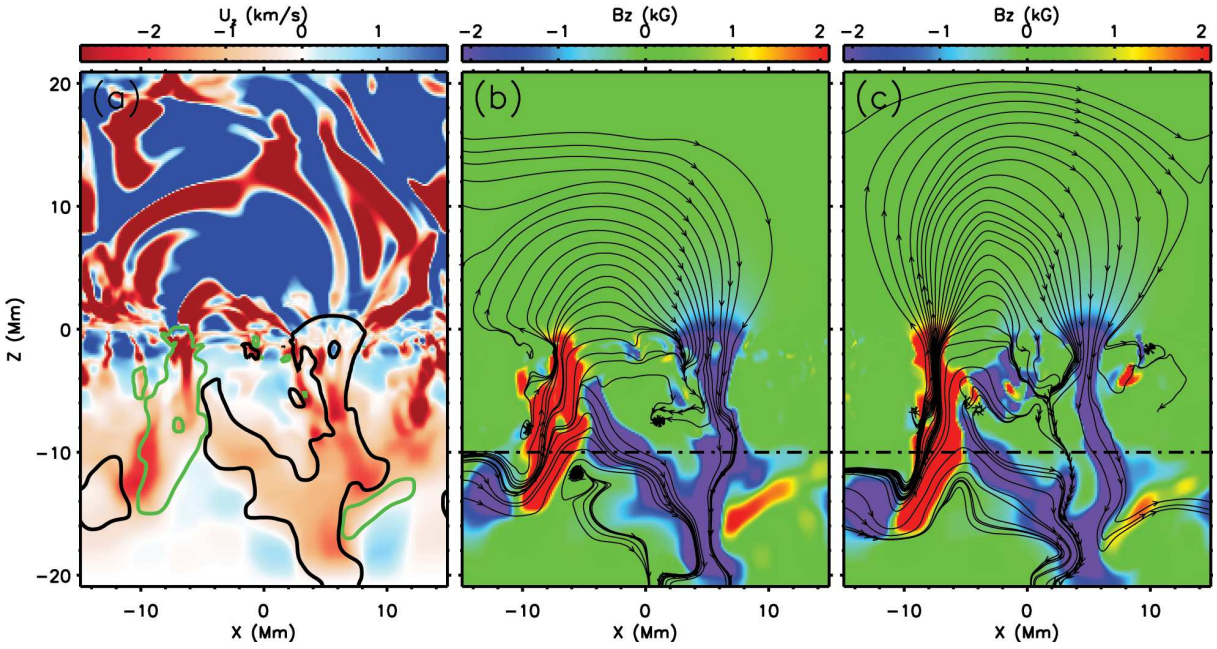

Figure 3.4: The structure of u_z (a), B_z (b) and B_z (c) in the $y = 0$ plane at $t =$ 4:50:00 (a and b) and $t =$ 5:22:00 (c). The black and green lines in Panel (a) outline $B_z =$ -1, 1 kG, respectively. The dash-dotted line in Panel (b) and (c) indicate the initial location of the axis of the inserted flux rope. And the black lines in Panel (b) and (c) indicate the magnetic field lines by ignoring the B_y component to show the direction of the field confined to the $x - z$ plane.

of the pores. This consistency between the downflowing and magnetic concentrated regions suggests a causal relationship between the formation of the magnetic pores and the large-scale downflows. Figure 3.5 illustrates the temporal evolution of the 3-D magnetic field, colored by the u_z value of the local plasma during the rise of the central section of the flux rope. The long-lasting, large-scale downflow, indicated by the blue color, drags down the two endpoints of the rising part and fixes them in the deep convection zone, forming an Ω-shape emerged flux rope within 2.5 hours. The downflow maintains the pores and prevents the two pores of opposite polarities from separation or drifting apart, while the central section of the flux rope emerges and expands in the upper domain. Thus with the two foot points deeply embedded and fixed in the convection zone, the emerged magnetic flux remains highly concentrated

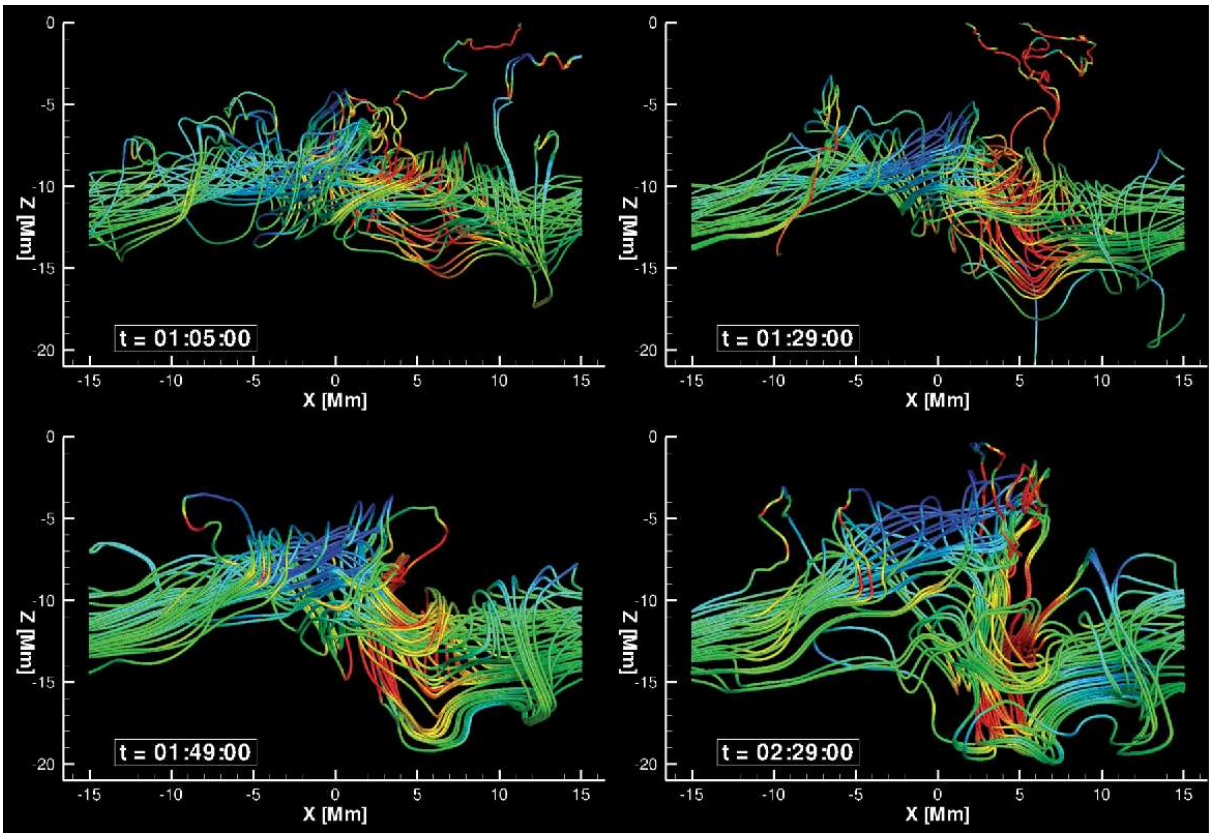

Figure 3.5: The temporal evolution of 3-D magnetic field lines colored by local u_z values with red indicating downflows and blue upflows from -2 km s^{-1} to 1 km s^{-1}, at t = 1:05:00, 1:29:00, 1:49:00 and 2:29:00.

in a relatively small area at the photosphere.

In Panel (b) of Figure 3.3 and Panel (a) of Figure 3.4, small-scale convective granules in the near surface layers appear inside each of the pores. Emonet & Cattaneo (2001) also simulate the diminishing horizontal scale of the granules with increasing vertical magnetic field. While the magnetic field modifies the convective granules, the downward flows produce a bulb of colder plasma. The pressure imbalance with the surrounding material thus causes the flux tube to collapse and increases the strength of the magnetic field (see Section 1.2.2). The flux tube approaches equilibrium again with higher magnetic pressure balancing the surrounding material. With the convective collapse process (Parker, 1978; Spruit, 1979; Nagata et al., 2008), the magnetic

field strength at the surface can be increased up to 4 kG, much higher than the equipartition field strength with the kinetic energy of the surrounding plasma. These near-surface processes, due to the convective motion, play a very important role in reorganizing the magnetic flux after its emergence at the photosphere. The magnetic field of the bipolar structures at the photosphere is intensified by the convective collapse in the near surface layers, which is shown by Panel (c) of Figure 3.4.

3.2.2 Rotation of the Pores

The magnetic flux rope travels through the 10 Mm distance and approaches the photosphere after 2.5 hours. Figure 3.6 shows the evolution of the structure of the B_z field at the photosphere, with arrows representing the horizontal velocity field. The magnetic field concentrates as narrow bands of bipolar fluxes, as shown in Panel (a) and (b), in the regions between the major pores. The horizontal velocity, represented by the white arrows, reveals that the bipoles are moving in opposite directions, toward the major pores of the same polarity. For example, in Panel (a), the rectangle outlines a region with flux emergence, where the negative flux is moving in the upper right direction into the negative pores and the positive flux bands are moving in the lower left direction into the positive pores. The coalescence of the small-scale fluxes into the major pores facilitates the accumulation of the magnetic flux on the surface and, therefore, the formation of the large pores shown in Panel (c) and (d). Cheung et al. (2010) simulated the formation of an active region and finds that the counterstreaming motion of opposite polarities is driven by the Lorentz force.

The large pores of negative polarity show a coherent pattern of rotation at the photosphere after their formation in Panel (a) of Figure 3.6. The rotation of the pores persists during the emergence and the increase of magnetic flux at the photosphere. However, the positive polarity on the left does not present a complete rotation pattern during the emerging phase, but the rotation is interrupted by the horizontal motions

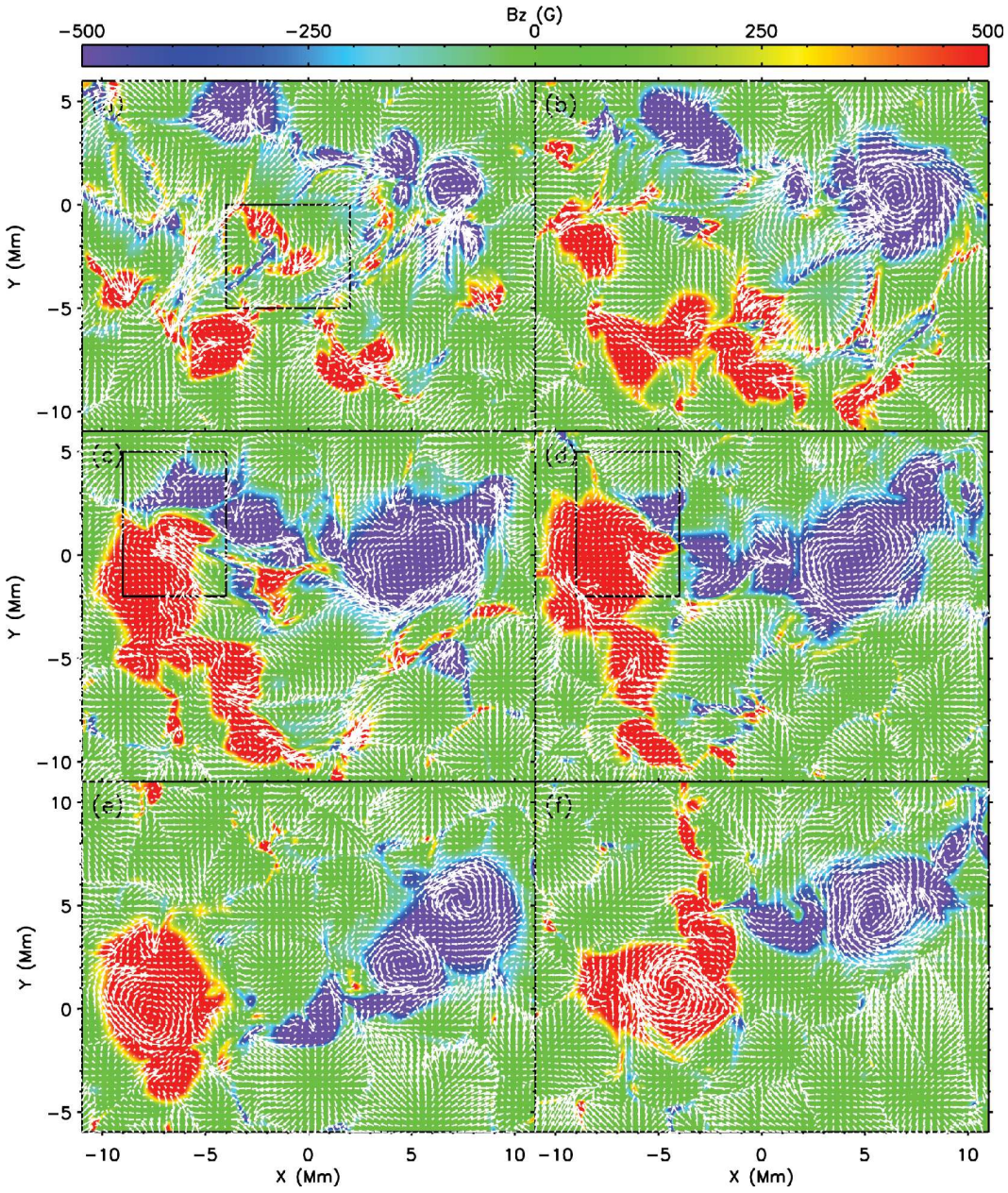

Figure 3.6: The structure of B_z field at $z = 0$ Mm at t = 3:45:00 (a), 4:15:00 (b), 5:10:00 (c), 5:35:00 (d), 6:23:00 (e) and 7:41:00 (f). The arrows show the horizontal velocity field.

of the convective flow. The coherent rotation starts to develop on the positive pore after 5.5 hrs, shown by Panel (e) and (f) in Figure 3.6. Figure 3.7 illustrates the evolution of B_z and the horizontal velocity fields at $z = -3$ Mm, in the convection zone. Here, we observe a coherent rotation at this depth on the negative polarity as

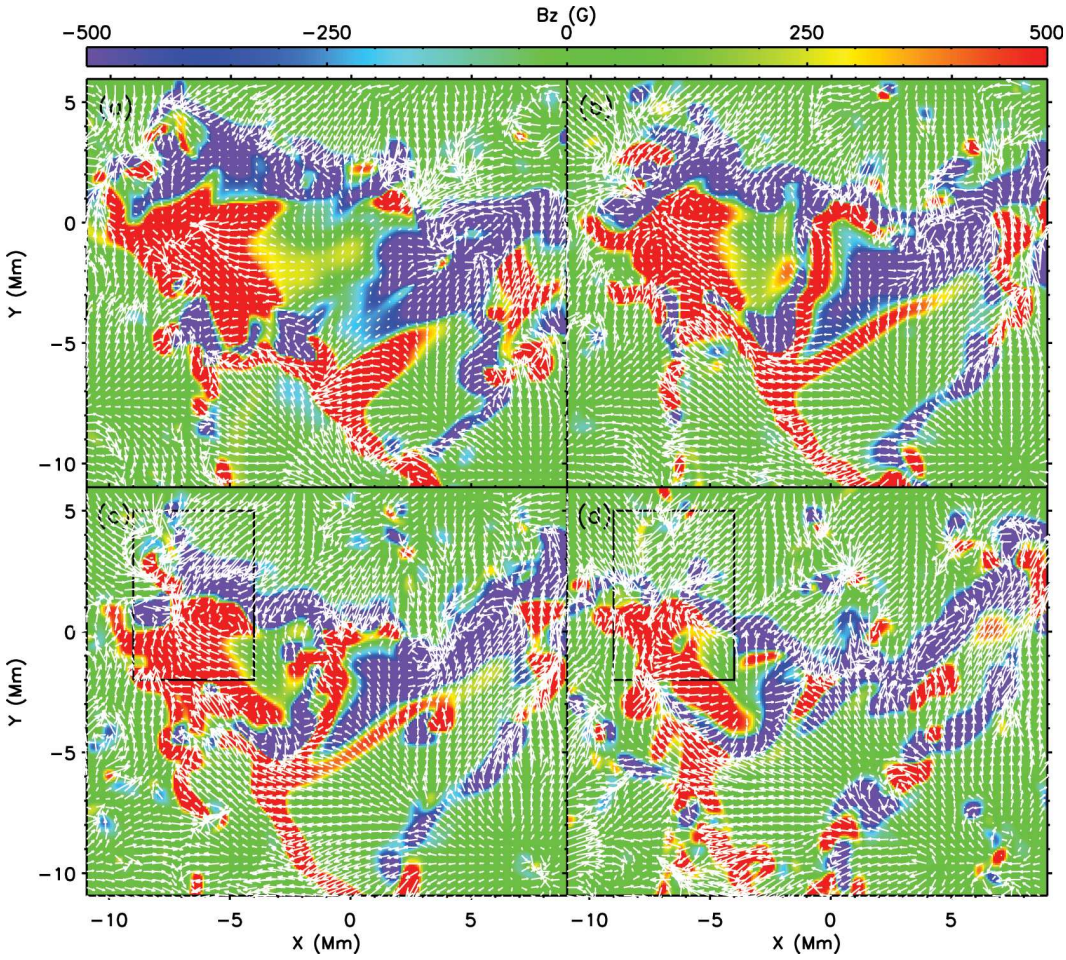

Figure 3.7: The structure of B_z field at $z = -3$ Mm at t = 4:40:00 (a), 5:00:00 (b), 5:10:00 (c), and 5:30:00 (d). The arrows show the horizontal velocity field.

well. The question then, is to what depth does the rotation extend? We therefore examine the structure of u_y on the $y = 0$ plane during the rising of the flux rope in the upper panels in Figure 3.8. The reversal of the direction of u_y in the right side of the domain corresponds to the projection of the rotation of the negative polarity on the $y = 0$ plane. The coherent rotation starts to extend downward at $t = 4 : 00 : 00$ and approaches the depth of -10 Mm in 21 mins. (see Panel (a)). Panel (c) shows a very coherent pattern of rotation on the negative polarity at $t = 5 : 13 : 00$, while on the positive pore on the left, the rotation is not obvious.

Sunspot rotation has long been observed and studied in detail and has been found

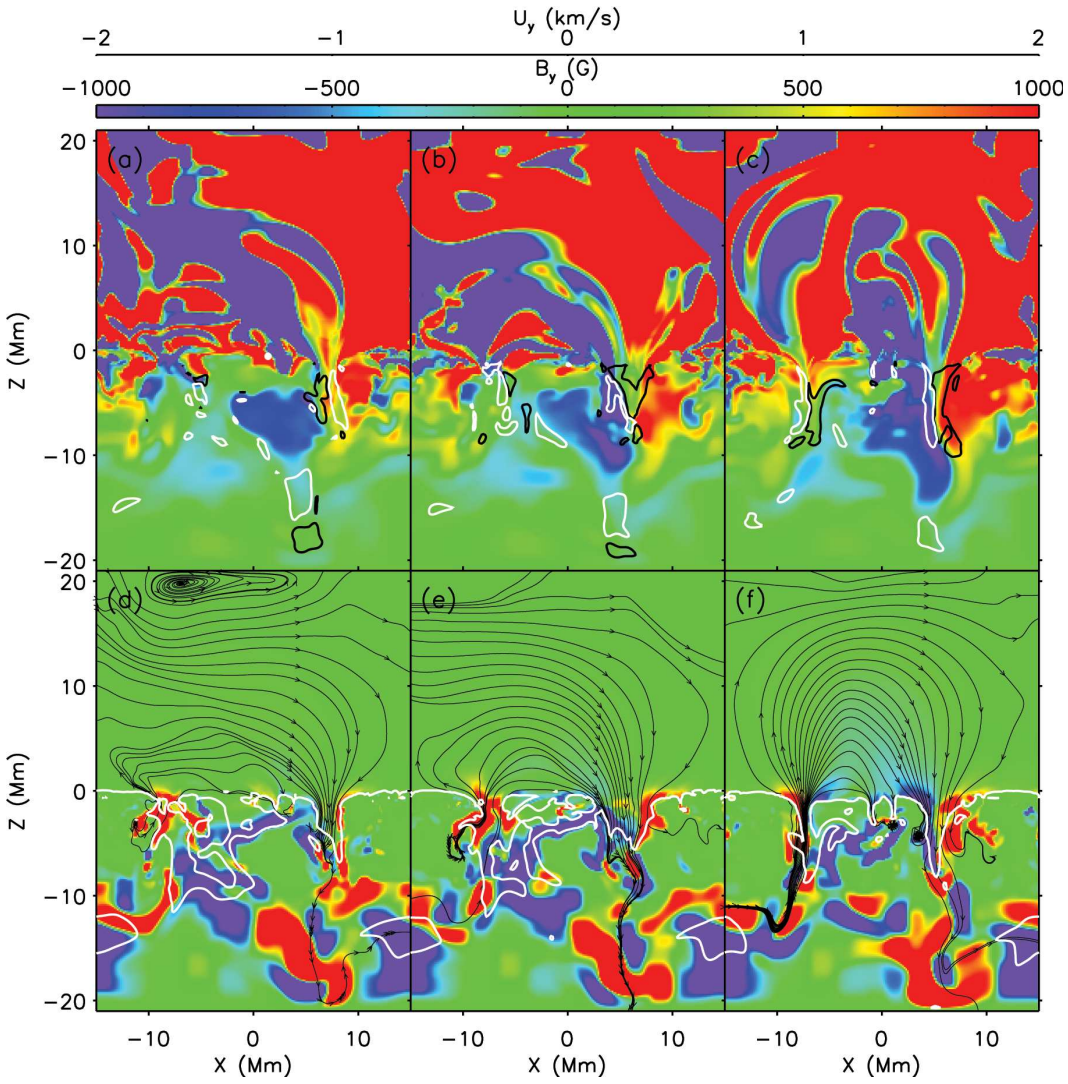

Figure 3.8: The structure of u_y (upper panels) and B_y (lower panels) at time t = 4:21:00 (a and d), 4:37:00 (b end e) and 5:13:00 (c and f) in the $y = 0$ plane. The black and white contour lines in the upper panels represent regions with Lorentz force density f_y = -20 and 20 dyne cm^3 respectively. And the black lines with arrows in the lower panels indicate streamlines of (B_x, B_z) while white lines outline Alfvènic Mach number $u/u_A = 1$.

in association with CMEs (Brown et al., 2003; Kazachenko et al., 2009). The rotation mechanism for sunspots found in our simulation was first described by Parker (1979a). Longcope & Welsch (2000) simulated the increase of the helicity of coronal field due to the rotation of the photospheric footpoints in a dynamic model. Ideal MHD simulations by Fan (2009b) illstrate the rotation driven by torsional Alfvèn

waves and the development of sigmoid-shaped field lines during the flux emergence from the top layer of the convection zone. Brown et al. (2003) and Min & Chae (2009) study the behavior of the rotating sunspots in solar active regions and found that the rotation speed varies with time, radius and angular spacing, with an increase in rotation speed in the penumbra. Kosovichev (1996); Zhao & Kosovichev (2003) find twists of the magnetic field and vortical flows around the sunspots in the convection zone underneath a rapidly rotating sunspot area. The flows underneath the negative pore in our simulation also exhibit a rotating pattern extending 10 Mm down into the convection zone. The question then, is what dynamic mechanism during flux emergence causes the observed variation in the rotation speed? Our simulation enables a detailed investigation of how sunspot rotation develops in the complex circumstances of the convection zone.

The development of the coherent rotation is accompanied by the presence of a strong Lorentz force in the azimuthal direction (see the upper panels in Figure 3.8), which is defined as $f_y = j_z B_x - j_x B_z$. The black and white contour lines in the upper panels of Figure 3.8 represent areas with strong negative and positive f_y respectively. We find that the Lorentz force is driving the coherent rotation as a torsional Alfvèn wave. At time $t = 4:21:00$, shown by Panel (a), the Lorentz force is in the same direction as u_y, thus acting to accelerate the rotation. However, the Lorentz force reverses direction at time $t = 4:37:00$ (see Panel (b)) and decelerates the rotation. Panel (c) reveals the structure of the Lorentz force at time $t = 05:13:00$, which runs in the opposite direction of the rotation. The flux rope has rotated past its equilibrium point, and the Lorentz force reverses with the gradient of the azimuthal (B_y) component of the field as the flux rope further emerges. The rotation of the pores untwists the field in the convection zone and produces a twisted magnetic field in the corona, as shown by the lower panels of Figure 3.8, which illustrates the B_y field on the $y = 0$ plane. As such, the rotation also provides a mechanism to build up

the helicity and magnetic energy in the coronal magnetic field. The white lines in the lower panels outlines where the Alfvénic Mach number $u/u_A = 1$. The consistency between the structures of the Alfvénic Mach number and the Lorentz force f_y suggests that in the pore region the magnetic field dominates over the plasma motion, and is responsible for the rotating flows.

In Figures 3.6 and 3.7, the positive polarity does not present as coherent a rotation as the negative polarity. However, in Panel (c) and (d) of Figure 3.6, we observe a strong flux cancellation in the region outlined by the rectangles from time $t = 5:00:00$ to $t = 5:35:00$. Cheung et al. (2010) reports that magnetic reconnection takes place within the U-loops formed by the convective downflows, which can remove the unsigned magnetic flux on the photosphere. In our simulation, the total amount of the magnetic flux that is cancelled is 10% of the total unsigned flux on the photosphere. The flux cancellation strongly interrupts the coherency of the rotation on the positive polarity. The horizontal velocity fields exhibit a converging flow at the two opposite polarities of the cancelled flux, both at the photosphere and in the convection zone, yielding a high gradient in the magnetic field. A close examination of this flux cancellation event will be the discussed in Chapter IV. Another interesting feature we observe in our simulation is that the horizontal velocity field in Figure 3.7 shows a converging horizontal flow field around the magnetic flux region. This convective converging flow constrains the total area of the magnetic concentration, and thus prevents the magnetic pores from expanding and separating.

3.2.3 Energy Fluxes

The magnetic flux rope approaches the photosphere within 2.5 hours after its initialization, and the photospheric magnetic flux, i.e. the emerged flux, reaches its maximum value at time $t = 5:11:00$. Afterward, the magnetic pores start to decay slowly for the rest of the simulation. However, even at its maximum emergence, the

magnetic flux rope is far from being fully above the photosphere. This is clearly shown by Panel (b) and (c) of Figure 3.4, where the negative polarity is split into two parts, with one part emerging and forming pores while the other is sinking to the deep convection zone. The lower right panel of Figure 3.5 shows the 3-D magnetic field lines of the flux rope when it first approaches the photosphere. The red contour color over the field lines represents upflows while blue represents downflows. Only about half of the original flux rope is rising with upflows, while the other half remains almost stationary or sinks in the convection zone.

It is of great interest to study the mechanism for transporting the initial magnetic flux from the deep convection zone into the photosphere, where the magnetic pores appear, and further out into the corona. Here we calculate the temporal evolution of the total unsigned magnetic flux at the photosphere ($z = 0$), $z = -3$ Mm and $z = 3$ Mm, shown by the upper panel of Figure 3.9. At time $t = 4 : 49 : 00$, the magnetic flux at $z = -3$ Mm reaches its maximum value of 2.63×10^{21} Mx, which is most of the total unsigned flux (3.04×10^{21} Mx) when the flux rope is initially bent.

At the photosphere, at $t = 5 : 11 : 00$, the unsigned magnetic flux reaches its maximum of 1.37×10^{21} Mx, 45% of the total initial flux. The unsigned flux at $z = 3$ Mm in the lower corona maximizes at $t = 05 : 29 : 00$ with a value of 8.00×10^{20} Mx. The ratio of the emerged unsigned flux with respect to the total initial flux decreases with increasing altitudes, from 86% at $z = -3$ Mm to 26% at $z = 3$ Mm. The sharp decrease from the convection zone to the photosphere is caused by the downflows in the near-surface layers that tend to return flux to the deep convection zone.

The question then, is how the horizontal and vertical flows (driven both by convective motions and the Lorentz force) affect the emergence of magnetic flux and the transport of the magnetic energy. To address this question we next calculate the magnetic energy flux (Poynting flux) passing through three layers of the atmosphere: $z =$ -3, 0, and 3 Mm using Equation 2.5 and 2.6. The lower panel of Figure 3.9 illustrates

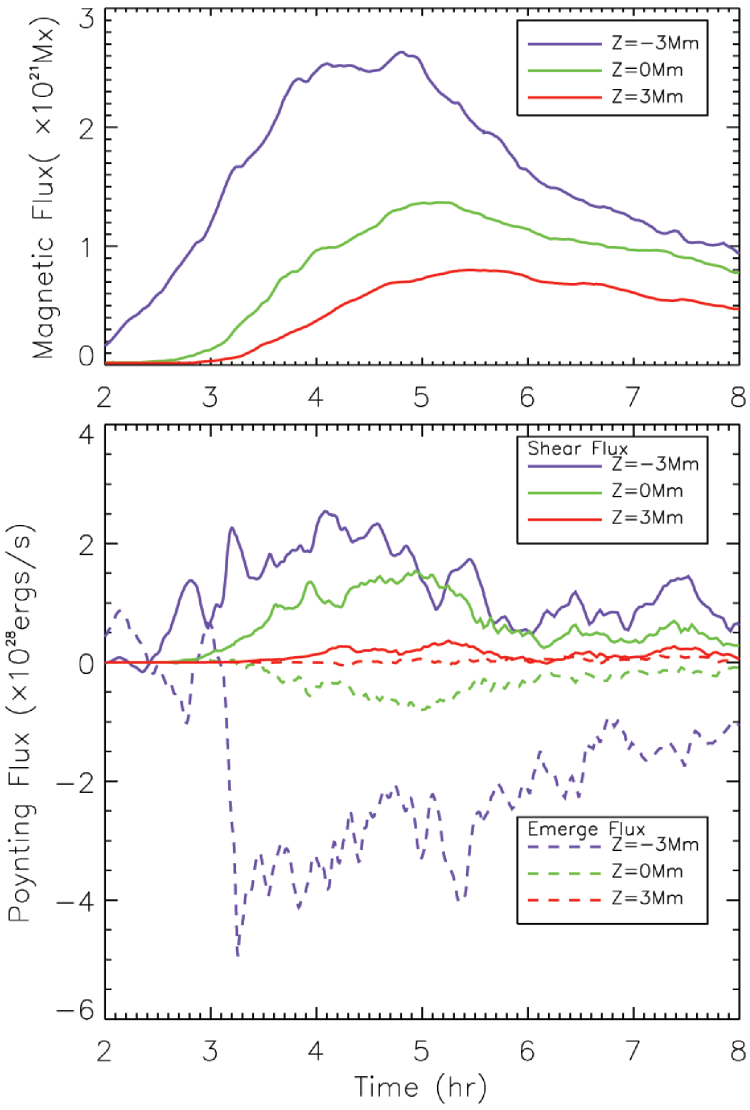

Figure 3.9: The temporal evolution of magnetic flux (upper) and energy flux (lower) associated with the horizontal flows (solid) and vertical flow (dashed) at $z = -3$ (purple), 0 (green) and 3 (red) Mm from time $t = 2:00:00$ to $t = 8:00:00$.

the temporal evolution of the Poynting energy flux associated with the horizontal and vertical motions. We find that the energy flux associated with the vertical flows at z = -3 and 0 Mm, remains negative during the rising and decaying phase of the flux emergence. There are several transient positive pulses of energy fluxes by the vertical

motions at $z = -3$ Mm, at times $t = 2:09:00$ and $t = 2:57:00$. These transient positive pulses represent the energy transport when the magnetic flux first emerges to the surface with upflows, as shown by the lower right panel of Figure 3.5. Each of these pulses is followed by a sharp increase in the energy flux associated with the horizontal flows and a reversal of the energy flux by vertical flows. This time evolution of energy shows a process of magnetic flux emergence at the near surface layers with convective flows: magnetic flux emerges at the surface as bipoles with upflowing motion, then they are quickly pulled apart by the horizontal flows, and concentrate in the downdrafts. This process then leads to a positive energy flux by the upflows, followed by a increasing energy flux by the horizontal motions, and a negative energy flux associated with the downdrafts.

Panel (a) and (b) in Figure 3.10 show the B_z field at z = -3 and 0 Mm, overlaid by white lines showing downdrafts. The concentration of the magnetic flux in the downdrafts explains the negative energy flux associated with the vertical flows in the lower panel from 3.0 hrs to 5.0 hrs while the total magnetic flux is still increasing in the upper panel. During this time period, more than 60% of the total unsigned flux is in the downflowing region for both z = - 3 and 0 Mm layers. At time $t = 5:11:00$, when the photospheric unsigned flux maximizes, 70% of emerged flux is concentrated in the downdrafts. Panel (c) and (d) show the Poynting fluxes at the photosphere associated with the vertical and horizontal flows, defined as:

$$F_{\rm shear} = -\frac{1}{4\pi}\left(B_x u_x + B_y u_y\right) B_z, \tag{3.3}$$

$$F_{\rm emerg} = \frac{1}{4\pi}\left(B_x^2 + B_y^2\right) u_z. \tag{3.4}$$

$F_{\rm emerg}$ is negative in the magnetic polarities while postive in the areas between the polarities , where the magnetic flux is emerging. In the pores, the energy flow is instead dominated by the $F_{\rm shear}$, shown by Panel (d). At $z = 3$ Mm, in the corona, the

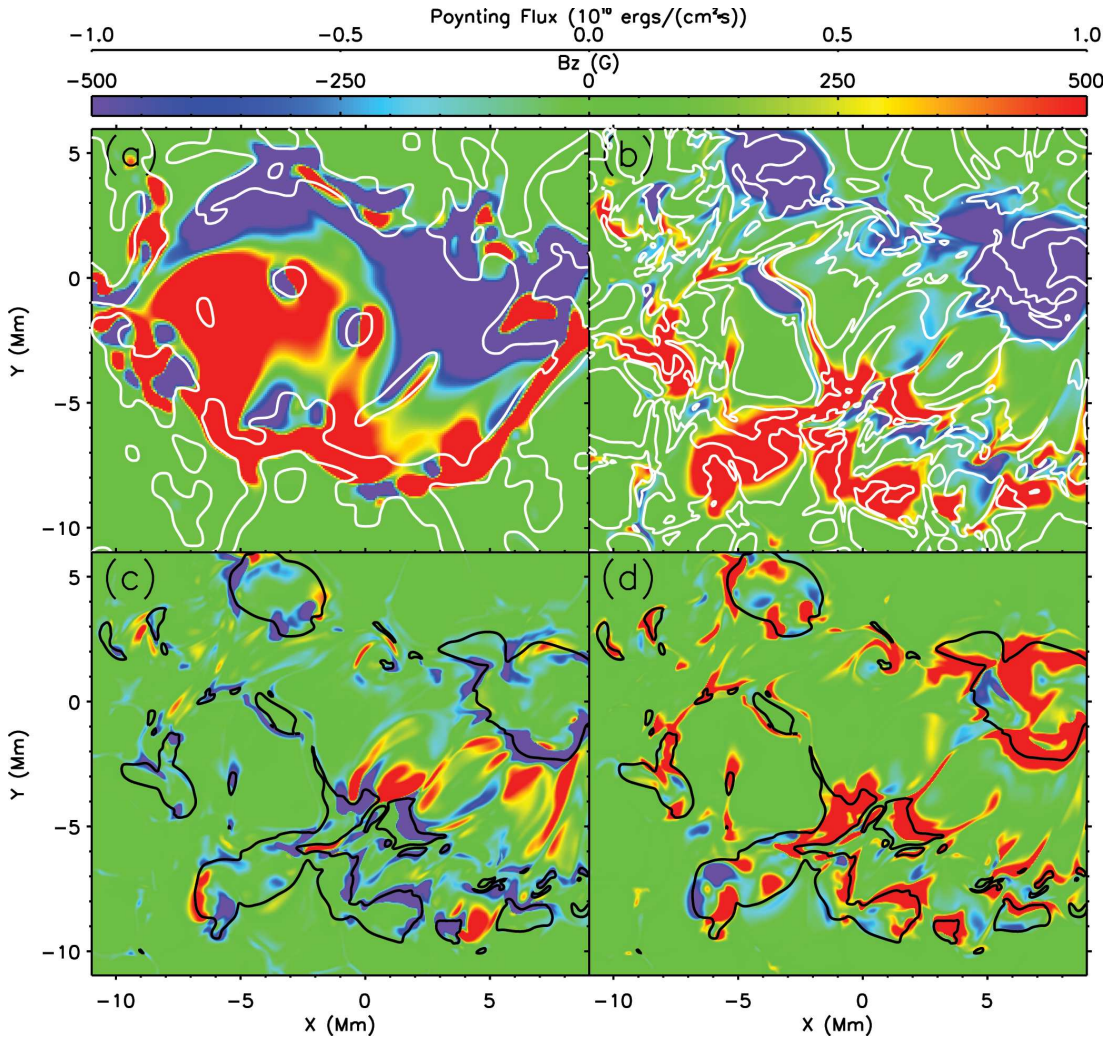

Figure 3.10: The structure of B_z field at $z = -3$ Mm at t = 3:40:00 (a), B_z field at $z = 0$ Mm at t = 4:03:00 (b) and Poynting fluxes associated with vertical (c) and horizontal flows (d) at $z = 0$ Mm at t = 4:03:00. The white lines in Panel (a) and (b) indicate downflowing regions with u_z = -0.1 km s^{-1}, and the black lines in Panel (c) and (d) show regions with $|B_z| = 500$ G.

energy flux by the vertical flows shows short periods of postive values. The increased energy flux is driven upward by convectively-driven magnetoacoustic shocks, and could be interpreted in terms of the dynamics of Type I spicules (see e.g., Hansteen et al. (2006); Martínez-Sykora et al. (2009)).

The Poynting flux associated with the horizontal flows dominates the energy trans-

port during the flux emergence. At the photosphere, the total energy transport by this flux is 1.35×10^{32} ergs, while vertical flows transport 5.77×10^{31} ergs, 42% of the energy back to the convection zone by the end of the simulation. The horizontal flows here include the rotation of the magnetic pores, the separating motion of the small bipoles and the shearing motion along PILs. The rotation of the pores is discussed in Section 3.2.2, which transports both the magnetic energy and helicity into the corona region. The extension of the rotation motion into the deep convection zone shown by Figure 3.8 greatly impacts the spatial distribution of the Poynting flux by the rotation. Figure 3.6 shows the separating process of the small bipoles, which tend to move apart from each other after their emergence at the photosphere and merge into large pores with the same polarity via this self-sorting process. The horizontal separating flow on the small bipoles builds up energy in the near surface region. In Panel (c) and (d) of Figures 3.6 and 3.7, the black rectangles outline the area with a large-scale magnetic flux cancellation. The converging flows across the PIL build up the magnetic gradient in this area, and the shearing flow along the PIL, shown in Panel (c) and (d) of Figure 3.6, drives the magnetic field lines along the PIL and builds up a highly sheared magnetic field configuration, which plays an important role in eruptive events such as flares, filament eruptions and CMEs (Mikic & Linker, 1994; Wu & Guo, 1997; Antiochos et al., 1999).

3.3 Discussion and Conclusions

In Section 3.2.1 and 3.2.2, we examined the structures of the vertical and horizontal velocity fields separately and their influence on the emerging magnetic flux rope. The persistent large-scale downflows help form and maintain the bipolar pores of uniform polarity in the deep convection zone, while the small-scale downflows in the near-surface layers intensify the strength of the emerged flux tube by convective collapse, as suggested by Parker (1978) and found in previous simulations by Stein & Nordlund

(2006). At the photosphere, the horizontal flows act on the small newly-emerged bipoles, to not only separate opposite polarities, but also sort them into large pores of uniform polarity. This coalescence of small-scale fluxes enables the formation of the magnetic pores with a unsigned flux of up to 1.37×10^{21} Mx, which is limited by the scale of our simulation. The horizontal flows of the magnetic pores exhibit a coherent rotation extending down to the deep convection zone, which is clearly driven by the Lorentz force as was found in earlier simulations (Longcope & Welsch, 2000; Fan, 2009b). Our simulation illustrates that this rotation mechanism operates in a realistic convection zone but requires the coalescence of a well formed pore. In addition, complex interactions may break the symmetry of the pore, (such as flux cancellation) and disrupt the rotation.

We calculate the energy transport due to the horizontal and vertical flows in the domain from the convection zone to the corona. Abbett & Fisher (2011) found that, in the quiet Sun, the Poynting flux flows downward into the interior below the visible surface and flows upward into the corona above it. They suggest that surface convection is the energy source of the separatrix in the energy flux. Our study shows a negative total energy flux at $z = -3$ Mm, and positive at $z = 0$ and 3 Mm, which agrees with this result. The energy flux is initially dominated by the emerging flow on the magnetic flux. Shortly thereafter, opposite polarities separate. This gives rise to an increase in the energy flux associated with the horizontal flows. This general trend has been found in early work e.g. Magara & Longcope (2003); Manchester et al. (2004) and Chapter II, but these works did not illustrate the extent to which downflows control energy transport in the convection zone. In the convection zone and at the photosphere, the flux concentrates in the downflow drafts, yielding a negative energy flux associated with the vertical motion. Horizontal flows thus dominate the magnetic energy transport into the corona. We identify three types of horizontal flows in Section 3.2.2: the rotation, the separating motion of the bipoles, and the shearing

motion along PILs. The rotation and shearing both transfer magnetic energy and helicity into the corona. And it is the separating and shearing motions that build up the magnetic energy in the near-surface region, which is necessary if eruptive events are to occur.

In our simulation, we also find an area with cancellation of magnetic flux up to 10^{20} Mx within 0.5 hour, shown by Panels (c) and (d) of Figure 3.6. The coronal response to this large-scale flux cancellation is of great interest. Green et al. (2011) finds the evolution of coronal fields into a highly sheared arcade and then a sigmoid in an active region where 1/3 of the flux is cancelled. Whether the cancelled flux in our simulation produces a flux rope in the coronal region will be examined in Chapter IV. Another interesting feature is the decay of the magnetic pores from time $t = 6:00:00$ to $t = 8:00:00$, shown by Figure 3.9. van Ballegooijen & Mackay (2007) suggests that the submerged magnetic field repairs the toroidal flux ropes from which the initial flux emerged. The decayed magnetic flux thus may play a fundamental role in replacing the magnetic field in the solar interior.

CHAPTER IV

Energy Buildup for Eruptive Events

Regions of intense solar magnetic fields such as sunspots and active regions are known to exhibit energetic outbursts that are manifest in many forms, such as CMEs, filament eruptions, and flares (e.g. Forbes, 2000; Low, 2001; Forbes et al., 2006; Gopalswamy, 2006; Schrijver, 2009). Although less energetic, large-scale regions of relatively weak magnetic fields can also erupt giving rise to streamer blowouts and the expulsion of quiescent filaments into the solar wind (e.g. Hundhausen, 1993; Lynch et al., 2010). As discussed in Section 1.2.3, strong solar eruptions release a significant amount of the free energy, up to 10^{32} ergs. Therefore, in order to produce such eruptions, the magnetic field must possess free magnetic energy, which requires that the field is in a nonpotential configuration with electric currents passing through the photosphere and into the corona. The non-potential coronal fields, before the eruption, are believed to take the form of either sheared arcades or twisted flux ropes, both of which store a significant amount of magnetic free energy (see Section 1.2.3). However, the buildup of the non-potentiality and the destabilization of the coronal field is yet to be determined. The excellent coverage of the eruptive events by observations have provided us a better understanding of the preferred magnetic and dynamic configuration of the system for eruption: the existence of strong PILs is essential for the ocurrence of M- and X- class flares (Schrijver, 2007; Falconer et al., 2008); active

region CME and flare productivity is also strongly correlated with magnetic shear (Hagyard et al., 1984; Falconer et al., 2002, 2006); shearing flows associated with flux emergence also drive enhanced flaring (Schrijver et al., 2005); flux cancellation has been observed to be associated with flares (Martin et al., 1985) and CMEs (Subramanian & Dere, 2001) in active regions; Green et al. (2011) shows a clear example in AR 10977, where reconnection at the PIL during flux cancellation forms a highly sheared arcade and sigmoidal structure during eruption; and Li et al. (2004) found converging flows consistent with flux cancellation in decaying and young active regions producing CMEs.

Inspired by the observations, shear flows, converging motion and flux cancellation have been implemented artificially in MHD simulations to drive solar eruptions. A widely used approach is to apply the shear flows, converging motion or flux cancellation as boundary conditions at the photosphere Steinolfson (1991); Mikic & Linker (1994); Amari et al. (1996); Guo & Wu (1998); Amari et al. (2003). Recent simulations have identified the shear flows naturally arising from the expansion of the magnetic flux into the stratified atmosphere and the energy transport of shear flows naturally provides an energy source for CMEs (Manchester et al., 2004; Manchester, 2007, 2008). The study in Chapter II and III addresses the emergence of magnetic flux ropes from a turbulent convection zone into the corona and found both shear flows and rotational flows driven by the Lorentz force. These horizontal flows were found to dominate the energy transport from the convection zone into the corona. Of particular significance, the simulation in Chapter III exhibits a case of large-scale flux cancellation, a phenomena strongly associated with CME initiation (Subramanian & Dere, 2001). More importantly, the flux cancellation is accompanied by shearing and converging motion around a sharp PIL. Here we examine the flux cancellation in conjunction with energy transport from the convection zone to the corona and enhance our understanding of how these processes are critical for solar eruptions (Fang et al.,

2012a).

4.1 A case of Flux Cancellation

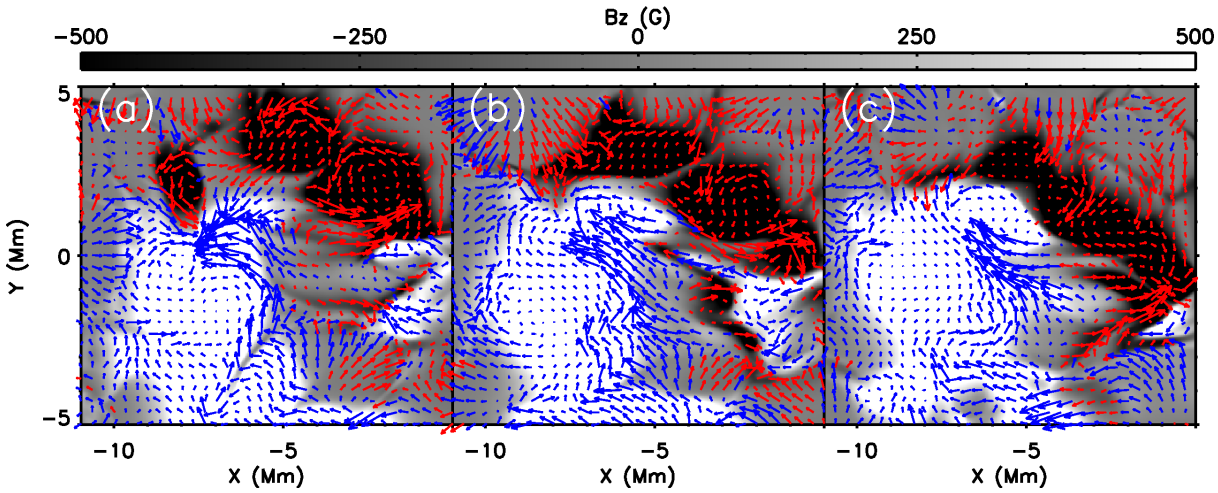

Figure 4.1: The photospheric structure of B_z in the area of flux cancellation at time t = 5:00:00 (a), 5:10:00 (b), 5:22:00 (c). Blue and red arrows show the horizontal velocity in positive and negative magnetic polarities, respectively. Shear flows are most apparent at time t = 5:10:00.

The simulation of Chapter III studies the emergence of a buoyant, initially stationary, horizontal flux rope inserted at $Z = -10$ Mm. Interaction of the rising flux rope with large-scale convective motion produces the bipolar structure of the flux rope, with the convective downflows fixing the two ends of the emerged section of the flux rope in the convection zone. Near-surface small-scale convection produces the pores by coalescence and intensifies the strength of the magnetic flux inside the pores. Here, we examine a region of magnetic flux cancellation at the photosphere in our simulation, which is characterized by high magnetic shear. Flux cancellation of this form is particularly significant as it has been observed to be associated with flares (Martin et al., 1985) and CMEs (Subramanian & Dere, 2001) in active regions. A clear example is observed in AR 10977, where reconnection at the PIL during flux cancellation forms a highly sheared arcade and sigmoidal structure that subse-

quently reforms after eruption (Green et al., 2011). Li et al. (2004) found converging flows consistent with flux cancellation in decaying and young active regions producing CMEs. Inspired by similar observations, converging motion and flux cancellation have been imposed as boundary conditions in MHD simulations to produce eruptions (Linker et al., 2003; Amari et al., 2003).

As it is observed on the Sun, flux cancellation is very ambiguous as it may be caused by submergence of Ω-loops, emergence of U-loops, or magnetic cancellation by some dissipative process. Our simulation provides a unique opportunity to fully understand an example of flux cancellation in a way that is not possible through observations alone. We find flux cancellation occurs spontaneously between opposite polarities that are driven together by the convective flows near the photosphere. The temporal evolution of cancellation is shown in Figure 4.1, which shows a zoom-in view of the relevant area, with background color showing photospheric B_z field. The horizontal motions in positive and negative polarities are shown by blue and red arrows, respectively. The flux cancellation event starts at time t = 05:00:00, lasts for 0.5 hr, and the total amount of cancelled flux approaches 1×10^{20} Mx, which is 10% of the total unsigned flux on the photosphere. It is remarkable that during the process of flux cancellation, the coronal free energy (shown in the left panel of Figure 4.6) is still increasing even though the photospheric magnetic flux is decreasing.

To understand this process, we take close examination of the velocity fields in the area of flux cancellation prior to, during and in the later phase of the event, as shown by Panel (a), (b) and (c) in Figure 4.1, respectively. In Panel (a), the two polarities are pushed together by the horizontal converging motion at the two sides of the PIL. The flow pattern at the PIL is mostly converging and forms a very narrow PIL at a later time illustrated in Panel (b). Panel (b) shows a clear shearing motion at the PIL, with two polarities running in opposite directions. The strong shear flow at the PIL is driven by the Lorentz force, and takes place during the flux cancellation

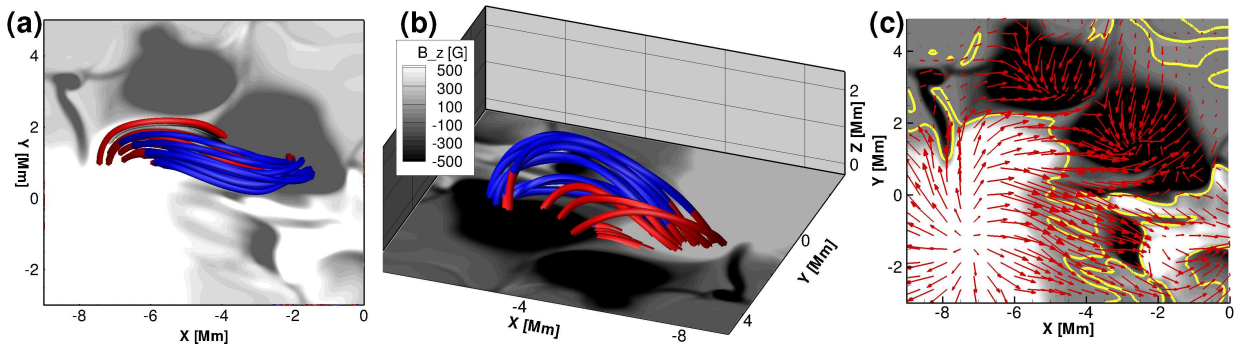

Figure 4.2: The structure of the magnetic fields in the area of flux cancellation at time t = 5:05:00 from top (a) and side (b) view. The background planes show the photospheric B_z field. Color on the rods indicates the vertical velocity at which the field lines are moving, with blue showing rising lines and red submerging. The red arrows in Panel (c) represent the horizontal magnetic field, with yellow line showing PIL.

as the magnetic field expands in the corona as shown by the blue colored field lines in Figure 4.2. Panel (a) of Figure 4.4 shows the horizontal Lorentz force at time t = 05:01:00 with arrows, from which we find a clear pattern of the force running in the opposite directions across the PIL in the area of flux cancellation. At time t = 5:22:00, toward the end of the flux cancellation, the flow pattern becomes converging again, dominated by the convective motion. The weak-strong-weak shearing motion in the flux cancellation event is also shown by observations (Su et al., 2007) during flares where footprints of the magnetic fields present the same pattern of motion.

Figure 4.2 shows the configuration of the magnetic fields in the area of flux cancellation at time t = 05:05:00. Panel (a) provides the top view of the fields, and we find that instead of short loops perpendicular to the PIL, as is the case for potential fields, the field lines are instead elongated parallel to the PIL. Furthermore, the fields are more parallel to the PIL as they become closer to it, as shown by the red arrows in Panel (c) of Figure 4.2. The elongation of the field lines is clearly the result of shearing motion, which is further enhanced by the converging motion at the PIL (Martens & Zwaan, 2001). These converging motions also give rise to tether-cutting reconnection

in the highly sheared fields as proposed by Moore et al. (2001) as an explanation for solar eruptive events. Moore et al. (2001) envisioned reconnection inside a highly sheared core field, which would produce longer, nearly horizontal field lines higher in the corona, while at the base of the arcade, a system of short unsheared loops would form. This flux transfer process accumulates the free energy of the sheared field higher in the corona while at the same time reducing the magnetic tension by binding the system to the photosphere. The rise of the arcade naturally leads to necking off of the fields, which in turn, promotes more reconnection. Unabated, the runaway reconnection provides a mechanism for the initialization and growth of explosive events. With our simulation, we can fully examine the way in which submergence and reconnection alter the field line geometry in the tether-cutting process. A 3-D view of the magnetic fields combined with the flow pattern provides a complete picture of the effects of the internal reconnection. Panel (b) of Figure 4.2 illustrates the structure of the magnetic field lines colored by the vertical velocity at which the lines are moving. Blue indicates upflows and red downflows. We find two groups of magnetic field lines formed during tether-cutting reconnection, with one rising up into the corona and the other, shorter loops, submerging into the convection zone. Both groups of the magnetic fields are escaping from the photosphere, leading to the decreased unsigned flux observed at the surface. Magnetic shear accumulates along the long, rising loops, forming a highly sheared arcade.

To study the energy transport into the corona during flux cancellation, we examine the Poynting flux at $Z = 3$ Mm associated with the vertical motions. At the surface, the vertical motion transports the energy back into the convection zone due to the concentration of the magnetic flux in downflows. In the corona, the acceleration of magnetic fields after reconnection plays a very important role in the energy flux, shown by Panel (e) in Figure 4.8. At the PIL in the corona, we observe a strong energy input associated with the rising motion of the fields. The rising motion here

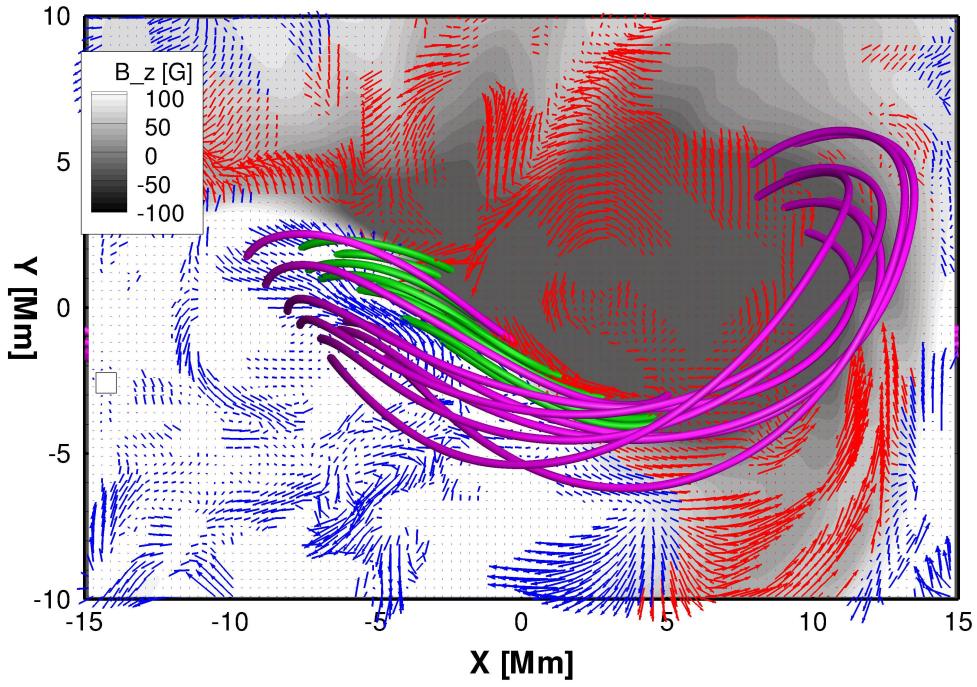

Figure 4.3: 3-D structure of the magnetic fields in corona at time t = 5:05:00. The background planes show the B_z field at Z = 3 Mm. Green rods represent low-lying field lines below 5 Mm with purple showing high field lines. The blue and red arrows show the horizontal velocity in positive and negative magnetic polarities, respectively. There is a clear shear flow along the polarity inversion line. The negative polarity also shows some signs of rotation, while the positive polarity shows only a coherent shear flow. The magnetic field lines clearly reflect the flow pattern.

in the corona, however, is different from the emerging motion at the photosphere. At the photosphere, the emergence is caused by the expansion and buoyancy of the flux rope as well as convective upflows. However, in the corona, the magnetic fields are accelerated upward by the energy released from the tether-cutting reconnection in the highly sheared core field.

Besides reconnection and shear flows, rotation of the magnetic polarities also contributes to the accumulation of magnetic shear by moving the footpoints in opposite directions at the PIL. Figure 4.3 shows the geometry of two groups of coronal magnetic field lines: purple overlying lines with apex higher than 5 Mm, and green lines lower than 5 Mm. Horizontal velocity fields at $Z = 3$ Mm, represented by the arrows,

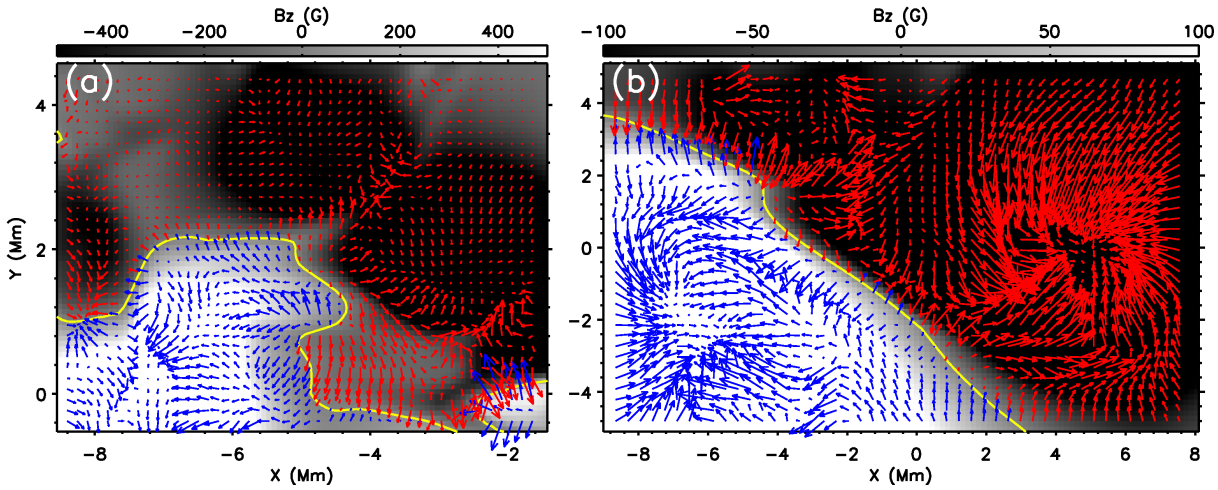

Figure 4.4: The structure of horizontal Lorentz force on Z = 0 (a) and Z = 3 Mm (b) planes at times t = 05:01:00 (a) and 05:05:00 (b), respectively. The blue and red arrows represent Lorentz forces in positive and negative polarities, respectively. The magnitude of B_z field component is shown in gray scale. Note that the Lorentz force reverses direction across the polarity inversion line driving the shear flow, and forms a spiral pattern in the negative polarity driving a rotating flow.

show a rotation pattern on the negative polarity, which is also seen in Figure 4.8. The rotation complements the shearing motion at the PIL, in the sense that both shear and rotation are parallel at the PIL. However the flow patterns are also quite distinct occurring at different scales and at different times. The shear flows are localized to the PIL and persist even when there is not a coherent rotation pattern in one pore or both pores as seen in Figure 4.1. When rotation is present in the pores, the shear flow tends to be greater in magnitude and will be shown graphically to dominate the energy transport into the corona.

The combination of the two motions creates a highly sheared arcade at the PIL, shown by the green rods in Figure 4.3, and rotation produces the twisted field structure at the far ends of the emerged fields, shown by purple rods. Both motions are driven by Lorentz force, as shown by the arrows in Panel (b) of Figure 4.4. At the PIL, the horizontal Lorentz force runs in the opposite direction, consistent with the

directions of the shearing motion. In the negative polarity, the Lorentz force rotates in the same way of the rotation of the polarity. The sigmoidal structure at the PIL is maintained by the consistent shearing and rotating motions in our simulation. The relative contribution of shear flows compared to rotation can be seen in the geometry of the coronal fields at the PIL. Here, the field is dominated by an arcade structure instead of a twisted flux rope. Most of the twist is located at the outer periphery of the two polarities. Even in the most twisted field lines, there is less than a full turn of the field around the axis of either pore. The absence of the twisted flux rope may be explained by two facts: the axis of the initial magnetic flux rope remains in the convection zone; and there is not enough writhing or braiding motion on the surface to reproduce such a twisted structure after emergence. The emerged fields are sheared and elongated, forming the arcade structure over the PIL.

4.2 Non-potentiality of the Magnetic Field

During our simulation, horizontal motions at the photosphere transfer a significant amount of energy, up to 7×10^{31} ergs, into the corona. The question is then, how much of the magnetic energy is the free energy, which is necessary for solar eruptive events. Magnetic free energy, is present in a sheared configuration where the field lines run almost parallel to the PIL instead of perpendicular or in a twisted field. To investigate the evolution of magnetic free energy, we compare the coronal magnetic fields in our simulation with potential fields extrapolated from the photospheric boundary conditions. Figure 4.5 shows the temporal evolution of the model fields (blue) and the extrapolated potential fields (red). Comparison between the two fields clearly shows the buildup of magnetic shear along the field lines during the process of flux emergence. At time t = 04:05:00, shown by the upper-left panel in Figure 4.5,the magnetic flux concentrates in two polarities, with most of the field lines running perpendicular to the PIL. The energy transfer into the corona occurs as the magnetic

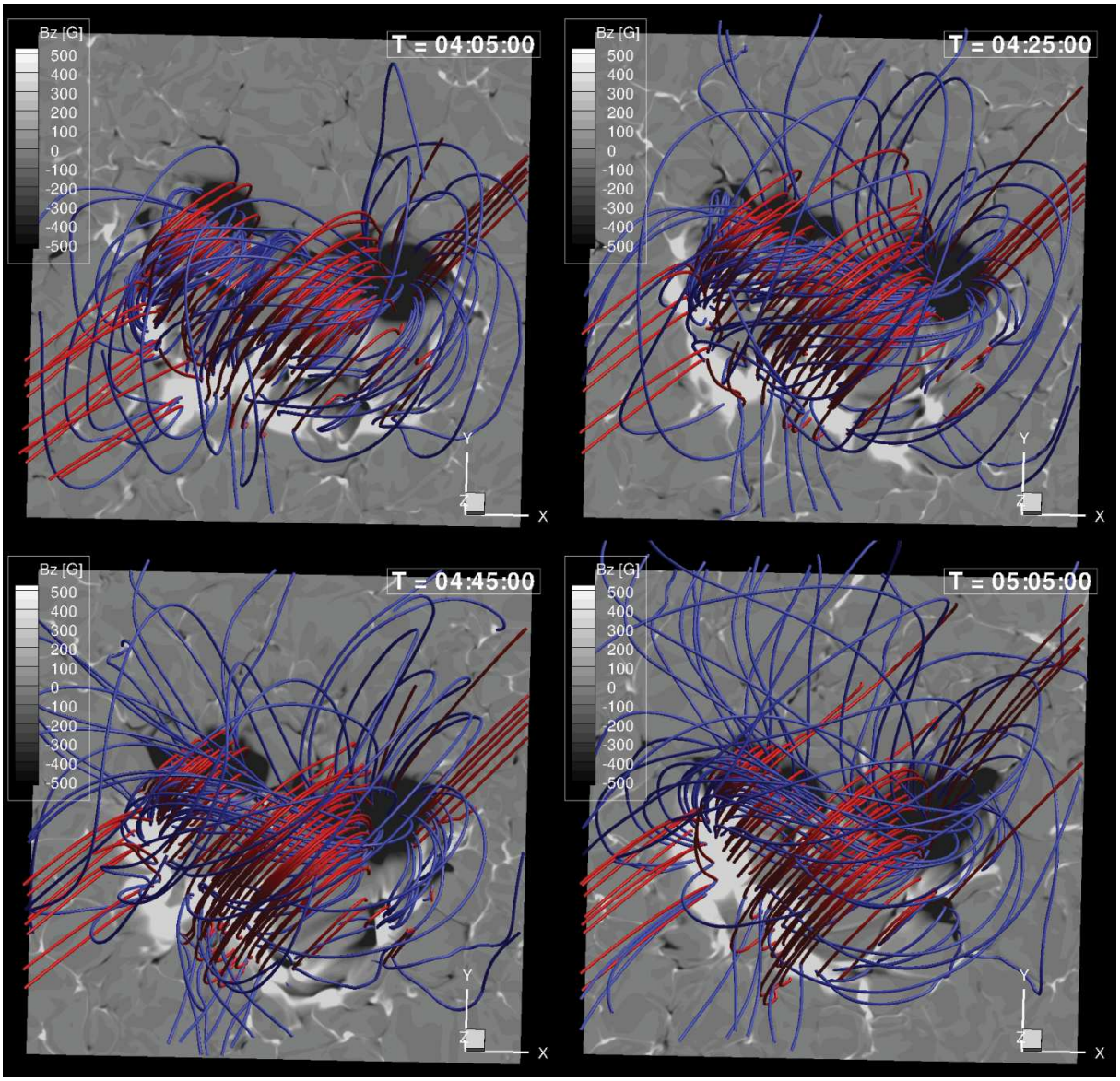

Figure 4.5: Comparison of the model field (blue) with the extrapolated potential field (red) at time t = 04:05:00, 04:25:00, 04:45:00 and 05:05:00. The color on the plane shows the B_z field at the photosphere. The clearest departure in field line direction occurs at with the sheared field lines above the PIL.

field lines become elongated and sheared along the PIL. The lower-right panel in Figure 4.5 shows the field structure at time t =05:05:00, in which the field lines are sheared along the PIL and compressed into the lower atmosphere while the overlying fields remain almost potential. The simulated configuration of the magnetic fields in our domain is consistent with observations and simulations of the magnetic fields

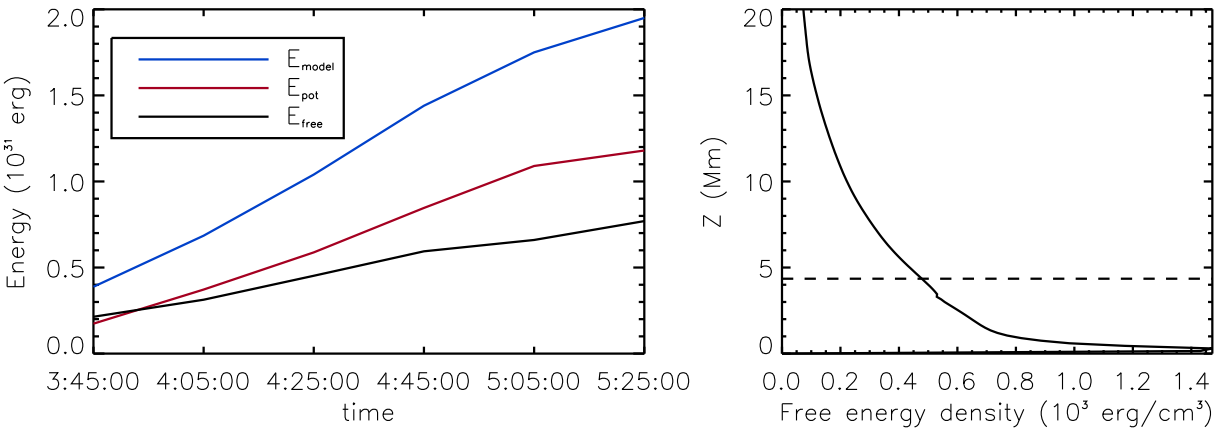

Figure 4.6: Left: temporal evolution of the total (blue), potential (red) and free (black) magnetic energy. Right: vertical distribution of free energy density at time t = 05:05:00. The dashed line indicates the altitude up to where 50% of the coronal free energy is stored.

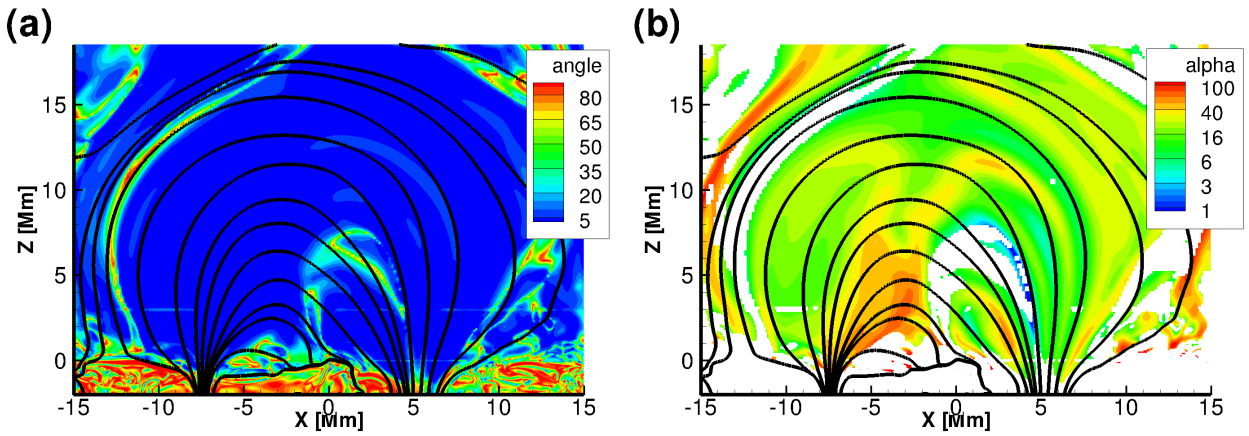

Figure 4.7: (a): the angle between the current and magnetic fields (b): the α structure on the Y = 0 plane. Black lines are the magnetic field lines and white regions in Panel (b) are areas where the angle between the current and magnetic fields are greater than 10°.

before solar eruptions (Schrijver et al., 2008; Leake et al., 2010). The overlying fields confine and compress the sheared core in the lower atmosphere, which may be destabilized and give rise to sudden release of magnetic free energy.

Here, we calculate the free energy for the simulation by integrating the magnetic energy for the model and subtracting the energy of the potential field. The results are shown in the left panel of Figure 4.6 where the temporal evolution of model, potential

and free energy is plotted with blue, red and black lines, respectively. Beginning at time t = 04:05:00, the amount of free energy doubles within one hour (the period shown by Figure 4.5), such that the coronal free energy approaches 7×10^{30} ergs while the total energy is 1.7×10^{31} ergs. At this time, the free energy contributes to 40% of the total energy. Meanwhile, the vertical stratification of the free magnetic energy, is shown in the right panel of Figure 4.6. The line plot shows a strong tendency of concentrating free energy in the lower atmosphere, with 50% located below $Z = 4$ Mm, shown by the dashed line. Figure 4.7 shows the angle between the current and the magnetic field in Panel (a) and the structure of α ($\frac{|\mathbf{j}|}{|\mathbf{B}|}$ when the angle between them is less than 10°) in Panel (b) in the Y = 0 plane. The non-force-free magnetic fields mainly reside in the convection zone, and in the core sheared field close to the surface (see Panel (a)). Note that α tends to be maximized low down the center of the arcade structure and then falls off with distance from the PIL.

4.3 Poynting Fluxes

To separate the energy transfer associated with vertical and horizontal flows, we decompose the Poynting flux into two components, described by Equation 3.3 and 3.4: F_{shear} associated the horizontal motions and F_{emerg} with the vertical motion. The horizontal motions, at the photosphere, include the separation of small dipoles, rotation, and the shearing flow along the PIL. Panels (b) and (c) of Figure 4.8 show the structures of F_{emerg} and F_{shear}, respectively, with the arrows representing the horizontal velocity fields. It is clear that in regions with rotation or shearing there is a strong energy input into the corona. Comparison of the structures of F_{emerg} and F_{shear} suggests that horizontal motion dominates in the energy transfer during the current phase of emergence, while vertical motion transfers energy back into the convection zone, due to the concentration of magnetic flux in downflow regions (see Chapter II and III). Vertical emerging motion dominates at the very beginning of the

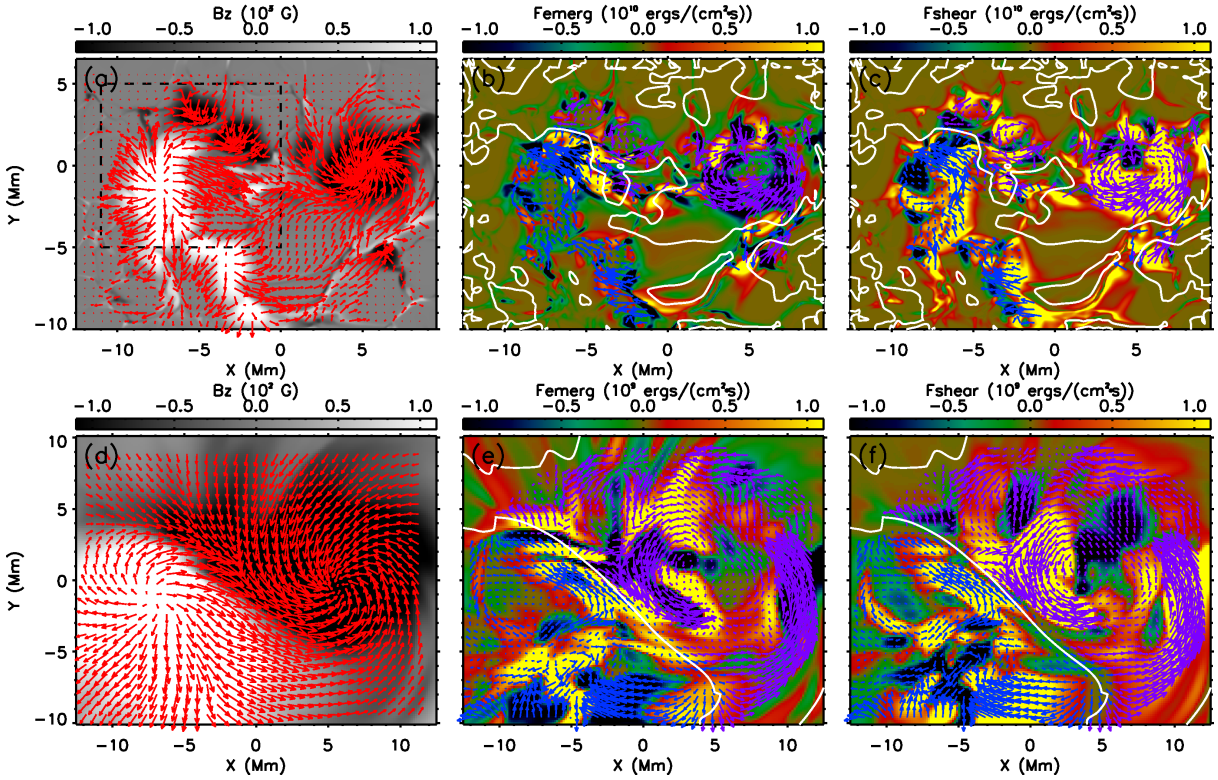

Figure 4.8: The structure of B_z (a and d), F_{emerg} (b and e) and F_{shear} (c and f) fields at the photosphere (a, b and c) and at Z = 3 Mm in the corona (d, e, and f) at time t = 05:05:00. PIL is shown by the white line. Red arrows in Panel (a) and (d) represent the horizontal magnetic fields. Blue and purple arrows in (b, c, e and f) show the horizontal velocity in positive and negative magnetic pores, respectively.

flux emergence, and later gives way to horizontal motions, a pattern found earlier by Magara & Longcope (2003) and Manchester et al. (2004).

At the photosphere, the magnetic field is very highly structured by convection. In particular, the flow patterns and Poynting fluxes can be difficult to interpret with a large component of their structure being caused by random convective motions. To get a better understanding of the dynamics, we plot the vertical field strength, flow field and Poynting fluxes in the low corona at a height of $Z = 3$ Mm in Panels (d), (e) and (f) in Figure 4.8. Here, in the corona, the magnetic field expands and smooths out as the plasma beta drops. This transition allows us to make a much clearer

picture of the relevant structures. The flux expands to form two nearby polarities and an elongated PIL between them, shown by Panel (d). Here, the presence of a highly sheared field is obvious in the red arrows showing the horizontal field direction. The negative polarity pore shows little discernible twist while the negative polarity is clearly twisted. Flows are completely dominated by shearing motion at the PIL and rotation in the polarities. Both flows make a significant contribution to the energy transfer, but the energy transported by shear flow tends to be more consistent in time than that of rotational flows. In particular, the shearing motion at the PIL not only builds up the energy in a confined region along the PIL, but also leads to the occurrence of magnetic reconnection taking place in the dashed square in Panel (a) of Figure 4.8, discussed in Section 4.1.

4.4 Summary and Conclusions

Our simulation provides us with a unique opportunity to study an example of magnetic flux emergence in a realistic simulation of the convection zone, coronal system. The system shows a wealth of complexity and interaction of mutiple physical processes, which conspire to transport magnetic flux and free enegy from the convection zone into the corona. The emerging magnetic flux interacts with convective cells of varying scalesas it approaches the photosphere, and then accumulates in convective downdrafts to form a bipolar magnetic structure resembling solar pores. The magnetic field continually expands into the upper atmosphere, which results in shear flows and rotating motions that combine to draw the field nearly parallel to the PIL, and transport energy into the corona. At a later time, converging motions at the PIL cause flux cancellation at the photosphere along with tether-cutting reconnection, which produces highly sheared, sigmoidal shaped field lines high in the corona. The resulting field configuration contains significant amounts of free magnetic energy essential to solar euptions.

In the process of building up the magnetic free energy, shearing flows play a significant role at the photosphere and in the corona. At the near surface layers, the angle between the current and magnetic fields ranges from 35° to 90°. The geometry of current and magnetic fields then produces the Lorentz force at the surface, which drives the rotating and shearing motions and increases the non-potentiality of the magnetic fields over a period of hours after the emergence. In particular, the shearing flows align the magnetic fields nearly parallel to the PIL and transport significant amount of magnetic energy from convection zone into the corona during the flux emergence, consistent with observations by Schrijver et al. (2005). The shearing flows at the PIL are accompanied by periods of rotating motion of the pores. Both of the two motions contribute to the build up of magnetic shear and free energy in the corona. However, the shearing motions distinguish themselves from the rotation by their persistent presence and concentration at the PIL where the field has an arcade structure, while rotation on the other hand is only present in one of the pores and lasts only for 1 hour. It is the long-lasting, Lorentz-force driven shearing motion that dominates the energy transfer and builds up the free energy powering eruptive events.

Convection-driven converging motion drives flux bundles of opposite polarities together, producing a strong magnetic gradient and a pronounced PIL, a situation favorable for large flares (Schrijver, 2007; Falconer et al., 2008). The horizontal converging motion at the PIL also contributes to the development of the magnetic shear of the field lines by increasing the shear angle (Martens & Zwaan, 2001). The combination of converging and shearing flows at the PIL forms a group of highly sheared arcades overlying a sharp magnetic PIL. Within this arcade, converging motions lead to the occurrence of tether-cutting reconnection, producing two types of field lines: one long sheared expanding loops and the other unsheared submerging loops. The short loops sink into the convection zone at the speed of convective flows, up to 2 km/s, consistent with Harvey et al. (1999), which continuously reduces the photo-

spheric unsigned flux. The longer loops rise into the corona with more magnetic shear. The shearing motion along the PIL plays a very important role in that it both produces a sheared arcade structure ready for reconnection and accumulates magnetic shear in the field lines formed after the reconnection. The magnetic configuration of this area thus yields a high free energy up to 40% of the total, which is approaching the threshold value for eruptions (Moore et al., 2012).

Shear flows, converging motions, and tether-cutting reconnection combine to continuous building up of the magnetic shear and free energy in the corona necessary for eruptive and explosive events. The magnetic reconnection and shearing motion at the photosphere produce the sigmoid-shaped field geometry, which is preferential for CMEs (Canfield et al., 1999), and the persistent sheared arcade structure is consistent with many CME models (e.g. Steinolfson, 1991; Mikic & Linker, 1994; Amari et al., 1996; Guo & Wu, 1998; Antiochos et al., 1999). Futhermore, we find that the coronal free energy grows at a rate of 3×10^{30} ergs/hr, which build up $10^{32} \sim 10^{33}$ ergs, sufficient for CMEs, over a period of several days. Such a build up rate is observed by Schrijver (2007) prior to large flares. Moreover, the majority of the free energy resides low in the corona where it can be confined and later released by reconnection. Finally, we note that the consistent shearing motion and reconnection at the flux cancellation site keep reforming the sigmoid structure, which is essential for homologous eruptive events.

CHAPTER V

Comparison between Simulations and Observations

Eruptive events are associated with the rapid, irreversible changes in the photospheric and coronal magnetic fields, during which a tremendous amount of plasma and energy are released powering the eruption (Forbes et al., 2006; Low, 2001; Schrijver, 2009). Observations of solar activity over the past decades have advanced our understanding of the nature of solar magnetic eruptions. Strong PIL (Schrijver, 2007), magnetic shear (Hagyard et al., 1984; Falconer et al., 2006), shearing flows (Schrijver et al., 2005; Deng et al., 2006), converging motion (Li et al., 2004) and flux cancellations (Martin et al., 1985; Subramanian & Dere, 2001; Green et al., 2011) are found to be strongly correlated with the occurence of solar eruptions, such as CMEs, flares and filament eruptions. In addition to observations, numerical simulations also identify the important role of these mechanisms in the formation of the magnetic geometry prone to eruptions (see Section 1.2.3). Shear flows, converging motion, and flux cancellation are applied as boundary conditions in many models of CMEs and flares and are found to drive instabilities and eruptions (Steinolfson, 1991; Mikic & Linker, 1994; Amari et al., 1996; Guo & Wu, 1998; Amari et al., 2003).

In particular, the simulation discussed in Chapter III produces a flux cancellation event examined in Chapter IV that illustrates the process of building up free magnetic energy during flux emergence and cancellation in a more realistic simulation.

The combination of shearing flows and the converging motion at the PIL produces a highly sheared magnetic geometry along the PIL and promotes the occurence of the tether-cutting reconnection (Moore et al., 2001). Reconnection and submergence result in the magnetic flux cancellation at the surface, and more importantly, in the transfer of magnetic shear to longer magnetic loops. It is notable that the persistent shearing flows dominates the energy transfer into the corona and build up magnetic free energy that can power eruptions. To elucidate these processes, we compare our simulation results presented in Chapter III and IV with the observational characteristics of AR11158 in Feb 2011, focusing on the following features: the photospheric magnetic and velocity fields; the coronal magnetic geometry and the free magnetic energy.

5.1 Observations on AR11158

The *Solar Dynamic Observatory* (SDO), launched on Feb 11, 2010, observes the activity of the photospheric and coronal magnetic fields in great detail (Pesnell et al., 2012). The Helioseismic and Magnetic Imager (HMI) on SDO observes the full Sun, creating Dopplergrams and Line of Sight (LOS) magnetograms every 45 sec with $0.5''$ spatial resolution, and vector magnetograms with a 12-min cadence. With the high-cadence, high-resolution measurements of photospheric magnetic fields, HMI provides the first full-disk continuous observation of the evolution of vector magnetic fields in active regions (Scherrer et al., 2012). Meanwhile, the Atmospheric Imaging Assembly (AIA) on SDO obtains images of the Sun in the extreme ultraviolet (EUV) wavelength every 12 sec with $1.5''$ spatial resultion, at ten wavelength bands covering temperature ranges from 6×10^4 to 2×10^7 K. With simultaneous multi-wavelength observations, it monitors the coronal and chromospheric regions up to 0.5 R_s above the surface (Lemen et al., 2012).

Observed continuously by HMI and AIA, AR11158 presents a complex structure

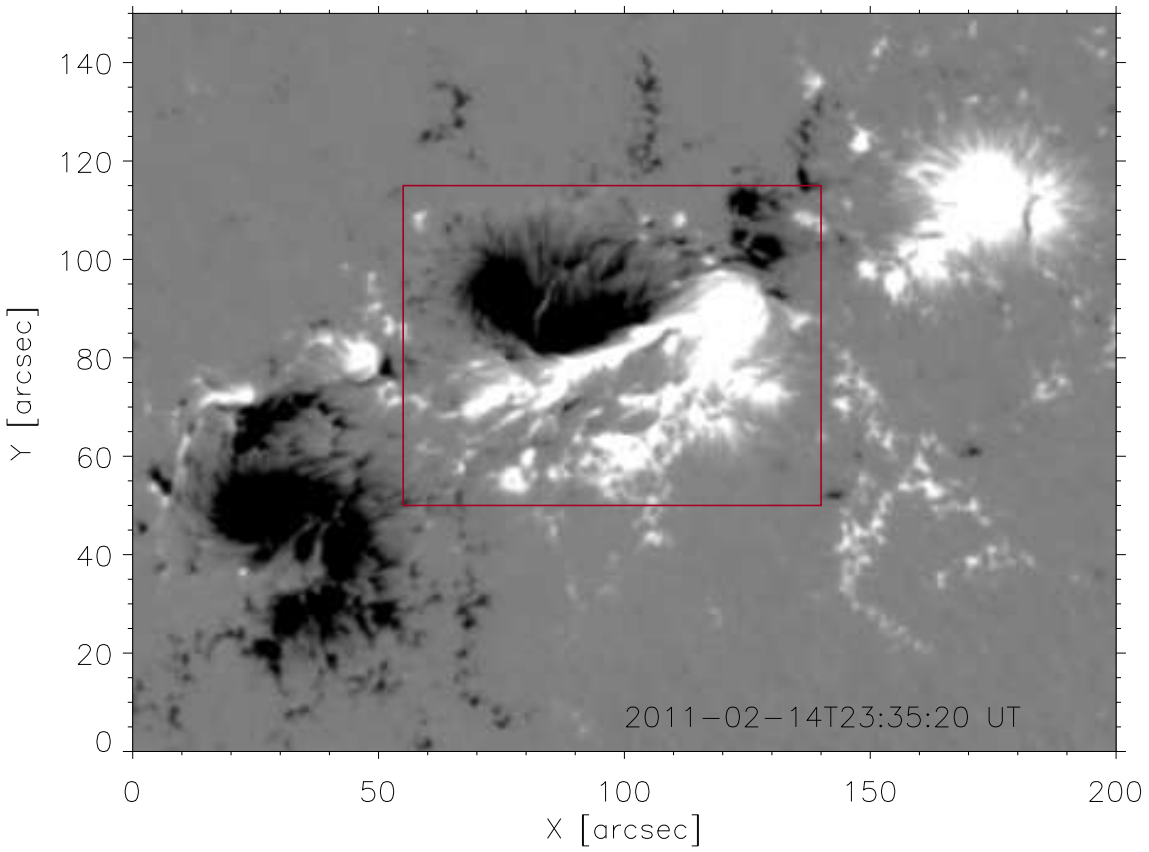

Figure 5.1: The B_z field on the photosphere in AR 11158 observed by HMI at time 2011 Feb 14 23:35:30 UT. The red box indicates the area where the flux cancellation takes place and the field of view of HMI images in Figure 5.4, 5.3 and 5.2.

with two pairs of magnetic bipoles emerging at the same time, as shown in Figure 5.1. The active region starts to form on Feb 12, 2011, and during its 5 days of observed evolution, it produces 2 M- and 1 X- class flares accompanied by a halo CME (Schrijver et al., 2011). The X2.2-class flare starts at 1:44 UT on Feb 15, 2011 and is the first X-class flare in Solar Cycle 24, also called the Valentine's Day flare. On the photosphere, the formation of AR11158 is associated with quick flux emergence centered at three sites. It is unclear whether or how the sites of flux emergence are magnetically connected in the solar interor. However, the coronal structures and the photospheric topology of the magnetic fields suggest that the magnetic structure in this active region is of great complexity. Sun et al. (2012) study the evolution of

the magnetic field and the free energy in this active region using a time series of HMI and AIA observations combined with Non-Linear Force-Free Field (NLFFF) extrapolations, and find that the magnetic structures exhibit strong shearing and store significant amouts of free energy during the early flux emergence. During the flare, horizontal fields are strongly intensified at the PIL (Sun et al., 2012; Wang et al., 2012; Gosain, 2012). NLFFF extrapolations suggest the existence of strong currents in the low atmosphere, which collapse downward after the eruption (Sun et al., 2012; Liu et al., 2012). The variations in the observed and extrapolated magnetic structures are suggestive of tether-cutting reconnection at the PIL leading to the flare eruption (Liu et al., 2012).

5.2 Photospheric Velocity and Magnetic Fields

Evolution of the photospheric magnetic fields in AR11158 can be described as the following three stages characterized by these features (Sun et al., 2012): fast flux emergence with a rate of 10^{20} Mx/h; slower emergence but strong shearing motions between the opposite polarities together with simultaneous flux cancellation at the PIL; and episodic flux emergence and cancellation with persistent shearing flows. The second stage, with the presence of shearing flows and flux cancellation, produces the X2.2-class flare, and therefore is of great interest to compare with the flux cancellation event in our simulation.

In AR11158, a strong PIL forms between the two polarities during the flux emergence, outlined by the red box in Figure 5.1. In the vicinity of the PIL, strong shear flows are observed prior to the flare, shown in Panel (a) of Figure 5.2. Red and blue arrows distinguish the horizontal velocity fields in negative and postive polarities, which shows that along the major PIL, the nagative polarity is moving downward while the positive is upward. The opposite motions of the two polarities are highly concentrated in the vicinity of the PIL, and persist even after the flare, shown in

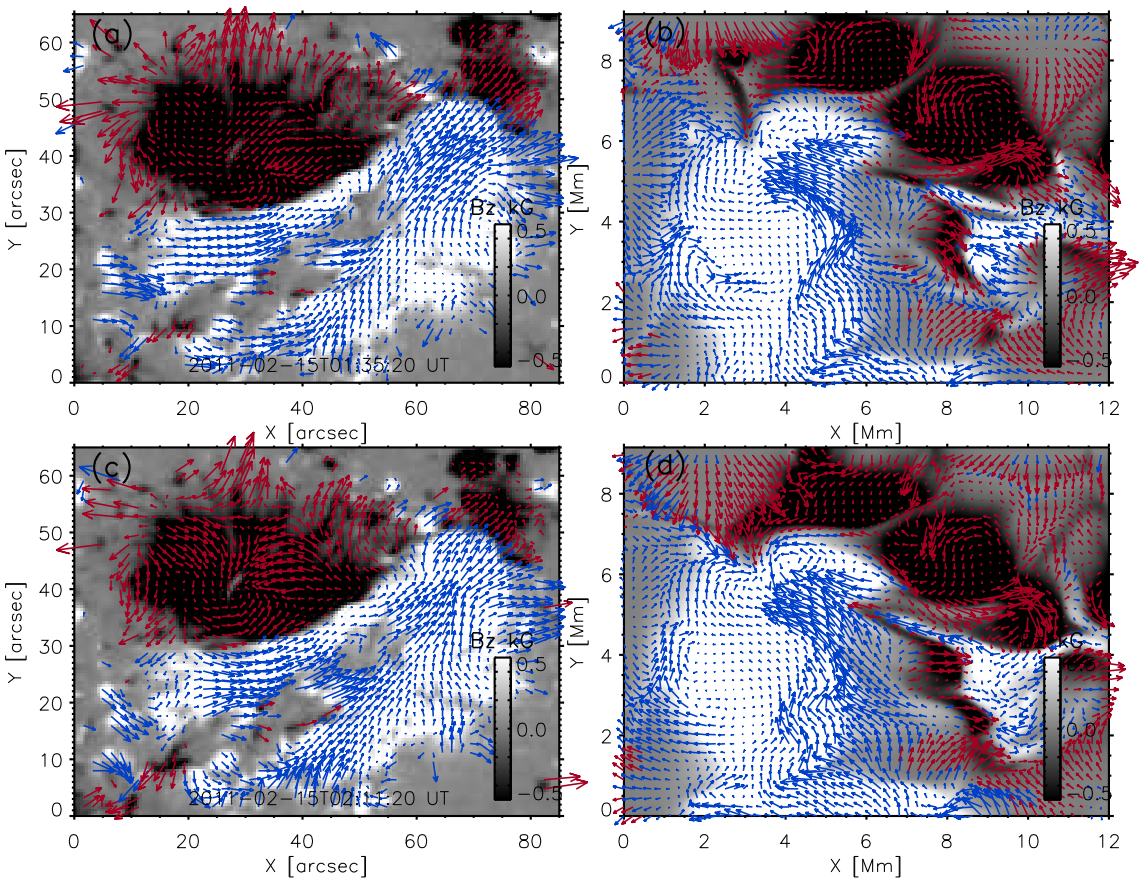

Figure 5.2: Comparison of B_z field in AR11158 (a and c) and in the model (b and d) with red and blue arrows showing the horizontal velocity fields in negative and positive magnetic polarities, respetively. Panel (a) and (c) are taken by HMI at 2011 Feb 15 01:35:20 UT and 02:11:20 UT, respetively. Panel (b) and (d) are simulation results at time t = 05:11:00 and 05:16:00.

Panel (c). The simulation results, discussed in Chapter IV, also demonstrate a clear shearing pattern along the PIL in the horizontal flow fields during the flux cancellation event, as shown in Panel (b) and (d). The consistency of the shearing flows in the model and AR11158 validates the importance of the shearing flows in driving solar magnetic instabilities and eruptions (Steinolfson, 1991; Mikic & Linker, 1994; Guo & Wu, 1998; Amari et al., 2003; Manchester et al., 2004; Deng et al., 2006; Su et al., 2007). These shearing flows are driven by the reversal of the Lorentz force across the PIL, as shown by Panel (a) of Figure 4.4 (Manchester & Low, 2000).

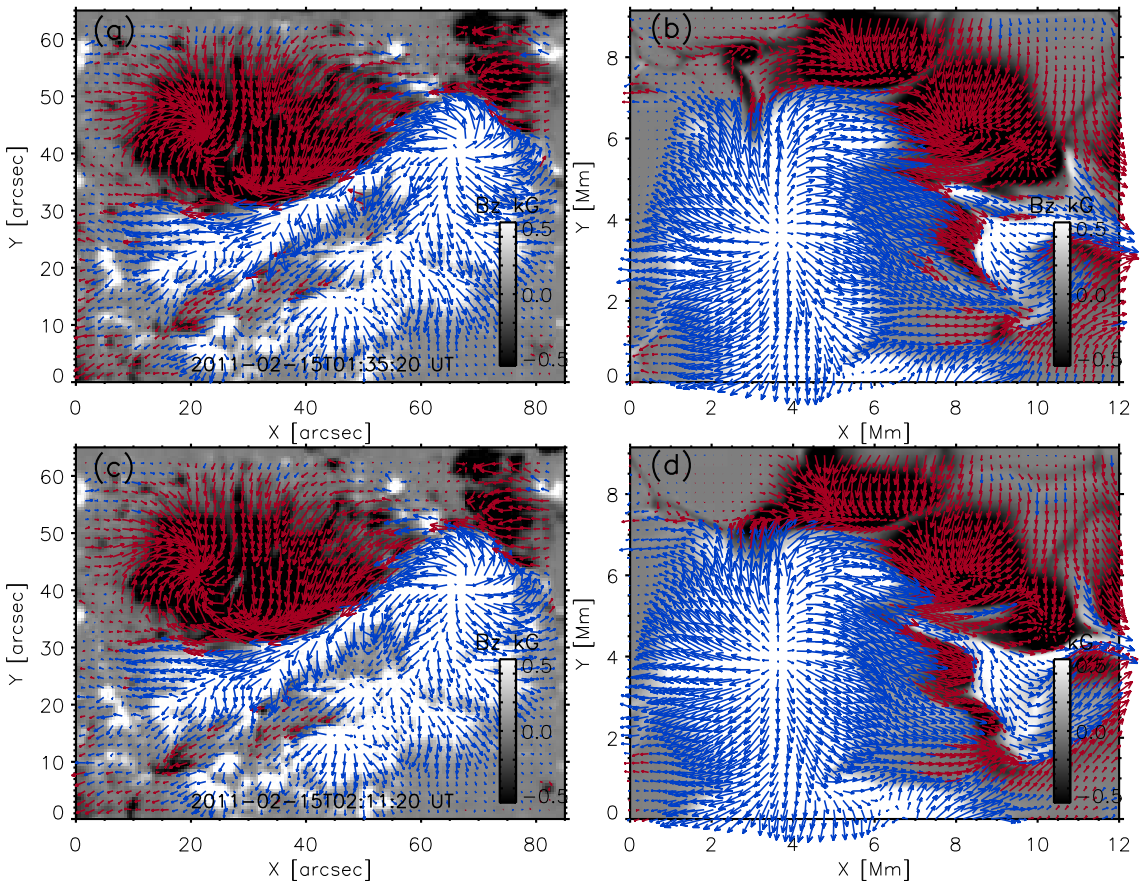

Figure 5.3: Comparison of B_z field in AR11158 (a and c) and in the model (b and d) with red and blue arrows showing the horizontal magnetic fields in negative and positive magnetic polarities, respetively. Panel (a) and (c) are taken by HMI at 2011 Feb 15 01:35:20 UT and 02:11:20 UT, respetively. Panel (b) and (d) are simulation results at time t = 05:11:00 and 05:16:00.

The strong, persistent shearing flows along the PIL pull the magnetic fields parallel to the PIL, leading to a highly sheared field structure observed by HMI vector magnetogram. The magnetic fields change quickly to a highly sheared geometry when approaching the PIL, while away from the PIL, they are in a more relaxed state, as shown by the left panels of Figure 5.3. The transition of relaxed-sheared-relaxed state of the magnetic fields across the PIL is also found in our simulation results (see Panel (b) and (d)), whose 3-D structure is shown in Figure 4.2. It is clear both in observation and simulation that, on the photosphere the magnetic shear is highly

concentrated in the very vicinity of the PIL, corresponding to the increasing strength of shearing flows. The sharp transition into a highly sheared structure in the confined area along the PIL therefore suggests a 3-D magnetic structure with a significant amount of free energy stored right above the PIL, while the confining fields are in a relaxed, less-energetic state, as shown in Figure 4.5. This magnetic configuration, with a high magnetic shear at PIL, is strongly correlated with the CME and flare productivity (Hagyard et al., 1984; Falconer et al., 2002, 2006).

During the flare event in AR11158, the presence of the velocity shear is accompanied by a strong variation in the horizontal magnetic fields. Panel (a) and (c) show the strength of the horizontal magnetic fields before and after the X2.2-class flare, respectively, with the red lines representing the PIL. It is clear that the the horizontal magnetic fields are strongly intensified along the PIL during the flare. The variation of the horizontal fields is illustrated by Panel (e), which shows that at the PIL the field strength increases by over 300 G. The average horizontal magnetic field strength along the PIL increases from 1200 G to over 1500 G (Sun et al., 2012; Wang et al., 2012; Gosain, 2012). Interestingly, during the flux cancellation event in our model, the horizontal fields also undergo an striking intensification along the PIL, shown in Panel (b) and (d). Panel (f) shows the difference image between Panel (b) and (d).

5.3 Free Magnetic Energy

Both shearing flows and the reconnection at the PIL contribute to the formation of highly sheared, non-potential coronal magnetic fields and the buildup of the coronal free magnetic energy, the energy source for solar eruptions. It is thus of great interest to study how the coronal fields respond to the injection of free energy. Sun et al. (2012) apply the NLFFF extrapolation to the photospheric magnetic fields in AR111158 and calculate the vertical stratification of the free magnetic energy in the corona by comparing NLFFF fields with potential fields. As shown in Panel (a) of Figure 5.5,

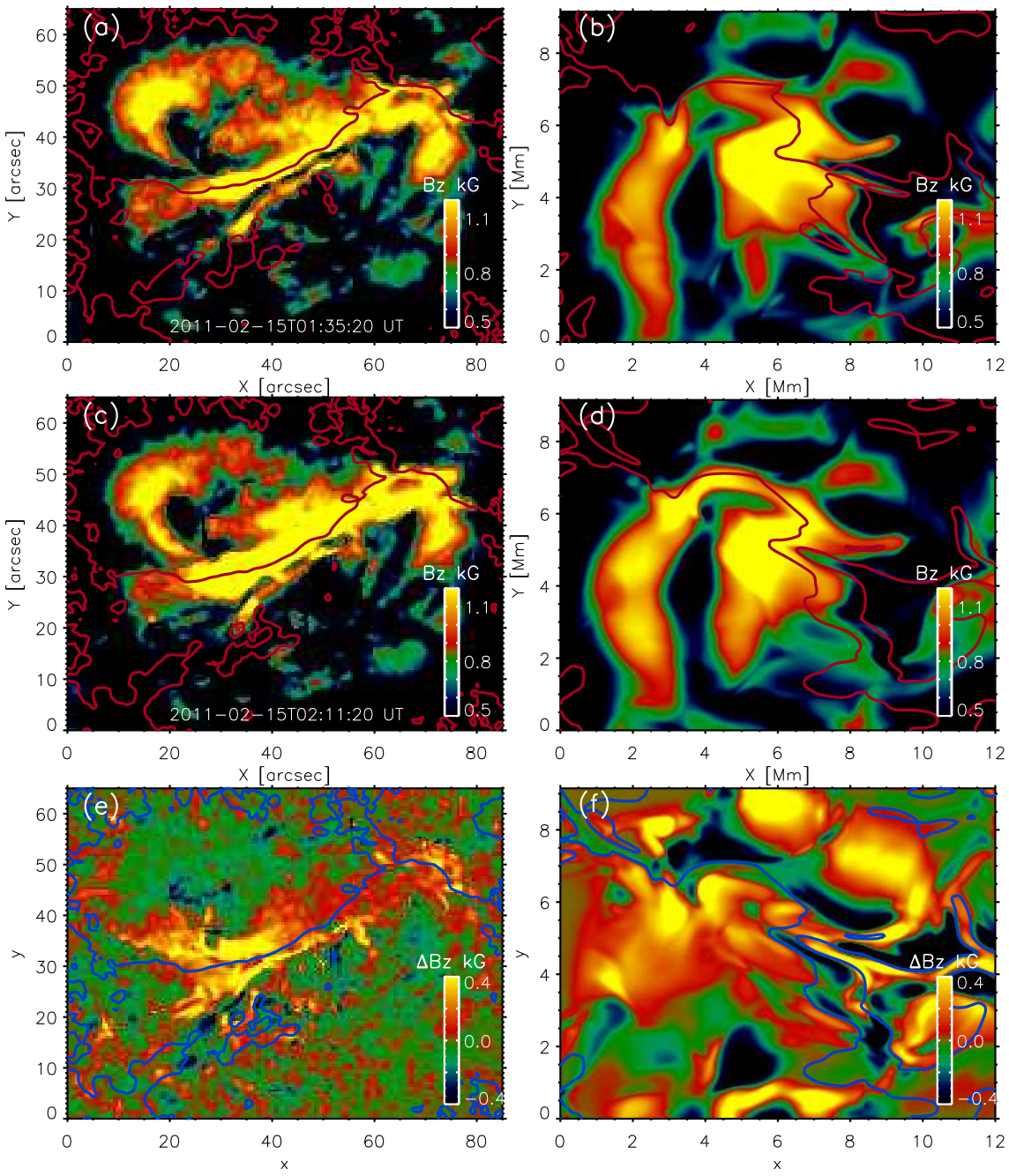

Figure 5.4: The strength of horizontal magnetic fields in AR11158 at time 2011 Feb 15 01:35:20 UT before the flare (a) and at time 2011 Feb 15 02:11:20 UT after the flare (c); horizontal fields in the model at time t = 05:11:00 (b) and 05:16:00 (d). Panel (e) shows the difference between Panel (a) and (c) while Panel (f) shows difference between Panel (b) and (d). The red contour lines in Panel (a)-(d) and the blue lines in Panel (e) and (f) represents the PIL.

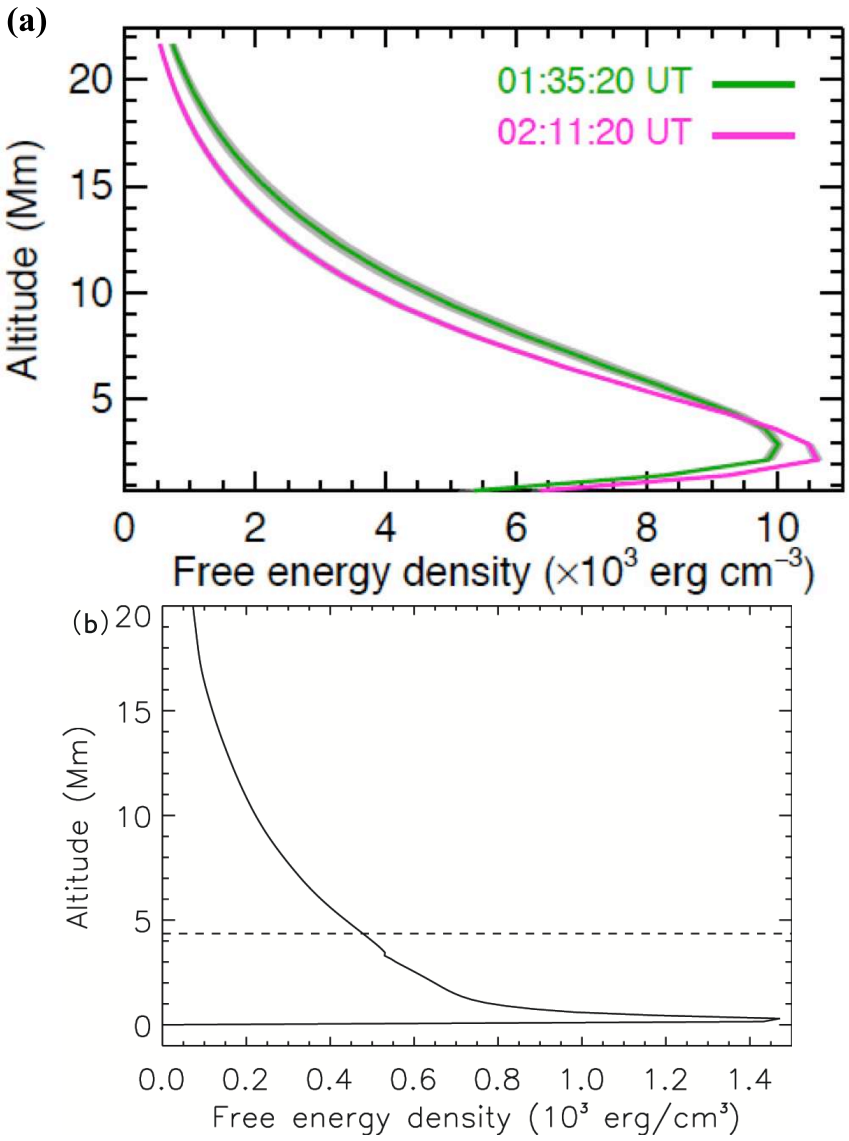

Figure 5.5: The vertical distribution of the free magnetic energy in AR 11158 (a) and model (b). The green and pink lines show the stratification before and after the X-class flare, respectively.

the free energy is concentrated in the lower atmosphere, with 50% stored below 6 Mm Sun et al. (2012). After the flare, we observed a collaspe of the free energy with height, with a larger percentage stored in the lower atmosphere, corresponding to the enhanced horizontal magnetic field. Panel (b) shows the distribution of coronal free energy in our simulation by comparing the model fields with potential fields. The free energy is concentrated even lower than the observation, with 50% stored below

5 Mm. Interestingly, the free energy in our simulation peaks at about 0.5 Mm above the photosphere, while Sun et al. (2012) report a peak at 3 Mm. This difference in the altitude of the peak free energy results from the absence of surface forces in the NLFFF extrapolated field in Sun et al. (2012), while in the simulation results the Lorentz force at the photosphere produces high free energy even closer to the photosphere. However, it is notable that both observation and simulation suggest a distribution of free magnetic energy, highly concentrated in the near-surface region and dropping rapidly with increasing altitude.

5.4 Discussion and Conclusions

Analysis of the flux cancellation event in our model (see Chapter IV) suggests the formation of highly sheared magnetic arcades in the presence of converging and shearing flows at the PIL. To compare the simulation with observations, we consider the evolution of a solar active region, AR111158, which produces a X2.2-class flare and a halo CME (Sun et al., 2012; Schrijver et al., 2011). The photospheric vector flow fields and magnetograms observed by HMI highlight the important role of velocity and magnetic shear in the development of eruptive events. During the X2.2-class flare, strong shear flows, highly sheared magnetic fields, intensified horizontal magnetic fields are observed.

Both model and observations show a significant shear in the velocity and magnetic fields during the flux cancallation, as well as the intensification of horizontal magnetic fields. The question is then, how these mechanisms combine right above the PIL to produce the observed magnetic structures and eruptions? A close examination of the 3-D structure in the simulation suggest that tether-cutting reconnection takes place in the sheared magnetic arcades, and the reconnection explains the buildup of free energy in the corona during flux cancellation at the photosphere. This physical process combines the effects of the turbulent surface flows and the geometry of the

magnetic fields at the PIL, and reveals the energy transfer in a coupled system from the convection zone to the corona. The reconnection creates two groups of magnetic loops: the shorter loops submerge to the convection zone, producing the observed decrease in the unsigned flux; the longer loops rise to the corona, transferring magnetic shear to the upper atmosphere. The submerging loops also explain the observed intensification of the horizontal fields on the photosphere and observed collapsing loops in AIA images (Sun et al., 2012). Besides the observed variations of the magnetic fields, the combination of shearing and reconnection also builds up a free energy of 7×10^{30} ergs in the model field at a rate of 3×10^{30} ergs/hr, comparable to the observed rate in CMEs.

CHAPTER VI

Conclusions and Future Work

The Sun presents an amazing varitety of magnetic structures, i.e. sunspots, active regions, and eruptive behavior such as CMEs and flares, which are driven by solar magnetic fields. Generated in the tachocline and expanding all the way into the outer corona, magnetic fields therefore act as a link between the solar interior with the outer atmosphere by making their way through the solar layers. The interaction between magnetic fields and the plasma produces a hierarchy of magnetic features throughout the Sun (See Chapter 1.2): in the interior, the operation of the solar dynamo results in the regeneration and cyclic behavior of the global magnetic fields; on the photosphere, magneto-convection generates small-scale flux concentrations while sunspots and active regions emerge as large-scales concentrations of kG magnetic strength. The dynamics of the tenuous solar corona is dominated by these magnetic fields, and can produce an enormous collection of eruptive and explosive events.

Understanding solar activity requires a systematic study of solar magnetism through different layers of the Sun. Newly launched satellites, such as Hinode and SDO, observe magnetic structures at the photosphere and in the corona with high spatial and temporal resolution. These observations provide us a wealth of information about the formation and destabilization of solar magnetic features. For example, the formation and eruption of AR11158 is well studied with plentiful observations of photospheric

vector magnetic and velocity fields and coronal EUV emission (see Chapter V). Producing an X2.2-class flare, this active region exhibits strong magnetic activity in the presence of a strong persistent shear, in the velocity and magnetic fields along the PIL. During the flare event, the horizontal field intensifies dramatically along the PIL as the coronal loops collapse downward rapidly. All of these observations have advanced our understanding of the physical processes at the photosphere and in the corona. In addition, helioseismology helps us probe the solar interior by analysing oscillations at the photosphere.

Numerical simulations have also greatly advanced our understanding of the solar dynamics. Dynamo models provide key tools to study the amplification of magnetic fields in the interior and the cyclic reversal of the global magnetic field; coronal models with realistic thermodynamic processes allow us to study the coronal magnetism and emission (van der Holst et al., 2010). However, in between the solar interior and corona, the physical properties of the plasma, e.g. density and pressure, demonstrate variations over many orders of magnitude. This imposes a challenge to numerical models. Realistic simulations have been carried out either underneath the surface, or above it to avoid the sharp transition above the photosphere. These simulations illustate a detailed picture of the formation of magnetic structures on the surface. Rempel et al. (2009) and Cheung et al. (2010) simulated the formation of sunspots and active regions by the emergence of magnetic flux from the convection zone. Their work found the important role of the interaction of convective plasma and magnetic fields, which gives rise to the observed features of sunspots and active regions, such as the umbra dots, and coalescence of small-scale fluxes. However, their simulations are restricted to layers at and below the photosphere, and thus unable to capture the coronal response to the flux emergence from the convection zone. Abbett (2007) studied the quiet-Sun magnetoconvection in a extended domain spanning from the convection zone to the corona. Here, we set out to study the emergence of magnetic

fields and formation of ephemeral and active regions in a domain containing the upper convection zone, the photosphere and the outer atmosphere. Our aim is to understand the transfer of the magnetic flux and energy and the interaction of the plasma and magnetic fields through the different layers of the Sun, by numerical simulations and comparison with observations.

6.1 Conclusions

We carry out numerical simulations on the rising of magnetic fields and implement the radiative loss terms, non-ideal equations of state, and empirical corona heating. We summarize our work as follows:

- In Chapter II, we simulate the rise of the magnetic flux from a near-surface granular convection zone into the low corona and illustrate the complex interaction of magnetic fields with the turbulent near-surface plasma and the formation of an ephemeral region. During this process, near-surface convection distorts and deforms the magnetic flux, maintaining intense, disordered magnetic fields in the downdrafts.

- In Chapter III, a magnetic flux rope rises from the upper convection zone (with a depth of 20 Mm) into the corona and interacts with convective cells of varing sizes and forms a solar active region. In the formation of the sunspots, large-scale convective downflows form the bipolar structure of the emerged solar active region, while near-surface convective collapse intensifies the strength of magnetic fields.

- Chapter IV analyses the buildup of coronal free magnetic energy in a flux cancellation event found in the simlation described in Chapter III. At the PIL, shearing flows drive magnetic fields parallel to the PIL and the converging motion around the PIL leads to tether-cutting reconnection, which transfers the

free magnetic energy into the corona.

- Chapter V compares our simulation with observations during a X-class flare. Strong magnetic and velocity shear, intensification of horizontal field strength, and concentration of free magnetic energy in the low corona are found to occur both in the simulation and during the flare event observed by SDO. This consistency suggests the occurrence of tether-cutting reconnection, which can explain the observed features during the flare event, such as the flux cancellation at the photosphere and distribution of coronal free energy.

By studying the flux emergence from the convection zone to the corona and comparing numerical simulations with observations, our work has demonstrated the essential role of the convective motions in the formation of magnetic structures, as shown below:

- **Horizontal motions**, i.e. separation of the bipoles, shearing motion, and rotation, dominates the energy transfer into the corona. Magnetic flux approaches the photosphere as bipoles with emerging flows first, and quickly becomes pulled apart and concentrated in the downflowing region.

- **Rotation of the sunpots** driven by Lorentz force extends from the photosphere to 10 Mm below the convection zone.

- **Coherent shearing flows** driven by Lorentz force occur both at the photosphere and in the corona, with speeds approaching 20 km/s in the corona. Shearing flows along the PIL form strongly **sheared magnetic fields** at the PIL;

- **Tether-cutting reconnection** at the PIL occurs in the highly sheared magnetic fields under shearing and converging flows. The reconnection transfers the magnetic shear into the corona by forming longer, rising loops, while the

shorter, submerging loops from the reconnection causes the flux cancellation at the photosphere as well as the collapse of the coronal loops;

- **Coronal free magnetic energy** increases dramatically in the presence of turbulent surface flows, reaching $7{\times}10^{30}$ ergs, with a growth rate of 3×10^{30} ergs/hr, comparable to that released during CMEs. Moreover, the free magnetic energy is concentrated in the low atmosphere, with 50% stored within 5 Mm above the photosphere. The resulting magnetic structure is composed of highly sheared, compact core overlied by relaxed coronal fields, favorable for eruptive events.

Shearing and converging flows, flux cancellation, magnetic shear and reconnection and rotation of the sunspots have been individually found in earlier work to drive instabilities in the magnetic system and give rise to eruptions. However, the connection between these processes is yet to be determined. Here, in a coupled system of the convection zone, the photosphere and the corona, our simulations perform the first study where multiple processes described above combine to work simultaneously, and transfer the magnetic flux and energy from the solar interior to the outer atmosphere.

6.2 Future Work

Following the study demontrated here, future work can be carried out in three ways:

- Take the input magnetic fields from dynamo models and link the global-scale, deep-convection- zone dynamics to the near-surface and coronal magnetism.

- Expand the size of the simulation domain to that of a solar active region and study the transfer of magnetic and energetic flux in the system.

- Include more realistic physical processes, such as heat conduction, electrical resistivity, and non-gray non-LTE radiative transfer, and simulate the solar magnetism in a more accurate background atmosphere.

- Compare the subsurface structure in the simulations with that from helioseismology, and improve techniques in predicting the flux emergence on the photosphere.

BIBLIOGRAPHY

BIBLIOGRAPHY

Abbett, W. P. 2007, *ApJ*, 665, 1469

Abbett, W. P. & Fisher, G. H. 2003, *ApJ*, 582, 475

—. 2011, ArXiv e-prints

Abbett, W. P., Fisher, G. H., & Fan, Y. 2000, *ApJ*, 540, 548

—. 2001, *ApJ*, 546, 1194

Amari, T., Luciani, J. F., Aly, J. J., Mikic, Z., & Linker, J. 2003, *ApJ*, 585, 1073

Amari, T., Luciani, J. F., Aly, J. J., & Tagger, M. 1996, *ApJ*, 466, L39

Antiochos, S. K., DeVore, C. R., & Klimchuk, J. A. 1999, *ApJ*, 510, 485

Archontis, V., Moreno-Insertis, F., Galsgaard, K., Hood, A., & O'Shea, E. 2004, *A&A*, 426, 1047

Archontis, V. & Török, T. 2008, *A&A*, 492, L35

Athay, R. G., Jones, H. P., & Zirin, H. 1985, *ApJ*, 288, 363

Bahcall, J. N. & Ulrich, R. K. 1988, Reviews of Modern Physics, 60, 297

Bercik, D. J. 2002, PhD thesis, MICHIGAN STATE UNIVERSITY

Bieber, J. W. & Rust, D. M. 1995, *ApJ*, 453, 911

Brown, B. P., Browning, M. K., Brun, A. S., Miesch, M. S., & Toomre, J. 2010, *ApJ*, 711, 424

Brown, D. S., Nightingale, R. W., Alexander, D., Schrijver, C. J., Metcalf, T. R., Shine, R. A., Title, A. M., & Wolfson, C. J. 2003, *Sol. Phys.*, 216, 79

Caligari, P., Moreno-Insertis, F., & Schussler, M. 1995, *ApJ*, 441, 886

Canfield, R. C., Hudson, H. S., & McKenzie, D. E. 1999, *Geophys. Res. Lett.*, 26, 627

Cattaneo, F., Emonet, T., & Weiss, N. 2003, *ApJ*, 588, 1183

Chae, J., Wang, H., Qiu, J., Goode, P. R., & Wilhelm, K. 2000, *ApJ*, 533, 535

Charbonneau, P. 2010, Living Reviews in Solar Physics, 7, 3

Cheung, M. C. M., Rempel, M., Title, A. M., & Schüssler, M. 2010, *ApJ*, 720, 233

Cheung, M. C. M., Schüssler, M., & Moreno-Insertis, F. 2007, *A&A*, 467, 703

Cowling, T. G. 1933, *MNRAS*, 94, 39

—. 1957, Magnetohydrodynamics (Interscience Publishers Inc.)

De Pontieu, B., McIntosh, S. W., Hansteen, V. H., & Schrijver, C. J. 2009, *ApJ*, 701, L1

Deng, N., Xu, Y., Yang, G., Cao, W., Liu, C., Rimmele, T. R., Wang, H., & Denker, C. 2006, *ApJ*, 644, 1278

Dere, K. P., Landi, E., Mason, H. E., Monsignori Fossi, B. C., & Young, P. R. 1997, *A&AS*, 125, 149

Dere, K. P., Landi, E., Young, P. R., Del Zanna, G., Landini, M., & Mason, H. E. 2009, *A&A*, 498, 915

Dorch, S. B. F. & Nordlund, A. 1998, *A&A*, 338, 329

Emonet, T. & Cattaneo, F. 2001, *ApJ*, 560, L197

Emonet, T. & Moreno-Insertis, F. 1998, *ApJ*, 492, 804

Falconer, D. A. 2001, *J. Geophys. Res.*, 106, 25185

Falconer, D. A., Moore, R. L., & Gary, G. A. 2002, *ApJ*, 569, 1016

—. 2006, *ApJ*, 644, 1258

—. 2008, *ApJ*, 689, 1433

Fan, Y. 2001, *ApJ*, 554, L111

—. 2004, Living Reviews in Solar Physics, 1, 1

—. 2005, *ApJ*, 630, 543

—. 2008, *ApJ*, 676, 680

—. 2009a, Living Reviews in Solar Physics, 6, 4

—. 2009b, *ApJ*, 697, 1529

Fan, Y., Fisher, G. H., & Deluca, E. E. 1993, *ApJ*, 405, 390

Fan, Y., Fisher, G. H., & McClymont, A. N. 1994, *ApJ*, 436, 907

Fang, F., Manchester, W., Abbett, W. P., & van der Holst, B. 2010, *ApJ*, 714, 1649

Fang, F., Manchester, IV, W., Abbett, W. P., & van der Holst, B. 2012a, *ApJ*, accepted

—. 2012b, *ApJ*, 745, 37

Fisher, G. H., Fan, Y., Longcope, D. W., Linton, M. G., & Pevtsov, A. A. 2000, *Sol. Phys.*, 192, 119

Forbes, T. G. 2000, *J. Geophys. Res.*, 105, 23153

Forbes, T. G. & Isenberg, P. A. 1991, *ApJ*, 373, 294

Forbes, T. G., Linker, J. A., Chen, J., Cid, C., Kóta, J., Lee, M. A., Mann, G., Mikić, Z., Potgieter, M. S., Schmidt, J. M., Siscoe, G. L., Vainio, R., Antiochos, S. K., & Riley, P. 2006, *Space Sci. Rev.*, 123, 251

Foukal, P. 1971, *Sol. Phys.*, 19, 59

Galsgaard, K., Archontis, V., Moreno-Insertis, F., & Hood, A. W. 2007, *ApJ*, 666, 516

Gary, G. A., West, E. A., Rees, D., McKay, J. A., Zukic, M., & Herman, P. 2007, *A&A*, 461, 707

Ghizaru, M., Charbonneau, P., & Smolarkiewicz, P. K. 2010, *ApJ*, 715, L133

Gombosi, T. I. 1998, Physics of the space environment (Cambridge University Press)

Gopalswamy, N. 2006, *Space Sci. Rev.*, 124, 145

Gosain, S. 2012, *ApJ*, 749, 85

Gosling, J. T., Bame, S. J., McComas, D. J., & Phillips, J. L. 1990, *Geophys. Res. Lett.*, 17, 901

Gough, D. & Toomre, J. 1991, *ARA&A*, 29, 627

Green, L. M., Kliem, B., & Wallace, A. J. 2011, *A&A*, 526, A2+

Gudiksen, B. V., Carlsson, M., Hansteen, V. H., Hayek, W., Leenaarts, J., & Martínez-Sykora, J. 2011, *A&A*, 531, A154+

Gudiksen, B. V. & Nordlund, Å. 2005, *ApJ*, 618, 1020

Guo, W. P. & Wu, S. T. 1998, *ApJ*, 494, 419

Hagenaar, H. J., Schrijver, C. J., & Title, A. M. 2003, *ApJ*, 584, 1107

Hagyard, M. J., Teuber, D., West, E. A., & Smith, J. B. 1984, *Sol. Phys.*, 91, 115

Hale, G. E. 1908, *ApJ*, 28, 315

Hansteen, V. H., De Pontieu, B., Rouppe van der Voort, L., van Noort, M., & Carlsson, M. 2006, *ApJ*, 647, L73

Harvey, K. L., Jones, H. P., Schrijver, C. J., & Penn, M. J. 1999, *Sol. Phys.*, 190, 35

Hathaway, D. H. 2010, Living Reviews in Solar Physics, 7, 1

Hathaway, D. H., Beck, J. G., Bogart, R. S., Bachmann, K. T., Khatri, G., Petitto, J. M., Han, S., & Raymond, J. 2000, *Sol. Phys.*, 193, 299

Hundhausen, A. J. 1993, *J. Geophys. Res.*, 98, 13177

Jouve, L. & Brun, A. S. 2009, *ApJ*, 701, 1300

Kazachenko, M. D., Canfield, R. C., Longcope, D. W., Qiu, J., Des Jardins, A., & Nightingale, R. W. 2009, *ApJ*, 704, 1146

Kitiashvili, I. N., Kosovichev, A. G., Wray, A. A., & Mansour, N. N. 2010, *ApJ*, 719, 307

Klimchuk, J. A. 2006, *Sol. Phys.*, 234, 41

Kosovichev, A. G. 1996, *ApJ*, 461, L55+

Kosovichev, A. G. & Duvall, T. L. 2006, *Space Sci. Rev.*, 124, 1

Kuperus, M., Ionson, J. A., & Spicer, D. S. 1981, *ARA&A*, 19, 7

Leake, J. E., Linton, M. G., & Antiochos, S. K. 2010, *ApJ*, 722, 550

Leka, K. D. & Steiner, O. 2001, *ApJ*, 552, 354

Lemen, J. R., Title, A. M., Akin, D. J., Boerner, P. F., Chou, C., Drake, J. F., Duncan, D. W., Edwards, C. G., Friedlaender, F. M., Heyman, G. F., Hurlburt, N. E., Katz, N. L., Kushner, G. D., Levay, M., Lindgren, R. W., Mathur, D. P., McFeaters, E. L., Mitchell, S., Rehse, R. A., Schrijver, C. J., Springer, L. A., Stern, R. A., Tarbell, T. D., Wuelser, J.-P., Wolfson, C. J., Yanari, C., Bookbinder, J. A., Cheimets, P. N., Caldwell, D., Deluca, E. E., Gates, R., Golub, L., Park, S., Podgorski, W. A., Bush, R. I., Scherrer, P. H., Gummin, M. A., Smith, P., Auker, G., Jerram, P., Pool, P., Soufli, R., Windt, D. L., Beardsley, S., Clapp, M., Lang, J., & Waltham, N. 2012, *Sol. Phys.*, 275, 17

Leroy, J. L. 1989, in Astrophysics and Space Science Library, Vol. 150, Dynamics and Structure of Quiescent Solar Prominences, ed. E. R. Priest, 77–113

Li, Y., Luhmann, J., Fisher, G., & Welsch, B. 2004, Journal of Atmospheric and Solar-Terrestrial Physics, 66, 1271

Linker, J. A., Mikić, Z., Lionello, R., Riley, P., Amari, T., & Odstrcil, D. 2003, Physics of Plasmas, 10, 1971

Lites, B. W. 2005, *ApJ*, 622, 1275

Lites, B. W., Low, B. C., Martinez Pillet, V., Seagraves, P., Skumanich, A., Frank, Z. A., Shine, R. A., & Tsuneta, S. 1995, *ApJ*, 446, 877

Liu, C., Deng, N., Liu, R., Lee, J., Wiegelmann, T., Jing, J., Xu, Y., Wang, S., & Wang, H. 2012, *ApJ*, 745, L4

Liu, C., Deng, N., Liu, Y., Falconer, D., Goode, P. R., Denker, C., & Wang, H. 2005, *ApJ*, 622, 722

Longcope, D. W. & Klapper, I. 1997, *ApJ*, 488, 443

Longcope, D. W. & Welsch, B. T. 2000, *ApJ*, 545, 1089

Low, B. C. 1994, Physics of Plasmas, 1, 1684

—. 2001, *J. Geophys. Res.*, 106, 25141

Lynch, B. J., Antiochos, S. K., DeVore, C. R., Luhmann, J. G., & Zurbuchen, T. H. 2008, *ApJ*, 683, 1192

Lynch, B. J., Antiochos, S. K., MacNeice, P. J., Zurbuchen, T. H., & Fisk, L. A. 2004, *ApJ*, 617, 589

Lynch, B. J., Li, Y., Thernisien, A. F. R., Robbrecht, E., Fisher, G. H., Luhmann, J. G., & Vourlidas, A. 2010, Journal of Geophysical Research (Space Physics), 115, 7106

MacTaggart, D. & Hood, A. W. 2009, *A&A*, 507, 995

Magara, T. & Longcope, D. W. 2003, *ApJ*, 586, 630

Manchester, W. 2003, Journal of Geophysical Research (Space Physics), 108, 1162

Manchester, W. 2008, in Astronomical Society of the Pacific Conference Series, Vol. 383, Subsurface and Atmospheric Influences on Solar Activity, ed. R. Howe, R. W. Komm, K. S. Balasubramaniam, & G. J. D. Petrie , 91–+

Manchester, W. & Low, B. C. 2000, Physics of Plasmas, 7, 1263

Manchester, IV, W. 2001, *ApJ*, 547, 503

—. 2007, *ApJ*, 666, 532

Manchester, IV, W., Gombosi, T., DeZeeuw, D., & Fan, Y. 2004, *ApJ*, 610, 588

Martens, P. C. & Zwaan, C. 2001, *ApJ*, 558, 872

Martin, S. F., Livi, S. H. B., & Wang, J. 1985, Australian Journal of Physics, 38, 929

Martínez-Sykora, J., Hansteen, V., & Carlsson, M. 2008a, *ApJ*, 679, 871

—. 2008b, *ApJ*, 679, 871

Martínez-Sykora, J., Hansteen, V., DePontieu, B., & Carlsson, M. 2009, *ApJ*, 701, 1569

Meunier, N. & Kosovichev, A. 2003, *A&A*, 412, 541

Miesch, M. S. & Toomre, J. 2009, Annual Review of Fluid Mechanics, 41, 317

Mikic, Z., Barnes, D. C., & Schnack, D. D. 1988, *ApJ*, 328, 830

Mikic, Z. & Linker, J. A. 1994, *ApJ*, 430, 898

Min, S. & Chae, J. 2009, *Sol. Phys.*, 258, 203

Mitalas, R. & Sills, K. R. 1992, *ApJ*, 401, 759

Moore, R. L., Falconer, D. A., & Sterling, A. C. 2012, *ApJ* in press

Moore, R. L., Sterling, A. C., Hudson, H. S., & Lemen, J. R. 2001, *ApJ*, 552, 833

Moreno-Insertis, F. & Emonet, T. 1996, *ApJ*, 472, L53

Nagata, S., Tsuneta, S., Suematsu, Y., Ichimoto, K., Katsukawa, Y., Shimizu, T., Yokoyama, T., Tarbell, T. D., Lites, B. W., Shine, R. A., Berger, T. E., Title, A. M., Bellot Rubio, L. R., & Orozco Suárez, D. 2008, *ApJ*, 677, L145

Nordlund, A., Brandenburg, A., Jennings, R. L., Rieutord, M., Ruokolainen, J., Stein, R. F., & Tuominen, I. 1992, *ApJ*, 392, 647

Nordlund, Å., Stein, R. F., & Asplund, M. 2009, Living Reviews in Solar Physics, 6, 2

Parker, E. N. 1978, *ApJ*, 221, 368

—. 1979a, Cosmical magnetic fields: Their origin and their activity (Oxford University Press)

—. 1979b, *ApJ*, 230, 905

Parnell, C. E., DeForest, C. E., Hagenaar, H. J., Johnston, B. A., Lamb, D. A., & Welsch, B. T. 2009, *ApJ*, 698, 75

Pesnell, W. D., Thompson, B. J., & Chamberlin, P. C. 2012, *Sol. Phys.*, 275, 3

Pevtsov, A. A., Fisher, G. H., Acton, L. W., Longcope, D. W., Johns-Krull, C. M., Kankelborg, C. C., & Metcalf, T. R. 2003, *ApJ*, 598, 1387

Powell, K. G., Roe, P. L., Linde, T. J., Gombosi, T. I., & de Zeeuw, D. L. 1999, Journal of Computational Physics, 154, 284

Rachmeler, L. A., DeForest, C. E., & Kankelborg, C. C. 2009, *ApJ*, 693, 1431

Rempel, M. 2011, *ApJ*, 729, 5

Rempel, M. & Schlichenmaier, R. 2011, Living Reviews in Solar Physics, 8, 3

Rempel, M., Schüssler, M., & Knölker, M. 2009, *ApJ*, 691, 640

Rogers, F. J. 2000, Physics of Plasmas, 7, 51

Roussev, I. I., Sokolov, I. V., Forbes, T. G., Gombosi, T. I., Lee, M. A., & Sakai, J. I. 2004, *ApJ*, 605, L73

Scherrer, P. H., Schou, J., Bush, R. I., Kosovichev, A. G., Bogart, R. S., Hoeksema, J. T., Liu, Y., Duvall, T. L., Zhao, J., Title, A. M., Schrijver, C. J., Tarbell, T. D., & Tomczyk, S. 2012, *Sol. Phys.*, 275, 207

Schrijver, C. J. 2007, *ApJ*, 655, L117

—. 2009, Advances in Space Research, 43, 739

—. 2010, *ApJ*, 710, 1480

Schrijver, C. J., Aulanier, G., Title, A. M., Pariat, E., & Delannée, C. 2011, *ApJ*, 738, 167

Schrijver, C. J., De Rosa, M. L., Metcalf, T., Barnes, G., Lites, B., Tarbell, T., McTiernan, J., Valori, G., Wiegelmann, T., Wheatland, M. S., Amari, T., Aulanier, G., Démoulin, P., Fuhrmann, M., Kusano, K., Régnier, S., & Thalmann, J. K. 2008, *ApJ*, 675, 1637

Schrijver, C. J., De Rosa, M. L., Title, A. M., & Metcalf, T. R. 2005, *ApJ*, 628, 501

Schrijver, C. J. & Zwaan, C. 2000, Solar and Stellar Magnetic Activity (Cambridge University Press)

Schwarzschild, M. 1958, Structure and evolution of the stars (Princeton University Press)

Shibata, K., Tajima, T., Steinolfson, R. S., & Matsumoto, R. 1989, *ApJ*, 345, 584

Sokolov, I. V., Powell, K. G., Cohen, O., & Gombosi, T. I. 2008, in Astronomical Society of the Pacific Conference Series, Vol. 385, Numerical Modeling of Space Plasma Flows, ed. N. V. Pogorelov, E. Audit, & G. P. Zank, 291

Spruit, H. C. 1979, *Sol. Phys.*, 61, 363

—. 1981, *A&A*, 98, 155

Spruit, H. C. & van Ballegooijen, A. A. 1982, *A&A*, 106, 58

St. Cyr, O. C., Plunkett, S. P., Michels, D. J., Paswaters, S. E., Koomen, M. J., Simnett, G. M., Thompson, B. J., Gurman, J. B., Schwenn, R., Webb, D. F., Hildner, E., & Lamy, P. L. 2000, *J. Geophys. Res.*, 105, 18169

Stein, R. F., Lagerfjärd, A., Nordlund, Å., & Georgobiani, D. 2011, *Sol. Phys.*, 268, 271

Stein, R. F. & Nordlund, Å. 2000, *Sol. Phys.*, 192, 91

—. 2006, *ApJ*, 642, 1246

Steinolfson, R. S. 1991, *ApJ*, 382, 677

Sturrock, P. A., Weber, M., Wheatland, M. S., & Wolfson, R. 2001, *ApJ*, 548, 492

Su, Y., Golub, L., & Van Ballegooijen, A. A. 2007, *ApJ*, 655, 606

Subramanian, P. & Dere, K. P. 2001, *ApJ*, 561, 372

Sun, X., Hoeksema, J. T., Liu, Y., Wiegelmann, T., Hayashi, K., Chen, Q., & Thalmann, J. 2012, *ApJ*, 748, 77

Titov, V. S. & Démoulin, P. 1999, *A&A*, 351, 707

Tokman, M. & Bellan, P. M. 2002, *ApJ*, 567, 1202

Török, T. & Kliem, B. 2005, *ApJ*, 630, L97

Tortosa-Andreu, A. & Moreno-Insertis, F. 2009a, *A&A*, 507, 949

—. 2009b, *A&A*, 507, 949

Tóth, G., van der Holst, B., Sokolov, I. V., de Zeeuw, D. L., Gombosi, T. I., Fang, F., Manchester, W. B., Meng, X., Najib, D., Powell, K. G., Stout, Q. F., Glocer, A., Ma, Y.-J., & Opher, M. 2012, Journal of Computational Physics, 231, 870

van Ballegooijen, A. A. & Mackay, D. H. 2007, *ApJ*, 659, 1713

van der Holst, B., Jacobs, C., & Poedts, S. 2007, *ApJ*, 671, L77

van der Holst, B., Manchester, IV, W., Sokolov, I. V., Tóth, G., Gombosi, T. I., DeZeeuw, D., & Cohen, O. 2009, *ApJ*, 693, 1178

van der Holst, B., Manchester, IV, W. B., Frazin, R. A., Vásquez, A. M., Tóth, G., & Gombosi, T. I. 2010, *ApJ*, 725, 1373

Vögler, A. & Schüssler, M. 2007, *A&A*, 465, L43

Vögler, A., Shelyag, S., Schüssler, M., Cattaneo, F., Emonet, T., & Linde, T. 2005, *A&A*, 429, 335

Vrabec, D. 1974, in IAU Symposium, Vol. 56, Chromospheric Fine Structure, ed. R. G. Athay, 201–+

Walsh, R. W. & Ireland, J. 2003, *A&A Rev.*, 12, 1

Wang, S., Liu, C., Liu, R., Deng, N., Liu, Y., & Wang, H. 2012, *ApJ*, 745, L17

Wu, S. T. & Guo, W. P. 1997, Advances in Space Research, 20, 2313

Yang, G., Xu, Y., Cao, W., Wang, H., Denker, C., & Rimmele, T. R. 2004, *ApJ*, 617, L151

Yashiro, S., Gopalswamy, N., Akiyama, S., Michalek, G., & Howard, R. A. 2005, Journal of Geophysical Research (Space Physics), 110, 12

Zhang, J., Dere, K. P., Howard, R. A., & Vourlidas, A. 2004, *ApJ*, 604, 420

Zhao, J. & Kosovichev, A. G. 2003, *ApJ*, 591, 446

Zirin, H. & Wang, H. 1993, *Nature*, 363, 426

Zwaan, C. 1985, *Sol. Phys.*, 100, 397

—. 1987, *ARA&A*, 25, 83